# Chiral Fermions in Lattice QCD and Random Matrix Theory

Dissertation

zur Erlangung des
Doktorgrades der Naturwissenschaften
(Dr. rer. nat.)
der Naturwissenschaftlichen Fakultät II – Physik
der Universität Regensburg

vorgelegt von
Wolfgang Söldner
aus
Burgkirchen

Regensburg, Juli 2004

Promotionsgesuch eingereicht am: 7. Juli 2004

Die Arbeit wurde angeleitet von: Prof. Dr. A. Schäfer

Prüfungsausschuß: Prof. Dr. D. Weiss
Prof. Dr. A. Schäfer
Prof. Dr. J. Keller
Prof. Dr. V. Braun

# Contents


**1 Introduction** **5**

**2 Lattice QCD in Short Words** **9**
2.1 How to discretize QCD . . . . . 9
2.1.1 QCD in the Euclidean Path Integral Formulation . . . . . 9
2.1.2 The Fermionic Action . . . . . 11
2.1.3 The Gluonic Action . . . . . 17
2.2 Finite Temperature QCD . . . . . 22
2.3 The Polyakov Loop . . . . . 23
2.4 The Banks-Casher Relation . . . . . 27
2.5 Instantons and Chiral Symmetry Breaking . . . . . 29
2.5.1 Classical Vacua . . . . . 29
2.5.2 Tunneling . . . . . 30
2.5.3 Zero Modes . . . . . 33
2.5.4 Instantons and Chiral Symmetry Breaking . . . . . 34

**3 Chiral Symmetry and Confinement** **37**
3.1 The Connection between Chiral Symmetry and Confinement . . . . . 37
3.2 The Low-Lying Eigenvalues of the Dirac Operator . . . . . 39
3.3 The Distribution of the Spectral Gap . . . . . 42
3.4 The Averaged Spectral Gap I . . . . . 45
3.4.1 Results for the Polyakov Loop . . . . . 46
3.4.2 Results for the Dirac Eigenvalues . . . . . 48
3.5 The Averaged Spectral Gap II . . . . . 49
3.5.1 Results for Staggered Fermions . . . . . 51
3.5.2 Staggered Fermions and Chiral Symmetry . . . . . 53
3.5.3 The Influence of the Quasi-Zero Modes . . . . . 57

**4 Searching Calorons on the Lattice** **63**
4.1 Calorons . . . . . 64
4.2 The Inverse Participation Ratio . . . . . 66
4.3 Calorons on the Lattice: Numerical Results . . . . . 67

**5 Normal Modes in Random Matrix Theory and QCD** **77**
5.1 Normal Modes and the Gaussian Ensembles . . . . . 78
5.2 Normal Modes and the Poisson Ensemble . . . . . 82
5.3 The Chiral Random Matrix Model . . . . . 83
5.4 Normal Modes and the Chiral Random Matrix Model . . . . . 85
5.5 Unfolding . . . . . 88
5.6 Normal Modes: Numerical Results . . . . . 89

**6 Conclusions** **105**

# Chapter 1

# Introduction

Since during the last years computer power has reached a level where lattice simulations in quantum chromodynamics (QCD) are becoming more and more enhanced, lattice QCD has developed into a popular subject in QCD. Before the advent of lattice QCD most predictions were limited to the perturbative regime. Perturbative methods in QCD can be applied only to the high energy regime in QCD, which is probed in modern accelerators like RHIC (relativistic heavy ion collider) at the Brookhaven National Lab in New York or the LHC (large hadron collider) at CERN. The somehow surprising point is that QCD at high energies behaves almost like a free theory. This means that the quarks at high energies interact only weakly through the gluon field. So, the coupling constant in the high energy regime is small which allows a systematic expansion of the theory in terms of the coupling constant and perturbative methods are applicable. The observation that the constituents of hadrons, the quarks, behave like free particles goes under the name of asymptotic freedom and was a major achievement in investigating the strong force.

However, many interesting phenomena in QCD appear at low energies. For example, the temperature of the hadronic matter which we are made of is, fortunately, very low, i.e. the typical energy of the system is low. It turns out that the coupling constant in QCD depends on the energy at which we are looking at our system. As already mentioned above, for high energies the coupling is small. But for low energies the coupling constant increases more and more. So, the coupling constant is not constant at all but it is "running", which is the reason why it is sometimes called "running coupling". The fact that the coupling is large at large distances is supposed to be intimately related to the non-abelian structure of QCD. The consequence of this property is that the colored gluons, which mediate the interactions between the quarks, are self-interacting. Furthermore, one believes that the self-coupling of the gluons is connected to the confining property of QCD. Each quark comes in three colors. Nevertheless, no one has yet observed colored quarks. We only find color neutral objects in nature like mesons or baryons, which consist of two or three confined quarks (or anti–quarks), respectively, or Glueballs, which consist of pure gluons. (Note that those glueballs have not yet been observed.) Since confinement appears at low energies, only a non-perturbative approach, like lattice QCD, can confirm that QCD accounts for confinement.

A second very interesting property of QCD is the spontaneous breaking of chiral symmetry. Quarks can not only be distinguished by their color, but they are also differently "flavored". There are six different quarks which we label by a flavor index. In the limit where the quark masses of the different flavors are zero, the QCD Lagrangian is invariant under a global symmetry, the chiral symmetry. Chiral symmetry is reflected in the mass spectrum and can, in principle, be observed. The lightest two (or three) quarks have relatively small masses compared to the typical energy scale of QCD, which is about 1 GeV. Therefore, the QCD Lagrangian is approximately chirally symmetric for these light quarks which should also show up in the mass spectrum. However, it turns out that chiral symmetry is not manifest in nature, but spontaneously broken. We can detect the (almost) massless Goldstone bosons, the pions, which appear because of the spontaneous breaking of the symmetry. The spontaneous breaking of chiral symmetry is, like confinement, a non-perturbative effect and has to be investigated on the lattice or by other non-perturbative methods. One very successful, analytic, and non-perturbative approach is the concept of instantons. Instantons describe tunneling processes in gauge theory. They are of particular interest in QCD because the mechanism of chiral symmetry breaking can be explained by the presence of instantons. Note that chiral symmetry can be investigated also on the lattice. Of course, it is interesting to compare the results of the two different approaches.

A completely different non-perturbative approach to certain aspects of QCD has been found in the framework of random matrix theory (RMT). In RMT one is not interested in the detailed dynamics of the system, but in universal quantities. Universal quantities are quantities which are not specific to one certain system, but to a whole class of systems which all possess the same symmetry properties. The basic idea of RMT is to replace a quantity by an ensemble average over random Hamiltonian matrices. We will calculate observables by averaging over an ensemble of random matrices which follow a certain probability distribution determined by the symmetries of the Hamiltonian. Because of the great progress which was made in RMT in the last decade we can find analytic expressions for many interesting quantities. However, RMT can be used only in a certain regime of the full theory. For example, RMT does not predict where the energy levels exactly lie, but it describes the fluctuations of the levels.

In this thesis we will touch all these non-perturbative topics, lattice QCD, confinement, chiral symmetry, instantons, and random matrix theory. We will point out the connections of the different issues with each other, investigate related unsolved problems, and hope to fertilize the understanding of them.

In Chapter 2 we begin with an introduction to lattice QCD. In order to calculate the important correlation functions numerically we first develop QCD in the Euclidean path integral formalism, see 2.1.1. In the common Minkowski description we cannot calculate the path integrals on the lattice, because the integrand of the path integral is heavily oscillating. In the Euclidean formalism the oscillations are completely gone. In Sec. 2.1.2 and 2.1.3 we show how to put the fermion and gluon fields on the lattice and we also discuss the problems connected to this procedure. The crucial problem on

the lattice is that the number of fermions doubles for each dimension of space-time. So we end up with 16 (interacting) fermions which does not describe QCD correctly. In order to reduce the number of doublers, chiral symmetry has to be broken explicitly. However, if chiral symmetry is explicitly broken, it is hard to study spontaneous chiral symmetry breaking, which we like to investigate. Anyway, there are possibilities to analyze chiral symmetry breaking on the lattice, see Sec. 2.1.2 and 2.1.3. In the latter part of this thesis we will study the spontaneous breaking of chiral symmetry and the confinement phase transition at finite temperature. Therefore, in Sec. 2.2 we will derive the formalism of QCD at finite temperature on the lattice. Furthermore, we will present order parameters for both the confinement and the chiral phase transition, see Sec. 2.3 and 2.4.

Chapter 3 is devoted to the relation of the chiral and confinement phase transition. From lattice studies we know that both phase transitions approximately appear at the same temperature which suggests that chiral symmetry and confinement should be connected somehow. Although intense work already has been invested in solving this puzzle, the relation of these two properties of QCD remains unknown. We will investigate the critical temperature of the chiral phase transition depending on a certain gluonic sector of the theory. In the literature it was claimed that there is indeed a dependence on that specific sector which should be a hint to the missing link. The discussion of these findings was very controversial. This motivated us to reinvestigate this problem again, but with fermions which have much better chiral properties.

Above we mentioned that the non-perturbative concept of instantons can describe the mechanism of chiral symmetry breaking. In the low temperature phase, where chiral symmetry is broken, the instantons only interact weakly with the anti–instantons, while in the high temperature phase strongly interacting instantons form a kind of "molecules" with the anti–instantons, which leads to the restoration of chiral symmetry. This is the so-called instanton picture of chiral symmetry breaking. In Chapter 4 we will search for instantons on the lattice at finite temperature, the so-called calorons, and we like to prove or disprove the correctness of this instanton picture. We will apply a new approach for which we can circumvent the usual problems which occur when identifying the instantons on the lattice. This approach makes use of the localization properties of a quark in an instanton background field and could provide evidence for calorons on the lattice.

Before we conclude in Chapter 6 we switch to a different, non-perturbative subject in Chapter 5, namely random matrix theory. In the beginning of the section we will apply RMT to QCD and present the chiral random matrix model. This model allows us to make RMT predictions for QCD in the chiral limit. Since there is no analytical proof that QCD is in the universality class of this model one employs lattice QCD to gather evidence for this assumption. In particular, we develop the formalism of the normal modes, see Sec. 5.1, Sec. 5.2, and Sec. 5.4, which allows us to describe the fluctuations of the eigenvalues in an easy way. These normal modes are then calculated also on the lattice and we compare the results of lattice QCD and RMT, see Sec. 5.6. This comparison of our results for the normal modes we will lead to a

new method to determine the Thouless energy, the engery scale below which RMT is applicable.

# Chapter 2

# Lattice QCD in Short Words

In this chapter we will develop the basic formalism which is necessary to perform lattice simulations in QCD [1, 2]. In Sec. 2.1 we first develop the path integral formulation in the Euclidean space. We have to do so because in Minkowski space the path integrals cannot be calculated in practice. In the following we will discretize the fermion and gauge field and also discuss fermion doubling which turns out to be a problem if we like to have chiral symmetry established on the lattice. In Sec. 2.3 and 2.4 we derive order parameters for the confinement and chiral phase transition. We will develop useful tools which allows us to study the chiral and confinement properties of QCD, see Chapters 3 and 4.

## 2.1 How to discretize QCD

A main task of every theory is to calculate the correlation functions of the system. In the path integral formalism of QCD these correlation functions are given by

$$\left\langle \Omega \middle| T\big(\Psi_1(x_1)\cdots\bar{\Psi}_1(x_1)\cdots\big) \middle| \Omega \right\rangle = \frac{\int \mathrm{D}[\bar{\psi}]\,\mathrm{D}[\psi]\ \psi_1(x_1)\cdots\bar{\psi}_1(x_1)\cdots\,\mathrm{e}^{\mathrm{i}S[\bar{\psi},\psi]}}{\int \mathrm{D}[\bar{\psi}]\,\mathrm{D}[\psi]\ \mathrm{e}^{\mathrm{i}S[\bar{\psi},\psi]}}, \tag{2.1}$$

where $T(\Psi_1(x_1)\cdots\bar{\Psi}_1(x_1)\cdots)$ is the time-ordered product of the field operators $\Psi(x)$ and $\bar{\Psi}(x)$ and $\bar{\psi}(x)$, $\psi(x)$ are the corresponding Grassmann-valued fields. $\mathrm{D}[\psi]$ denotes the product $\prod_i \mathrm{d}\psi_i$. In the following we will found out how to calculate the correlation functions in lattice QCD.

### 2.1.1 QCD in the Euclidean Path Integral Formulation

The QCD Dirac operator in Minkowski space is given by

$$\mathrm{i}\not{D} = \mathrm{i}D_\mu\gamma^\mu = \mathrm{i}(\partial_\mu + \mathrm{i}g\frac{\lambda^a}{2}A^a_\mu)\gamma^\mu \tag{2.2}$$

with the coupling constant $g$ and the 8 generators $\lambda^a$ of the su(3) lie algebra. These generators satisfy the commutation relation

$$[\lambda^a, \lambda^b] = 2\mathrm{i} f^{abc} \lambda^c, \tag{2.3}$$

with the structure constants $f^{abc}$. The matrices obey the normalization condition

$$\mathrm{Tr}(\lambda^a \lambda^b) = 2\,\delta^{ab}. \tag{2.4}$$

We abbreviate the gauge fields by

$$A_\mu(x) \equiv \sum_{a=1}^{8} A_\mu^a(x) \frac{\lambda^a}{2}, \tag{2.5}$$

where $A_\mu^a \in \mathbb{R}$. The $\gamma$-matrices obey the common anti–commutation relation $\{\gamma^\mu, \gamma^\nu\} = 2g^{\mu\nu}$. In connection with the $\gamma$-matrices we often use the Feynmann slash notation, e.g. $\not{\partial} = \gamma^\mu \partial_\mu$.

The QCD action with $N_f$ flavors then is given by

$$S_{QCD} = \int \mathrm{d}^4x\, \bar{\psi}(x)(\mathrm{i}\not{D} - M)\psi(x) - \frac{1}{2}\mathrm{Tr} \int \mathrm{d}^4x F_{\mu\nu}(x) F^{\mu\nu}(x). \tag{2.6}$$

$\bar{\psi} = \psi^\dagger \gamma^0$ and $\psi$ are the fermion fields which are vectors in flavor space, $\bar{\psi}, \psi \equiv \bar{\psi}^f, \psi^f$. $M$ is the (diagonal) mass matrix which acts on the flavor index, and

$$F_{\mu\nu} = \partial_\mu A_\nu - \partial_\nu A_\mu + \mathrm{i}g[A_\mu, A_\nu] \equiv \sum_{a=1}^{8} F_{\mu\nu}^a \frac{\lambda^a}{2} \tag{2.7}$$

is the field strength tensor. Now we can write down the QCD partition function for $N_f$ flavors,

$$Z_{QCD} = \int \mathrm{D}[A]\, \mathrm{D}[\bar{\psi}]\, \mathrm{D}[\psi]\, \mathrm{e}^{\mathrm{i}S_{QCD}} = \int \mathrm{D}[A]\, \mathrm{e}^{\mathrm{i}S_g} \prod_{f=1}^{N_f} \det(\mathrm{i}\not{D} - m_f), \tag{2.8}$$

where we have integrated out the fermionic part in the second term. The $m_i$ are the entries of the diagonal mass matrix $M$. Note that the integral over the fields in the partition function in (2.8) is mathematically not well defined. Only in some special theories the partition function is mathematically meaningful and can be calculated at all. On the lattice the situation is different. There the partition function is well defined and can, in principle, be calculated. But due to the imaginary exponent in (2.8) the partition function is heavily oscillating which makes practical calculations impossible. Anyway, we can work around this problem and cure it by introducing the concept of the Euclidean description. We are replacing $x^0$ by $-\mathrm{i}x_4$ introducing imaginary times. We find immediately $x^2 = x^\mu x^\nu g_{\mu\nu} = -((x^1)^2 + (x^2)^2 + (x^3)^2 + (x^4)^2)$ which shows the Euclidean nature. For the differential operator $\partial_\mu$ it follows that we have to make the replacement $\partial_0 \to \mathrm{i}\partial_4$. Further we have to change the $\gamma$-matrices. Because

in Euclidean space the Lorentz group is replaced by the ordinary four-dimensional rotation group we introduce the Euclidean $\gamma$-matrices, $\gamma_4^E = \gamma^0$, $\gamma_i^E = -\mathrm{i}\gamma^i$, which obey the anti–commutation relation

$$\{\gamma_\mu^E, \gamma_\nu^E\} = 2\delta_{\mu\nu}. \tag{2.9}$$

Therefore we have to replace $\not{\partial} \to \mathrm{i}\not{\partial}^E = \mathrm{i}\partial_\mu^E \gamma_\mu^E$ and with the definition above $\gamma^5 = \mathrm{i}\gamma^0\gamma^1\gamma^2\gamma^3$ becomes $\gamma_5^E = \gamma_1\gamma_2\gamma_3\gamma_4$. Finally, we find for the fermionic part of the Euclidean action

$$S_q^E = \int \mathrm{d}^4x\, \bar{\psi}(x)(\not{\partial}^E + M)\psi(x). \tag{2.10}$$

Note that $\bar{\psi}$ in Euclidean space corresponds to $\bar{\psi} = \psi^\dagger$ because the associated bilinear $\bar{\psi}\psi$ is just $\psi^\dagger\psi$. To obtain the gauge part of the Euclidean action we have to look at the transformation property of $A_\mu$. From $D_\mu = \partial_\mu + \mathrm{i}gA_\mu$ we find that $A_\mu$ has to transform like $\partial_\mu$. So we have to make the same replacement as before, $A_0 \to \mathrm{i}A_4$, which means that $F^a_{\mu\nu}F^{\mu\nu a} \to F^a_{\mu\nu}F^a_{\mu\nu}$. Finally, we find for the QCD Euclidean action

$$S_{QCD}^E = \int \mathrm{d}^4x \bar{\psi}(\not{D}^E + M)\psi + \frac{1}{4}\int \mathrm{d}^4x F^a_{\mu\nu}F^a_{\mu\nu}. \tag{2.11}$$

(Since from now on we will work only in Euclidean space we will drop the label "E".) Now the exponent in the QCD partition function is real and the integral is well defined,

$$Z_{QCD} = \int \mathrm{D}[A]\,\mathrm{D}[\bar{\psi}]\,\mathrm{D}[\psi]\,\mathrm{e}^{-S_{QCD}} = \int \mathrm{D}[A]\,\mathrm{e}^{-S_g}\prod_{f=1}^{N_f}\det(\not{D} + m_f). \tag{2.12}$$

This is the starting point for many lattice calculations. By the way, another often used approach for lattice calculations is the Hamiltonian formulation of QCD. The main disadvantage hereby is the explicitly broken Lorentz invariance. Different from the Lagrangian approach, the broken Lorentz invariance is also manifest in the continuum.

### 2.1.2 The Fermionic Action

We are now prepared to derive a lattice formulation of QCD. We begin with the pure fermionic part of the Euclidean action, in (2.11)

$$S_q = \int \mathrm{d}^4x\, \bar{\psi}(x)(\not{\partial} + m)\psi(x). \tag{2.13}$$

In order to discretize $S_q$ in (2.13) we are making the following substitutions

$$\psi(x), \bar{\psi}(x) \to \psi_x, \bar{\psi}_x \tag{2.14}$$

$$\partial_\mu\psi_x \to \frac{1}{2a}\left(\psi_{x+\hat{\mu}} - \psi_{x-\hat{\mu}}\right) \tag{2.15}$$

$$\int \mathrm{d}^4x \to a^4\sum_x \tag{2.16}$$

$$\mathrm{D}[\bar{\psi}]\,\mathrm{D}[\psi] \to \prod_{\alpha,x}\mathrm{d}\bar{\psi}_{\alpha x}\prod_{\beta,y}\mathrm{d}\psi_{\beta y}, \tag{2.17}$$

where $\psi_{\alpha x}$ is the field at lattice site $x = (x_1, x_2, x_3, x_4)$ with $x_\mu = 1, 2, \ldots, L_\mu$. The Dirac index is labeled by $\alpha = 1, 2, 3, 4$. The neighboring site of $x$ in $\mu$-direction is denoted by $x + \hat{\mu}$ with $\mu = 1, 2, 3, 4$. $L_\mu$ is the number of lattice sites in $\mu$-direction and $a$ denotes the lattice spacing. For the fermion action we then obtain

$$S_q = \sum_x a^4 \left( m\bar{\psi}_x\psi_x + \frac{1}{2a}\sum_{\mu=1}^{4} \left(\bar{\psi}_x\gamma_\mu\psi_{x+\hat{\mu}} - \bar{\psi}_{x+\hat{\mu}}\gamma_\mu\psi_x\right)\right) \tag{2.18}$$

$$= \sum_{x,y} a^4 \bar{\psi}_x K_{xy} \psi_y \tag{2.19}$$

with

$$K_{xy} = \sum_{\mu=1}^{4} \frac{1}{2a}\,\gamma_\mu(\delta_{y,x+\hat{\mu}} - \delta_{y,x-\hat{\mu}}) + m\delta_{xy}. \tag{2.20}$$

**Wilson Fermions**

The fermions which correspond to this naive discretization are sometimes called naive fermions. To illustrate the properties of these fermions we will calculate the corresponding propagator

$$\left\langle \psi_x \bar{\psi}_y \right\rangle = \frac{\int \mathrm{D}[\bar{\psi}]\,\mathrm{D}[\psi]\ \psi_x\bar{\psi}_y\,\mathrm{e}^{-S[\bar{\psi},\psi]}}{\int \mathrm{D}[\bar{\psi}]\,\mathrm{D}[\psi]\ \mathrm{e}^{-S[\bar{\psi},\psi]}}. \tag{2.21}$$

Integrating out the Grassmann integrals we obtain

$$\left\langle \psi_x \bar{\psi}_y \right\rangle = K^{-1}_{xy}. \tag{2.22}$$

In order to perform the continuum limit we like to Fourier transform the propagator. Therefore we first Fourier transform $K_{xy}$,

$$K_{xy} = \frac{1}{a}\int_{-\frac{\pi}{a}}^{\frac{\pi}{a}} \frac{a^4\mathrm{d}^4k}{(2\pi)^4} \left(\mathrm{i}\sum_\mu \gamma_\mu\,\sin(ak_\mu) + am\right)\mathrm{e}^{\mathrm{i}ak(x-y)}, \tag{2.23}$$

and afterwards we invert the obtained expression

$$K^{-1}_{xy} = a\int_{-\frac{\pi}{a}}^{\frac{\pi}{a}} \frac{a^4\mathrm{d}^4k}{(2\pi)^4} \frac{-\mathrm{i}\sum_\mu \gamma_\mu\,\sin(ak_\mu) + am}{\sum_\mu \sin^2(ak_\mu) + (am)^2}\,\mathrm{e}^{\mathrm{i}ak(x-y)}. \tag{2.24}$$

The propagator in the continuum limit is then given by

$$\begin{aligned}\left\langle \psi(x)\bar{\psi}(y)\right\rangle &= K^{-1}(x,y) = \lim_{a\to 0} K^{-1}_{xy} \\ &= \lim_{a\to 0}\int_{-\frac{\pi}{a}}^{\frac{\pi}{a}} \frac{a^4\mathrm{d}^4k}{(2\pi)^4} \frac{-\frac{\mathrm{i}}{a}\sum_\mu \gamma_\mu\,\sin(ak_\mu) + m}{\frac{1}{a^2}\sum_\mu \sin^2(ak_\mu) + m^2}\,\mathrm{e}^{\mathrm{i}ak(x-y)}.\end{aligned} \tag{2.25}$$

In order to carry out the continuum limit we expand the sine

$$\frac{1}{a}\sin(ak_\mu) \approx k_\mu + \mathcal{O}(a). \tag{2.26}$$

Inserting this expression into (2.25) and performing the "naive" continuum limit we find for the propagator

$$\left\langle \psi(x)\bar{\psi}(y)\right\rangle = \int_{-\infty}^{\infty} \frac{\mathrm{d}^4k}{(2\pi)^4} \frac{-\mathrm{i}\not{k} + m}{k^2 + m^2}\, \mathrm{e}^{\mathrm{i}k(x-y)} \tag{2.27}$$

which is the correct continuum propagator. However, we did not carry out the continuum limit correctly. The argument of the sine takes values from $-\pi$ to $\pi$. The sine in that interval has two zeros at $-\pi$ and $\pi$ which means that the propagator in the continuum limit has two poles in each direction of $k_\mu$. For all four directions of $k_\mu$ we end up with 16 poles sitting at the edges of the Brillouin zone. We see that the number of fermions has doubled for every space-time dimension. This problem is known as the fermion doubling problem and it becomes crucial if we consider interacting theories (which we usually do). Then, the doublers also interact with the other fermions. But we can circumvent this problem. As we know, on the lattice there are infinitely many versions of the action. So, we can modify the discretized action such that we are adding terms which vanish as $a \to 0$. One easy way to remove the doublers is to introduce a mass which depends on $k_\mu$ and diverges at the edges of the Brillouin zone. This mass, of course, has to coincide with the original mass in the continuum limit. This type of fermions are called Wilson fermions. See Refs. [1, 2] for details.

The main disadvantage of the Wilson fermions is that they explicitly break chiral symmetry. If all the masses in the QCD Lagrangian are equal, QCD is invariant under the global flavor transformations

$$\begin{aligned} \psi &\to \mathrm{e}^{\mathrm{i}\phi^a \frac{\lambda^a}{2}}\psi, \\ \bar{\psi} &\to \bar{\psi}\, \mathrm{e}^{-\mathrm{i}\phi^a \frac{\lambda^a}{2}}, \end{aligned} \tag{2.28}$$

where the $\lambda^a$'s are the generators of the flavor group $\mathrm{SU}(N_f)$ and $\psi$ is a short term for $\psi \equiv \psi^a$ with $a = 1, 2, \ldots, N_f$. In the massless case there is a further symmetry

$$\begin{aligned} \psi &\to \mathrm{e}^{\mathrm{i}\varphi^a\gamma_5 \frac{\lambda^a}{2}}\psi, \\ \bar{\psi} &\to \bar{\psi}\, \mathrm{e}^{-\mathrm{i}\varphi^a\gamma_5 \frac{\lambda^a}{2}}. \end{aligned} \tag{2.29}$$

So in the massless we have a $\mathrm{SU}(N_f) \times \mathrm{SU}(N_f)$ symmetry which is called chiral symmetry. We can decompose the quark fields into left-handed and right-handed components

$$\psi_L(x) = \frac{1-\gamma_5}{2}\psi(x), \tag{2.30}$$

$$\psi_R(x) = \frac{1+\gamma_5}{2}\psi(x), \tag{2.31}$$

$$\psi(x) = \psi_L(x) + \psi_R(x) \tag{2.32}$$

and chiral transformations leaves left- and right-handed fields invariant separately. The important feature of chiral symmetry is that it is spontaneously broken which also shows up in the particle spectrum. We will come back to this topic in Sec. 2.4.

However, Wilson fermions are not suitable to study chiral symmetry on the lattice because they have an explicit mass term in their action and, therefore, violate chiral symmetry explicitly [3]. It turns out that chiral symmetry is a deep problem on the lattice and it is hard work to circumvent this problem. We refer the interested reader to Ref. [4]. In the following we will presented another approach to avoid fermion doubling, but in this case it turns out that we have improved chiral properties.

**Staggered Fermions**

Another possibility to remove the doublers is to double the effective lattice extent. Then, we do not have zeros in the sine of the propagator at the edges of the Brillouin zone. We can achieve this by placing the 4 spinor components of 4 different fermions at the 16 edges of the four-dimensional hypercube. The different fermions may be distinguished by flavor. At every lattice site we now have a one-component field instead of a four-component field. In the continuum limit we then obtain a theory with 4 quark flavor.

Let us derive the action for staggered fermions. We start with the lattice action in (2.18). In order to obtain a one-component quark field we perform a "spin-diagonalization" which can be achieved by a local transformation of the fields

$$\begin{aligned} \psi_x &= A_x \chi_x, \\ \bar{\psi}_x &= \bar{\chi}_x A_x^\dagger, \end{aligned} \tag{2.33}$$

where $A_x$ is a unitary $4 \times 4$-matrix which diagonalizes the $\gamma$-matrices. The matrix $A_x$, thereby, fulfills the relation

$$A_x^\dagger \gamma_\mu A_{x+\hat{\mu}} \equiv \Delta_\mu(x) \in \mathrm{U}(1)^{\times 4}, \tag{2.34}$$

where $\Delta_\mu(x)$ is a diagonal $4 \times 4$ matrix belonging to a representation of the group $\mathrm{U}(1)^{\times 4}$. Each diagonal entity of the matrix belongs to one U(1) group. One possible representation of $A_x$ fulfilling the relation from above is given by

$$A_x = A_x^0 \equiv (\gamma_1)^{x_1} (\gamma_2)^{x_2} (\gamma_3)^{x_3} (\gamma_4)^{x_4}, \tag{2.35}$$

where the $(x_1, x_2, x_3, x_4)$ are the components of the vector $x$. We obtain for $\Delta_\mu(x)$,

$$\begin{aligned} &\Delta_\mu(x) = \Delta_\mu^0(x) \equiv \alpha_{x\mu} \mathbb{1}, \\ &\text{with } \alpha_{x\mu} = (-1)^{x_1 + \cdots + x_{\mu-1}} \quad (\mu = 1, 2, 3, 4). \end{aligned} \tag{2.36}$$

Now we can easily express the lattice action in terms of the new fields $\chi_x$ and $\bar{\chi}_x$

$$S_q = \sum_x a^4 \left\{ m(\bar{\chi}_x \chi_x) + \frac{1}{2a} \sum_{\mu=1}^{4} \left[ (\bar{\chi}_x \Delta_\mu(x) \chi_{x+\hat{\mu}}) - (\bar{\chi}_{x+\hat{\mu}} \Delta_\mu^\dagger(x) \chi_x) \right] \right\}. \tag{2.37}$$

Note that $\chi_x \equiv \chi_x^\alpha$ and $\bar{\chi}_x \equiv \bar{\chi}_x^\alpha$ still have 4 components in Dirac space denoted by $\alpha$. But because we got rid of the Dirac matrix $\gamma_\mu$ and the phase $\alpha_{x\mu}$ is also diagonal in Dirac space we have 4 identical fermions on the lattice. We now can in principle sum over any arbitrary integer $k$, where $\alpha = 1, 2, \ldots, k$. We will choose $k = 1$ and suppress the label $\alpha$. We will see, that in the continuum limit we will obtain a quark field with 4 flavors. For $k = N_k$ we would obtain $4N_k$ flavors. Note that we have reduced the components for the Dirac space but we still have three components in color space. So, if we speak of the one-component $\chi$ fields we refer to the component in Dirac space.

Let us now investigate the lattice action we just obtained in the continuum limit. First, we split our lattice into $2^4$ hypercubes which we label by $y_\mu$ with $0 \leq y_\mu \leq L'_\mu - 1$. The number of lattice sites in $\mu$-direction is denoted by $L_\mu$. So we have $L'_\mu = \frac{1}{2} L_\mu$ hypercubes in $\mu$-direction. Note that we have to use lattices with an even number of sites. The lattice coordinate $x_\mu$ (with $0 \leq x_\mu \leq L_\mu - 1$) can now be written in terms of $y_\mu$,

$$x_\mu = 2y_\mu + \eta_\mu, \quad \eta_\mu = 0, 1. \tag{2.38}$$

So, the sum in the lattice action over all lattice sites can be expressed as a sum over all hypercubes and a sum over all sites in the hypercubes

$$\sum_x = \sum_y{}' \sum_\eta . \tag{2.39}$$

Note that the "staggered phase" $\alpha_{x\mu}$ in (2.36) does not depend on $y$ but only on $\eta$, so $\alpha_{\eta\mu} \equiv \alpha_{x\mu}$. From the 16 components of the one-component $\chi$ field sitting on the edges of a hypercube we can obtain a 4 flavored quark field with 4 Dirac components by taking appropriate linear combinations,

$$q_y^{\alpha a} \equiv \frac{1}{8} \sum_\eta \Gamma_\eta^{\alpha a} \, \chi_{2y+\eta}, \quad \bar{q}_y^{a\alpha} \equiv \frac{1}{8} \sum_\eta \bar{\chi}_{2y+\eta} \, \Gamma_\eta^{\dagger\, a\alpha}, \tag{2.40}$$

where $\alpha$ denotes the Dirac index and $a$ the flavor index, $\alpha, a = 1, \ldots, 4$. The matrices $\Gamma_\eta$ are defined by

$$\Gamma_\eta \equiv (\gamma_1)^{\eta_1} (\gamma_2)^{\eta_2} (\gamma_3)^{\eta_3} (\gamma_4)^{\eta_4} \tag{2.41}$$

and fulfill the relations

$$\frac{1}{4} \mathrm{Tr} \left( \Gamma_\eta^\dagger \Gamma_{\eta'} \right) = \delta_{\eta\eta'}, \quad \frac{1}{4} \sum_\eta \Gamma_\eta^{\dagger\, b\beta} \, \Gamma_\eta^{\alpha a} = \delta^{ba} \delta^{\beta\alpha}. \tag{2.42}$$

From this relations we easily can show

$$\chi_{2y+\eta} = 2 \, \mathrm{Tr} \left( \Gamma_\eta^\dagger q_y \right), \quad \bar{\chi}_{2y+\eta} = 2 \, \mathrm{Tr} \left( \bar{q}_y \Gamma_\eta \right). \tag{2.43}$$

We see that the new quark fields $q$ and $\bar{q}$ now have the space-time index $y$ which is twice as large a $x$. So the propagator is not zero at the edges of the Brillouin zone

anymore because we effectively have doubled the lattice extent. This means that there are no doublers in this description.

Now, we can write the staggered action in (2.37) in terms of the new quark fields. For the mass term we easily obtain

$$\sum_x (\bar{\chi}_x \chi_x) = 16 \sum_y{}' (\bar{q}_y \mathbb{1} \times \mathbb{1} q_y). \tag{2.44}$$

The notation $\gamma \times t$ denotes the direct product of the Dirac matrix $\gamma$ with the flavor matrix $t$. For the kinetic term in the action we need the following relations

$$\begin{aligned} \gamma_\mu \Gamma_\mu &= \delta_{0\eta_\mu} \alpha_{\eta\mu} \Gamma_{\eta+\hat{\mu}} + \delta_{1\eta_\mu} \alpha_{\eta\mu} \Gamma_{\eta-\hat{\mu}}, \\ \gamma_5 \Gamma_\mu \gamma_5 &= (-1)^{\eta_1+\eta_2+\eta_3+\eta_4} \Gamma_\mu. \end{aligned} \tag{2.45}$$

Further we define the lattice derivatives

$$\begin{aligned} \Delta_\mu f_y &\equiv \frac{1}{4}(f_{y+\hat{\mu}} - f_{y-\hat{\mu}}) \to a \partial_\mu f_y, \\ \delta_\mu f_y &\equiv \frac{1}{4}(f_{y+\hat{\mu}} + f_{y-\hat{\mu}} - 2 f_y) \to a^2 \partial_\mu^2 f_y. \end{aligned} \tag{2.46}$$

Finally, we obtain for the staggered action in terms of the new fields

$$S_q = 16 a^4 \sum_y{}' \left\{ m \left(\bar{q}_y \mathbb{1} \times \mathbb{1} q_y\right) + \frac{1}{a} \sum_{\mu=1}^{4} \left(\bar{q}_y \left[\gamma_\mu \times \mathbb{1} \Delta_\mu - \gamma_5 \times t_5 t_\mu \delta_\mu\right] q_y\right) \right\}. \tag{2.47}$$

The flavor matrices $t_\mu$ are defined by

$$t_\mu \equiv \gamma_\mu^T = t_\mu^+ \quad (\mu = 1, 2, \ldots, 5). \tag{2.48}$$

We find that the mass term and the first kinetic term are diagonal in flavor space. The second kinetic term is of order $\mathcal{O}(a)$ and vanishes in the continuum limit. Therefore, in the continuum limit we obtain the correct fermion action with 4 flavors.

As we mentioned above, the one-component fields $\bar{\chi}$ and $\chi$ have improved chiral properties. So, in the massless case staggered fermions are symmetric under the global transformations

$$\left.\begin{aligned} \chi_x &\to U_{o(e)} \chi_x \\ \bar{\chi}_x &\to \bar{\chi}_x U_{e(o)}^+ \end{aligned}\right\} \quad \text{with even (odd) lattice site } x, \tag{2.49}$$

and $U_{o(e)} \in \mathrm{U}(1)$. We see, that the staggered fields transform independently on even and odd lattice sites. In the continuum limit this $\mathrm{U}_o(1) \times \mathrm{U}_e(1)$ symmetry becomes $\mathrm{SU}(4) \times \mathrm{SU}(4) \times \mathrm{U}(1)_A \times \mathrm{U}(1)_V$ with 4 flavors. But for finite $a$ it is explicitly broken by the second kinetic term in the staggered action in (2.47). We see, that the chiral properties for staggered fermions are indeed improved. Therefore, they are more suitable investigating the chiral phase transition.

### 2.1.3 The Gluonic Action

We will now construct the gauge theory on the lattice. We know how to do that in the continuum. We start with the pure fermionic action in (2.13) and require that the action should be invariant under local gauge transformations,

$$\begin{aligned} &\psi(x) \to G(x)\psi, \\ &\bar{\psi}(x) \to \bar{\psi}(x)G^{-1}(x), \end{aligned} \tag{2.50}$$

where $G(x) = \mathrm{e}^{\mathrm{i}\theta(x)^a \frac{\lambda^a}{2}}$ is a SU(3) matrix. This leads us to the covariant derivative $D_\mu = \partial_\mu + \mathrm{i}gA_\mu$ (in Euclidean space). Let us apply this procedure to the lattice.

#### The Wilson Action

By looking at (2.37) we find that the staggered fermion action is not invariant under local gauge transformations of (2.50). This is because of the nonlocal terms $\bar{\chi}_x\chi_{x+\hat{\mu}}$ and $\bar{\chi}_{x+\hat{\mu}}\chi_x$. In order to make these terms gauge-invariant we introduce the path integral

$$U(x,y) = P\mathrm{e}^{\mathrm{i}g\int_x^y \mathrm{d}z_\mu A_\mu(z)} \in \mathrm{SU}(3), \tag{2.51}$$

where $P$ denotes path ordering. From the gauge transformation law of the gauge field $A_\mu$ it follows that the transformation law of this object is given by

$$U(x,y) \to G(x)U(x,y)G^{-1}(y) \tag{2.52}$$

which (in the continuum) makes the nonlocal expression $\bar{\chi}(x)U(x,y)\chi(y)$ gauge-invariant. Consider now the lattice version of $U(x,y)$,

$$U_{x\mu} \equiv U_{(x+\hat{\mu}),x} = \mathrm{e}^{\mathrm{i}gaA_{x\mu}}, \tag{2.53}$$

where we assumed that $y$ is next to $x$. With the help of this expression we can write the staggered action in a gauge-invariant way

$$\begin{aligned} S_q[U,\chi,\bar{\chi}] = \sum_x \Bigg\{ & am(\bar{\chi}_x\chi_x) + \\ & \frac{1}{2}\sum_{\mu=1}^{4} \alpha_{x\mu}\left[(\bar{\chi}_x U^\dagger_{x\mu}\chi_{x+\hat{\mu}}) - (\bar{\chi}_{x+\hat{\mu}}U_{x\mu}\chi_x)\right] \Bigg\}. \end{aligned} \tag{2.54}$$

By expanding $U_{x\mu}$ in terms of the gauge field $A_{x\mu}$,

$$U_{x\mu} = \mathrm{e}^{-\mathrm{i}gaA_{x\mu}} = 1 - \mathrm{i}gaA_{x\mu} - \frac{g^2a^2}{2}A^2_{x\mu} + \ldots, \tag{2.55}$$

we can see by looking at the first two terms how the covariant derivative $D_\mu$ enters the game in the continuum limit. Note that the $U_{x\mu}$'s do not live on the lattice sites but

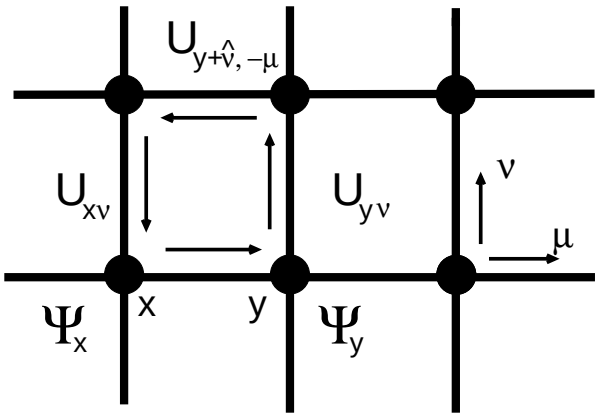


**Figure 2.1:** The link variables $U$ live on the links, the fermion fields $\Psi$ on the lattice sites. We plotted an elementary plaquette.

on the links between two sites. Therefore, we denote the $U_{x\mu}$'s also as link variables. The negative link variables are defined by

$$U_{x(-\mu)} \equiv U^{\dagger}_{(x-\hat{\mu})\mu}, \tag{2.56}$$

where $x - \hat{\mu}$ denotes the neighboring site of $x$ in (negative) $-\mu$-direction. The index $\mu$ can take the values $\mu = \pm 1, \pm 2, \pm 3, \pm 4$.

Let us now come to the kinetic term of the gauge field. We consider the gauge-invariant expression

$$\begin{aligned} U_p \equiv U_{x;\mu\nu} &\equiv U_{(x+\hat{\nu})(-\nu)} U_{(x+\hat{\mu}+\hat{\nu})(-\mu)} U_{(x+\hat{\mu})\nu} U_{x\mu} \\ &= U^{\dagger}_{x\nu} U^{\dagger}_{(x+\hat{\nu})\mu} U_{(x+\hat{\mu})\nu} U_{x\mu}. \end{aligned} \tag{2.57}$$

This expression is a product of the link variables along the elementary lattice cell in the $\mu$-$\nu$-plane, which we is called plaquette, see Fig. 2.1. One possible (Euclidean) gauge action on the lattice can be defined entirely in terms of such plaquette terms

$$\begin{aligned} S_g[U] &= \beta \sum_p \left\{ 1 - \frac{1}{6} \left( \text{Tr } U_p + \text{Tr } U_p^{-1} \right) \right\} \\ &= \beta \sum_p \left( 1 - \frac{1}{3} \text{Re Tr } U_p \right), \end{aligned} \tag{2.58}$$

where

$$\beta = \frac{6}{g^2}. \tag{2.59}$$

The summation over $p$ denotes the sum over all possible plaquettes in (say) counter-clockwise direction

$$\sum_p \equiv \sum_x \sum_{1 \le \mu < \nu \le 4} . \tag{2.60}$$

This lattice action is called Wilson gauge action. We still have to show that in the continuum limit we will obtain the correct action. With the expansion in (2.55), the help of

$$A_{(x+\hat{\mu})\nu} = A_{x\nu} + a\Delta^f_\mu A_{x\nu}, \tag{2.61}$$

where $\Delta^f_\mu$ denotes the lattice derivative in forward direction, and the Campbell-Baker-Hausdorff formula

$$\mathrm{e}^x \mathrm{e}^y = \mathrm{e}^{x+y+\frac{1}{2}[x,y]+\cdots}, \tag{2.62}$$

we find

$$U_{x;\mu\nu} = \mathrm{e}^{-\mathrm{i}ga^2 G_{x;\mu\nu}}, \tag{2.63}$$

where

$$\begin{aligned} G_{x;\mu\nu} &= F_{x;\mu\nu} + \mathcal{O}(a) \\ F_{x;\mu\nu} &= \Delta^f_\mu A_{x\nu} - \Delta^f_\nu A_{x\mu} + [A_{x\mu}, A_{x\nu}]. \end{aligned} \tag{2.64}$$

Because Tr $G_{x\mu\nu} = 0$ we find

$$\text{Tr } (U_p + U_p^{-1}) = 6 + g^2 a^4 \text{ Tr } (F_{x;\mu\nu})^2 + \mathcal{O}(a^5), \tag{2.65}$$

Using the relation

$$\sum_p \text{Tr } (F_{x;\mu\nu})^2 = \frac{1}{2} \sum_{x;\mu,\nu} \text{Tr } (F_{x;\mu\nu})^2 \tag{2.66}$$

we finally obtain for the Wilson action

$$S = -\frac{1}{2} \sum_x a^4 \text{ Tr } F_{x;\mu\nu} F_{x;\mu\nu} + \mathcal{O}(a^5) \tag{2.67}$$

which gives the correct action in the continuum limit. So, the full QCD action on the lattice with staggered fermions and Wilson gauge action is given by

$$S[U, \chi, \bar{\chi}] = S_g[U] + S_q[U, \chi, \bar{\chi}]. \tag{2.68}$$

Let us come back to the starting point of this section, the calculation of the correlation functions. Consider the expectation value of the correlation function $F$

$$\langle F \rangle = \frac{\int \mathrm{D}[U]\, \mathrm{D}[\bar{\chi}]\, \mathrm{D}[\chi]\ \mathrm{e}^{-S_g - S_q}\ F[\chi, \bar{\chi}]}{\int \mathrm{D}[U]\, \mathrm{D}[\bar{\chi}]\, \mathrm{D}[\chi]\ e^{-S_g - S_q}}, \tag{2.69}$$

where $F$ has the bilinear form

$$F[\chi, \bar{\chi}] = \chi_{y_1} \bar{\chi}_{x_1} \chi_{y_2} \bar{\chi}_{x_2} \cdots \chi_{y_n} \bar{\chi}_{x_n}. \tag{2.70}$$

We have to get rid of the (Grassmann-valued) fermionic variables in order to perform lattice calculations. It can be shown that for observables which are only bilinear in the fermion fields we can integrate out the fermionic fields. For example, for the fermionic part in the denominator we obtain

$$\int \mathrm{D}[\bar{\chi}]\,\mathrm{D}[\chi]\ \mathrm{e}^{-S_q} = \det\,[\not{D} + m], \tag{2.71}$$

where for the staggered action $\not{D} + m$ is given by

$$S_q[U, \chi, \bar{\chi}] \equiv \sum_{xy} \bar{\chi}_y (\not{D} + m)_{yx} \chi_x \tag{2.72}$$

with

$$(\not{D} + m)_{xy} = \frac{1}{2} \sum_{\mu=1}^{4} \left[ \alpha_{x\mu} U^{\dagger}_{x\mu} \cdot \delta_{(x+\hat{\mu}),y} - \alpha_{(x-\hat{\mu})\mu} U_{(x-\hat{\mu})\mu} \cdot \delta_{(x-\hat{\mu}),y} \right] + am\, \delta_{xy}. \tag{2.73}$$

If we also integrate out the fermion fields in the numerator we obtain for the correlation function

$$\langle F \rangle = \langle \chi_{y_1} \bar{\chi}_{x_1} \chi_{y_2} \bar{\chi}_{x_2} \cdots \chi_{y_n} \bar{\chi}_{x_n} \rangle = \frac{\int \mathrm{D}[U]\ \mathrm{e}^{-S_g[U] + \log\det\,[\not{D}+m]}\ F[U]}{\int \mathrm{D}[U] \mathrm{e}^{-S_g[U] + \log\det\,[\not{D}+m]}}, \tag{2.74}$$

where $F[U]$ has some complicated dependencies on the gauge field $U$, see [2]. We have written the correlation function entirely in terms of bosonic variables which allows us to calculate it on the lattice.

In order to reduce computation time in our lattice simulations to reasonable times we made use of the so-called "quenched approximation" in all our calculations,

$$\det\,[\not{D} + m] = \text{const.} \tag{2.75}$$

This is a common simplification which is often used in QCD lattice simulations because the calculation of the determinant is extremely expensive. With this simplification Eq. (2.74) becomes

$$\langle F \rangle = \frac{\int \mathrm{D}[U]\ \mathrm{e}^{-S_g[U]}\ F[U]}{\int \mathrm{D}[U] \mathrm{e}^{-S_g[U]}}. \tag{2.76}$$

It turns out that in this approximation we neglect closed quark loops, see Ref. [2]. However, the notation "approximation" is not really justified because this is not an approximation in the sense of an expansion in a small parameter. This means we cannot approximate how large the error is we make. Anyway, lattice calculations have shown that the quenched approximation yields good results which is the other reason why it is widely used.

Now we can start to generate gauge field configurations using the usual quantum Monte Carlo algorithm with importance sampling. Setting $a = 1$ we generate gauge configurations according to the probability given by the gauge action with a fixed value of $\beta$. For each configuration we can calculate different observables and finally compute the expectation value of the observables by simply taking the average over the ensemble. In the same way we obtain ensembles for different values of $\beta$.

Of particular interest are the eigenvalues of the Dirac operator. For each gauge configuration we can calculate the eigenvalues and eigenvectors from which we can calculate fermionic observables by averaging over the ensemble. In our studies we employed the implicit restarted Arnoldi method [5] using the ARPACK library [6, 7].

**Chiral Improvements**

In order to study chiral properties on the lattice we naturally want to have fermions with best chiral properties. As we have seen above, if we remove the fermion doublers we cannot implement chiral symmetry exactly on the lattice. It turns out, that the best we can achieve are fermions which fulfill the Ginsparg-Wilson relation [8]

$$\gamma_5 D + D\gamma_5 = a\, D\gamma_5 D, \tag{2.77}$$

where $D$ denotes the Dirac operator. In the continuum limit $D$ anti–commutes with $\gamma_5$ indicating that chiral symmetry is respected. Currently, there is only one kind of lattice fermions which obey this relation exactly, namely the overlap operator [9], and a few operators which fulfill the relation approximately like domain wall fermions or chirally improved fermions. The lattice simulations for exact Ginsparg-Wilson fermions are very expensive in computer time. Therefore, it is reasonable to look at approximate solutions of the Ginsparg-Wilson relation.

Chirally improved fermions are based on a systematic expansion of the most general Dirac operator [10, 11, 12]. This expansion is plugged into the Ginsparg-Wilson equation from which we obtain a set coupled equations. The expansion of $D$ can be truncated at some level. Solving the corresponding set of equations leads to a Dirac operator which approximately fulfills the Ginsparg-Wilson relations. In practice the expansion is truncated at a level which leads to paths of the Dirac operator which are not longer than 4 links. Note that the longest path for Wilson fermions is one link. The chirally improved fermions have much better chiral properties, e.g. they have numerically exact zero modes.

Because the path length of the Dirac operator is now larger we should also use an improved gauge action with larger path length. In numerical studies the Lüscher-

Weisz gauge action [13, 14] is used

$$\begin{aligned} S_g[U] =& \beta_1 \sum_{pl} \frac{1}{3}\text{Re Tr}\,[1 - U_{pl}] + \\ &+\beta_2 \sum_{rt} \frac{1}{3}\text{Re Tr}\,[1 - U_{rt}] + \\ &+\beta_3 \sum_{pg} \frac{1}{3}\text{Re Tr}\,[1 - U_{pg}]. \end{aligned} \tag{2.78}$$

The first term corresponds to the ordinary sum over the plaquettes. The sum in the second and third term is over all $2 \times 1$ rectangles and all parallelograms, respectively. Note that $\beta_2$ and $\beta_3$ can be computed from $\beta_1$ [15, 16, 17, 18]. We will present numerical results with chirally improved fermions in Chapter 3.

## 2.2 Finite Temperature QCD

In order to study phenomena like the chiral and the confinement phase transition in the vicinity of the critical temperature we have to find out how to incorporate finite temperature in our lattice description. We start with quantum mechanics in the path integral formalism with imaginary time. We can immediately write down the corresponding thermodynamical partition function,

$$Z = \text{Tr}\, \mathrm{e}^{-\beta H}, \tag{2.79}$$

where $H$ is the Hamiltonian and $\beta = 1/T$, with $T$ the temperature. (We set $k_B = 1$.) Consider a system with $n$ degrees of freedom. We denote the coordinate operator by $Q_i$ which has eigenvalues $q_i$. Then Eq. (2.79) can be written as

$$Z = \int \prod_{\alpha=1}^{n} \mathrm{d}q_\alpha \big\langle q \big| \mathrm{e}^{-\beta H} \big| q \big\rangle \tag{2.80}$$

with $\big|q\big\rangle = \big|q_1, q_2, \ldots, q_n\big\rangle$. Note that the coordinates at "times" $\tau = 0$ and $\tau = \beta$ are identified. For Hamiltonians of the form

$$H = \frac{1}{2} \sum_{\alpha=1}^{n} P_\alpha^2 + V(Q) \tag{2.81}$$

we can write for Eq. (2.80)

$$Z = \int_{periodic} [\mathrm{d}q]\, \mathrm{e}^{-\int_0^\beta \mathrm{d}\tau L(q,\dot{q})}, \tag{2.82}$$

where $L_E$ is the (Euclidean) Lagrangian and the label "periodic" refers to the periodic boundary conditions in time direction. We see that by restricting Euclidean time to the interval $[0, \beta]$ and imposing periodic boundary conditions in coordinate space

we obtain the thermodynamical partition function from the path integral formalism, which appears to be somehow miraculous.

We can apply this procedure immediately to quantum field theory. The thermodynamic partition function then is given by

$$Z = \int_{periodic} \mathrm{D}[\phi]\, \mathrm{e}^{-\int_0^\beta \mathrm{d}\tau \int \mathrm{d}x \mathcal{L}(\phi,\dot{\phi})} \tag{2.83}$$

with the (Euclidean) Lagrangian density $\mathcal{L}(\phi, \dot{\phi})$ and periodic boundary conditions on the fields. For our QCD lattice calculations, this means that we have to impose periodic boundary conditions and we have to remember that the temperature is given by the inverse of the lattice extent. In practice we mimic large temperatures by using lattices where the temporal extent of the lattice is much smaller than the spatial extent, and low temperatures by using lattices where the temporal extent of the lattice is equal to the spatial extent. Note that it turns out that for fermion fields, which have Grassmann-valued fields in the path integral, we have to impose anti-periodic boundary conditions, see [2]. So, the QCD thermodynamic partition function can be written as

$$Z = \int_{periodic} \mathrm{D}[A_\mu] \int_{anti-periodic} \mathrm{D}[\bar{\psi}]\, \mathrm{D}[\psi]\, \mathrm{e}^{-\int_0^\beta \mathrm{d}\tau \int \mathrm{d}x\, \mathcal{L}_{QCD}}. \tag{2.84}$$

Now we are prepared for numerical studies. In our numerical calculations we used lattices with $L_s > L_t$. We fix $L_t$ and change the temperature $T = 1/(aL_t)$ by changing $\beta = 6/g$ and hence $a$. Finally, we also have a finite extent of the lattice in the spatial directions. Therefore, we also have to impose spatial boundary conditions. A convenient choice are periodic boundary conditions, but we are free to choose other boundary conditions in this case. We have to consider the limit $V_s \to \infty$ anyway (where $V_s$ is the spatial volume), and in this limit the spatial boundary conditions play no role.

## 2.3 The Polyakov Loop

In this section we derive an order parameter for the confinement phase transition. Unfortunately, it is not easy to define such an order parameter in (full) QCD, which is related to the presence of dynamical fermions. But we will come back to this later. Confinement means that all physical states are color singlets. Consider the easiest case of an quark and an anti–quark. Let the quark have a certain color and the anti–quark the corresponding anti–color, then we can construct a color singlet quark state. Those color singlet quark states are the only quark states which can be observed in nature. There are no colored quark states being observed so far. So, we expect every theory describing the strong force to exhibit confinement.

Let us give a qualitative picture how confinement should work. If we try to separate a color singlet quark–anti-quark pair the potential of the two quarks begins to increase. Illustratively, we think of a tube of flux lines connecting both fermions.

The energy density of the gauge field is supposed to be constant and, therefore, the total field energy is linearly proportional to the distance. So, the potential (at large distances) is linearly rising with separation[1],

$$E(r) \to Kr, \tag{2.85}$$

where $r$ denotes the separation between the two quarks and the constant $K$ is the so-called string tension. When the potential reaches the energy which is necessary to create a new quark anti–quark pair it becomes energetically favorable to break the string and produce an new quark–anti-quark pair. Now, we have two quark–anti-quark pairs which will also break into new pairs if we try again to separate the quarks from the anti–quarks, and so on. At the end the original string is broken down into several strings which all have about the same length ($\sim 1\,\mathrm{fm}$). We see that due to this string breaking effects the potential between the original quark and anti-quark will be modified, which is known as the screening. Because of the screening it is very difficult to determine a proper order parameter for the confinement phase transition.

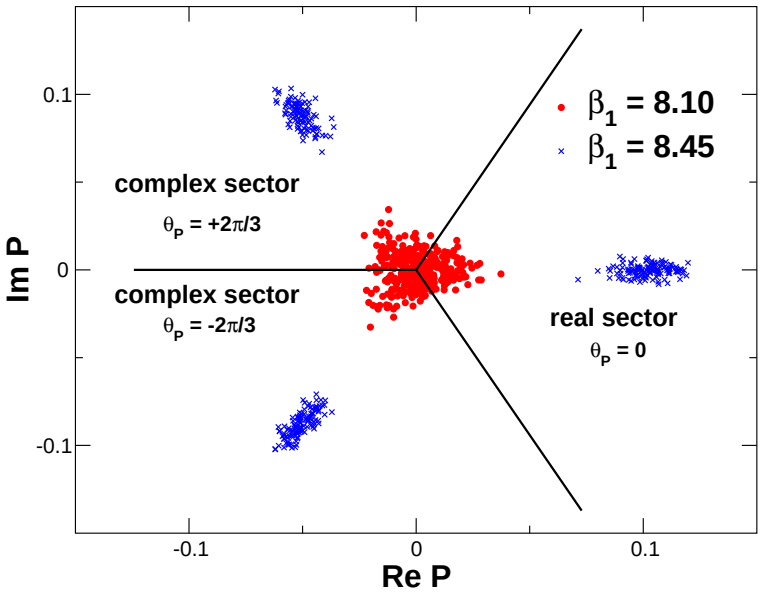


**Figure 2.2:** The Polyakov loop in the complex plane. Every data point corresponds to a single gauge field configuration of a $20^3 \times 6$ lattice. We plotted ensembles with two different values of $\beta$ using the Lüscher-Weisz gauge action. The data points of the ensemble with $\beta = 8.10$ cluster around zero which means that we are in the confinement phase while for $\beta = 8.45$ the data points cluster around the phases of the $Z_3$ group which signals deconfinement.

But there is one exception. If we forbid the creation of new quark–anti-quark pairs we will have a linearly increasing potential for long distances which improves the situation much. Forbidding pair creation corresponds to the quenched approximation

[1]Note that we are interested in the low energy regime, which means the length scale is large.

we use in our lattice calculations. In Sec. 2.1.3 we noted that this approximation reduces the computer time for lattice calculations enormously. As we will see soon, quenching has the further advantage that we can find a well defined order parameter for the confinement phase transition. The property of an order parameter is to divide the parameter space (of the order parameter) into two regions where each region correspond to one of the two phases. What we want to have is a relation between the order parameter and the temperature of the system. We, then, can determine the critical temperature $T_c$ where the phase transition occurs.

Let us become more quantitatively and present an order parameter for confinement, namely the Polyakov loop,

$$P(\boldsymbol{x}) = \frac{1}{3}\mathrm{Tr} P \exp\left\{ \mathrm{i}g \int_0^{1/T} \mathrm{d}t A_4(\boldsymbol{x}, t) \right\}, \tag{2.86}$$

where $P$ denotes path ordering and $1/T$ is the extent in time direction. We are using the Euclidean time description so $A_4(\boldsymbol{x}, t)$ denotes the time component of the gauge field. Remember, because we like to have QCD at finite temperature we use a lattice with finite extent in time direction and periodic boundary conditions. The temperature $T$ is related to the extent $L_t$ in time direction by $T = 1/L_t$. The lattice version of the Polyakov loop is quite simple. For a given spatial point $\boldsymbol{x}$ we just have to multiply all link variables $U_{(\boldsymbol{x},x_4),4}$ in time direction and take the trace,

$$P_{\boldsymbol{x}} \equiv \mathrm{Tr}\left( \prod_{x_4=1}^{L_t} U_{(\boldsymbol{x},x_4),4} \right). \tag{2.87}$$

It is no problem to calculate the Polyakov loop from lattice data. But let us return to the Polyakov loop and its role as an order parameter of the confinement phase transition. In Ref. [2] it is shown that one can relate the free energy which is necessary to bring in a static color triplet test charge into the gauge field to the Polyakov loop,

$$\mathrm{e}^{-\frac{\Delta E}{T}} \sim |\langle P \rangle| \equiv \left| \left\langle \frac{1}{L_s^3} \sum_{\boldsymbol{x}} P_{\boldsymbol{x}}, \right\rangle \right|. \tag{2.88}$$

We denote the change of the free energy by $\Delta E$ and $\langle P \rangle$ is the expectation value of the Polyakov loop. The lattice extent in the spatial directions is denoted by $L_s$. Let us see how we have to interpret this equation. Assume that we are in the deconfined phase. That means a color triplet charge can be easily put into the gauge field. This costs no energy, so $\Delta E$ is zero. For the expectation value of the Polyakov loop this means it has to be finite. Let us try the other way round. If we are in the confined phase we cannot bring in a single color triplet. We only can bring in color singlets. The amount of energy which is necessary to bring in a color triplet is infinite. The exponential in Eq. (2.88), therefore, vanishes and also the expectation value of the Polyakov loop does. We illustrate the behavior of the Polyakov loop in Fig. 2.2 where we plotted two lattice ensembles with different values of $\beta$. The ensemble with $\beta = 8.10$ corresponds to a temperature below the critical temperature $T_c$ of the phase transition while for

$\beta = 8.45$ the temperature is above $T_c$. We nicely see that the Polyakov loop for $T < T_c$ clusters around zero which signals that we are in the confined phase. For $T > T_c$ the Polyakov loop clusters around the elements of the $Z_3$ group. This means we are in the deconfined phase.

Let us focus on the group $Z_3$, the center group of SU(3). In general the center of a group contains all group elements which commute with all group elements. In the case of QCD we have a SU(3) group and the corresponding center of this groups is $Z_3 = \{\exp(i2\pi k/3);\, k = 0, 1, 2\}$. The gluonic action in QCD has a global $Z_3$ symmetry. This means the gluonic action is invariant under the following transformation

$$U_{(\boldsymbol{x},x_4),4} \to z\, U_{(\boldsymbol{x},x_4),4} \quad (x_4 \,\text{fixed}), \quad z \in Z_3, \tag{2.89}$$

where all transformations occur on a given temporal hyperplane, i.e. for a fixed $x_4$. From this transformation law it is clear that the gluonic action is invariant under such transformations. It is also clear that any closed loop which crosses that temporal hyperplane ($x_4 = \text{const.}$) the same number of times in positive as in negative direction will be left invariant as well. This may not be the case if we consider a product of link variables along a closed loop which goes around the torus, as it is the case for the Polyakov loop. Accordingly, the Polyakov loop transforms like

$$P_{\boldsymbol{x}} \to z\, P_{\boldsymbol{x}}. \tag{2.90}$$

Consider now the case that the ground state is invariant under $Z_3$ transformations. Then, configurations related by $Z_3$ transformations show up with the same probability. Hence, we have $\sum_k \exp(i2\pi k/3) = 0$ the expectation value of the Polyakov loop has to vanish. On the other hand, a nonzero expectation value means that the $Z_3$ symmetry is broken. We see, in the deconfinement phase the $Z_3$ symmetry is broken while in the confined phase the symmetry is restored [19].

Since the transformation defined in Eq. (2.89) leaves the action invariant the three different $Z_3$ sectors are equivalent. This is not the case for the spectrum of the Dirac operator. Notice that the boundary conditions of the fermions are changed by an $Z_3$ transformation [20]. The usual anti-periodic boundary conditions, see Sec. 2.2,

$$\psi(x, 1/T) = -\psi(x, 0), \tag{2.91}$$

are twisted into,

$$\psi(x, 1/T) = -z\, \psi(x, 0). \tag{2.92}$$

Further, the change in the boundary conditions affects the Matsubara frequencies. Instead of

$$\omega_k = (2k + 1)\pi T \tag{2.93}$$

we have

$$\omega_k = ((2k + 1)\pi - \arg P)T. \tag{2.94}$$

In the free-field case the smallest eigenvalue of the Dirac operator has the value of the lowest Matsubara frequency. So for the real sector ($z = \exp(\mathrm{i}2\pi 0/3) = 1$) the smallest eigenvalue is $\pi T$ but for the complex sectors ($z = \exp(\pm\mathrm{i}2\pi/3)$) it is $\pi T/3$. We see, that in the free-field case the lowest eigenvalue of the Dirac operator in the real sector of the Polyakov loop is three times larger than in the complex sectors. We will come back to this result later on.

## 2.4 The Banks-Casher Relation

In the limit where the quark masses tend to zero (chiral limit) the QCD Lagrangian has an additional global symmetry. This so-called chiral symmetry is crucial for the mass spectrum of the light hadrons. Indeed, we expect QCD to be chirally symmetric for the lightest quarks since the masses of the lightest two (or three) quarks are small compared to the typical energy scale of QCD. The typical energy scale of QCD is $\sim 1$ GeV. So, compared to the quark masses of $m_{u,d} \sim 5$ MeV, $m_s \sim 100$ MeV, $m_c \sim 1.3$ GeV, ... this symmetry is approximately respected for the lightest two (or three) quarks. Nevertheless, chiral symmetry is not manifest in the mass spectrum. This is because the symmetry is spontaneously broken, so the ground state of QCD is not chirally symmetric. Because of this spontaneous symmetry breaking, massless Goldstone bosons show up in the mass spectrum [21]. These Goldstone bosons in fact had been verified experimentally. However, since chiral symmetry is only approximately respected the experimentally found Goldstone bosons acquire a small mass. Let us consider the case $N_f = 3$. The group $\mathrm{SU}(3) \times \mathrm{SU}(3)$ of chiral symmetry is broken down to SU(3). Therefore, according to the Goldstone theorem, we obtain 8 massless Goldstone bosons for the 8 broken generators of the SU(3) group and, in principle, another one for the breakdown of $\mathrm{U}(1) \times \mathrm{U}(1) \to U(1)$. Note that for the latter Goldstone boson one has found a particle with the correct quantum numbers but the mass of this particle is too heavy. This riddle goes under the name of the $\mathrm{U}_A(1)$ puzzle but is beyond the scope of this thesis.

Let us see what impact chiral symmetry has on our theory. First of all we focus on the Dirac operator. We introduce the projection operators $P_{R/L} = (\mathbb{1} \pm \gamma_5)/2$ acting on the quark fields. The eigenstates of $P_{R/L}$ define the chiral basis $\{\varphi_R, \varphi_L\}$. The (flavor) group which corresponds to chiral symmetry is $\mathrm{SU}_R(N_f) \times \mathrm{SU}_L(N_f)$. So in the chiral limit where the QCD Lagrangian respects this symmetry the right- and left-handed components, $\varphi_R$ and $\varphi_L$, can be rotated independently in flavor space. Because $\not{D}$ anti–commutes with $\gamma_5$, $\{\not{D}, \gamma_5\} = 0$, the Dirac operator has a block diagonal structure in the chiral basis,

$$\not{D} = \begin{pmatrix} 0 & \mathrm{i}T \\ \mathrm{i}T^\dagger & 0 \end{pmatrix}. \tag{2.95}$$

The determinant in Eq. (2.12) then has the form

$$\det(\not{D} + m_f) = \det(TT^\dagger + m_f^2). \tag{2.96}$$

We see that the Dirac operator only couples left-handed to right-handed components while a mass term couples components of the same handedness. Note that the (Euclidean) Dirac operator is anti–hermitian, $\not{D}^\dagger = -\not{D}$, and, therefore, the nonzero eigenvalues of $\mathrm{i}\not{D}$ come in pairs $\pm\lambda_i$ (with $\lambda_i$ real). The corresponding eigenvectors fulfill the relation $\gamma_5\psi_\lambda = \psi_{-\lambda}$. Note that the Dirac operator also can have zero modes. These zero modes have definite chirality which means that they are eigenvector of $\gamma_5$, $\gamma_5\psi_0 = \pm\psi_0$.

We noted in the beginning of this section that we expect chiral symmetry to be spontaneously broken. The order parameter for this phase transition is the chiral condensate $\langle\bar{q}q\rangle$. In the following we will relate the chiral condensate to the eigenvalue density $\rho(\lambda)$ of the Dirac operator. This relation turns out to be a useful tool in lattice QCD which will help us to determine the critical point of the chiral phase transition. The chiral condensate for a given gauge field configuration is given by

$$\langle\bar{q}q\rangle = \mathrm{i}\int \mathrm{d}^4x\,\mathrm{Tr}\,S(x,x) = -\mathrm{i}\int \mathrm{d}^4x \sum_\lambda \frac{\mathrm{Tr}\,\psi_\lambda^\dagger(x)\psi_\lambda(x)}{\lambda + \mathrm{i}m} = -\sum_{\lambda>0}\frac{2m}{\lambda^2+m^2}, \tag{2.97}$$

where $S(x,y) = -\langle x|\mathrm{i}\not{D}^{-1}|y\rangle$ is the quark propagator and $\psi_\lambda(x)$ are normalized eigenfunctions of $\not{D}$ with corresponding eigenvalues $\lambda$. In the last expression we excluded the zero modes in the summation because they do not contribute to the quark condensate. This is because it is believed that the number of zero modes scales as $V^{1/2}$. So the density of zero modes scales like $1/V^{1/2}$ and, therefore, vanishes in the thermodynamic limit. This means that zero modes do not contribute to the eigenvalue density and chiral condensate, respectively, while the number of nonzero eigenvalues scales as $V$ and, thus, the density of nonzero modes does not necessarily vanish.

The chiral condensate $\langle\bar{q}q\rangle$ in Eq. (2.97) still has to be averaged over the gauge ensemble and the chiral and thermodynamic limits ($m \to 0$ and $V \to \infty$) have to be taken. To account for the ensemble average we introduce the spectral density $\rho(\nu) = \sum_\lambda \delta(\nu - \lambda)$ and obtain

$$\langle\bar{q}q\rangle = -\int_0^\infty \mathrm{d}\lambda\,\rho(\lambda)\,\frac{2m}{\lambda^2+m^2}. \tag{2.98}$$

Now we have to be careful in which order to take the limits. In a finite system the eigenvalue density always vanishes around zero, so there is no spontaneous symmetry breaking. Only in the thermodynamic limit we can have a finite density of eigenvalues close to zero. The situation is similar to that of a system of spins without an external field. In the system has finite extensions it is tunneling between the two ground states which means that the magnetization is zero. Only in the thermodynamic limit spontaneous symmetry breaking can occur and the system can choose a preferred direction for its magnetization.

So, if we take the thermodynamic limit first $\rho$ can be finite near zero and, therefore, the $\lambda$ integration is infrared divergent as $m \to 0$. Finally, we can have a finite quark

condensate,

$$\langle q\bar{q}\rangle = -\lim_{m\to 0}\int_0^\infty \mathrm{d}\lambda\,\rho(\lambda)\,\frac{2m}{\lambda^2+m^2} = -\pi\rho(\lambda=0). \tag{2.99}$$

This relation Banks and Casher derived first in 1980 [22] and it is known as the Banks–Casher relation. The absolute value of the chiral condensate is denoted by $\Sigma$. Note that if the condition

$$mV\Sigma \gg 1 \tag{2.100}$$

is satisfied the Banks–Casher relation still applies [23]. We will come back to this in Sec. 3.2. Remember, if there is a non–vanishing density of eigenvalues of the Dirac operator around zero then the chiral condensate is nonzero and chiral symmetry is broken while in the other case chiral symmetry is restored.

## 2.5 Instantons and Chiral Symmetry Breaking

In the last section we have discussed the Banks–Casher relation and its importance for chiral symmetry breaking. Now, that we have presented an order parameter for the chiral phase transition we would like to get some insight into the mechanism of chiral symmetry breaking. This topic is intimately connected to the subject of instantons [24]. Before we will go into more details let us first get familiar with the concept of instantons.

### 2.5.1 Classical Vacua

Instantons describe the tunneling between the classical vacua of a theory. Before we will study tunneling let us start with the classical vacua of SU($N$) gauge theory. The Yang-Mills Hamiltonian is given by

$$H = \frac{1}{2}\int \mathrm{d}^3x(\boldsymbol{E}^a\cdot\boldsymbol{E}^a + \boldsymbol{B}^a\cdot\boldsymbol{B}^a) \tag{2.101}$$

where the electric and magnetic fields $E_i^a$ and $B_i^a$ are defined by

$$E_i^a = F_{i0}^a, \quad B_i^a = \epsilon_{ijk}F_{jk}^a, \quad i,j,k = 1,2,3 \quad a = 1,2,\ldots,N_c. \tag{2.102}$$

$F_{\mu\nu}$ is the field strength tensor defined in (2.7). It is convenient to use the temporal gauge $A_0 = 0$. Note that we use the abbreviation $A_i \equiv A_i^a\lambda^a/2$ of (2.5). In that gauge the conjugate momentum is just the electric field $E_i = \partial_0 A_i$. Note that the classical vacuum corresponds to configurations with field strength zero. In the Abelian case, i.e. in electrodynamics, these are just configurations with constant potential. In the non-Abelian case this is no longer true. All fields which are "pure gauge",

$$A_i = \mathrm{i}\,U(\boldsymbol{x})\,\partial_i U^\dagger(\boldsymbol{x}), \tag{2.103}$$

have field strength zero. The gauge transformations $U(\boldsymbol{x})$ can be classified by their global topological properties. Let us restrict ourselves to fields satisfying

$$\lim_{|\boldsymbol{x}|\to\infty} U(\boldsymbol{x}) = \mathbb{1}. \tag{2.104}$$

Such fields can be classified by their winding number which is defined by

$$n_W = \frac{1}{24\pi^2}\int \mathrm{d}^3x\, \epsilon^{ijk}\,\mathrm{Tr}[(U^\dagger\partial_i U)(U^\dagger\partial_j U)(U^\dagger\partial_k U)]. \tag{2.105}$$

To illustrate the meaning of this integer let us consider the gauge group SU(2) [25]. We can parameterize this group as follows

$$U(\boldsymbol{x}) = u_0\,\mathbb{1} + \mathrm{i}\,\boldsymbol{u}\cdot\boldsymbol{\sigma}. \tag{2.106}$$

The components of $\boldsymbol{\sigma} = (\sigma_x, \sigma_y, \sigma_z)$ are the Pauli matrices and the components of $u = (u_0, \boldsymbol{u})$ are real and normalized by $u_0^2 + \boldsymbol{u}^2 = 1$. From this parameterization we easily can see that the SU(2) group is homeomorphic to the $\mathrm{S}_3$ sphere which is defined by $u_0^2 + u_1^2 + u_2^2 + u_3^2 = 1$. But $\mathrm{S}_3$ is also homeomorphic to $\mathbb{R}^3 \cup \{\infty\}$. That means that the gauge transformation $U(\boldsymbol{x})$ for the gauge group SU(2) maps $\mathrm{S}_3$ to $\mathrm{S}_3$. These mappings can be classified by equivalence classes characterized by an integer. The integer counts how many times the group manifold is covered. Note that in the general case of the gauge group $\mathrm{SU}(N_c)$ the results we obtained above are the same. Note that we also can express the winding number in terms of the gauge fields which is then called Chern-Simons characteristic

$$n_{CS} = \frac{1}{16\pi^2}\int \mathrm{d}^3x\, \epsilon^{ijk}\left(A_i^a\partial_j A_k^a + \frac{1}{3}f_{abc}A_i^a A_j^b A_k^c\right). \tag{2.107}$$

We see that there exist infinitely many classical vacua which are topologically different. Because of the topological difference we can not go from one vacuum to another by means of a continuous gauge transformation. This means that there is no connecting path of two topologically different vacua where the energy is zero all the time. Classically, we cannot go from one vacuum to another but quantum mechanically there is the possibility of tunneling. Instantons in gauge theory correspond to the tunneling amplitude between two topologically different vacua.

### 2.5.2 Tunneling

Let us look for a tunneling path in Yang-Mills theory which connects two different vacua. It is clear what we have to do. As in quantum mechanics, the tunneling amplitude is given by the classical solution of the (Euclidean) equations of motion. To find such solutions let us rewrite the gauge part of the action in (2.11)

$$S_g = \frac{1}{4g^2}\int \mathrm{d}^4x F_{\mu\nu}^a F_{\mu\nu}^a = \frac{1}{4g^2}\int \mathrm{d}^4x\left[\pm F_{\mu\nu}^a \widetilde{F}_{\mu\nu}^a + \frac{1}{2}\left(F_{\mu\nu}^a \mp \widetilde{F}_{\mu\nu}^a\right)^2\right], \tag{2.108}$$

where the dual field strength tensor $\widetilde{F}^a_{\mu\nu}$ is defined by

$$\widetilde{F}^a_{\mu\nu} = \frac{1}{2}\,\epsilon_{\mu\nu\rho\sigma} F^a_{\mu\nu} \tag{2.109}$$

and we made the convenient rescaling of the fields $A_\mu \to \frac{1}{g} A_\mu$. As we will see below the first term of the last equation in (2.108) is topologically invariant. From this and from the observation that the last term is always positive we can see that the action is minimal if the field is self-dual or anti self-dual

$$F^a_{\mu\nu} = \pm \widetilde{F}^a_{\mu\nu}. \tag{2.110}$$

Note that self-dual fields automatically fulfill the equation of motion $D_\mu F_{\mu\nu} = 0$ where $D_\mu$ is the covariant derivative.

Let us return to the first term in Eq. (2.108) and its topological invariance. We define the topological charge by

$$Q = \frac{1}{32\pi^2} \int \mathrm{d}^4x F^a_{\mu\nu} \widetilde{F}^a_{\mu\nu}. \tag{2.111}$$

The corresponding action is then given by

$$S_g = \frac{8\pi^2}{g^2} |Q|. \tag{2.112}$$

We now will show that for field configurations with finite action $Q$ is an integer. For this propose we will use the fact that the integrand in (2.111) can be written as a total derivative.

$$Q = \int \mathrm{d}^4x \partial_\mu K_\mu, \tag{2.113}$$

$$\text{with } K_\mu = \frac{1}{16\pi^2} \epsilon_{\mu\alpha\beta\gamma} \left( A^a_\alpha \partial_\beta A^a_\gamma + \frac{1}{3} f_{abc} A^a_\alpha A^b_\beta A^c_\gamma \right). \tag{2.114}$$

We know that for configurations with finite action the gauge field has to be pure gauge at infinity, that means as $|x| \to \infty$ we have $A_\mu \to \mathrm{i}\, U \partial_\mu U^\dagger$. Making a similar analysis to that we made above shows that the mappings of the sphere $\mathrm{S}_3$ ($|x| \to \infty$) into the gauge group can also be classified by an integer winding number $n$. If we insert $A_\mu = \mathrm{i} U \partial_\mu U^\dagger$ into Eq. (2.113), we find that $Q = n$. Note that if the gauge field falls off rapidly at spatial infinity we find

$$Q = \int_{-\infty}^{\infty} \mathrm{d}t \frac{\mathrm{d}}{\mathrm{d}t} \int \mathrm{d}^3x K_0 = n_{CS}(t = \infty) - n_{CS}(t = -\infty). \tag{2.115}$$

From this we see that field configurations with $Q \neq 0$ connect topologically different vacua.

Let us now construct an explicit solution for $Q = 1$. We will start from the simplest winding number $n = 1$. We begin with $A_\mu = \mathrm{i}\, U \partial_\mu U^\dagger$ with $U = \mathrm{i}\, \hat{x}_\mu \sigma^+_\mu$, where $\sigma^\pm_\mu = (\boldsymbol{\sigma}, \mp \mathrm{i})$ and $\hat{x}_\mu$ is normalized to one. It follows that

$$A^a_\mu = 2\, \eta_{a\mu\nu} \frac{x_\nu}{x^2}, \tag{2.116}$$

where we have used the 't Hooft symbols $\eta_{a\mu\nu}$ and $\bar{\eta}_{a\mu\nu}$,

$$\eta_{a\mu\nu} = \epsilon_{a\mu\nu} + \delta_{a\mu}\delta_{\nu 4} - \delta_{a\nu}\delta_{\mu 4}, \tag{2.117}$$

$$\bar{\eta}_{a\mu\nu} = \epsilon_{a\mu\nu} - \delta_{a\mu}\delta_{\nu 4} + \delta_{a\nu}\delta_{\mu 4}. \tag{2.118}$$

We make the ansatz $A^a_\mu = 2\,\eta_{a\mu\nu}\,x_\nu\,\frac{f(x^2)}{x^2}$ where $f$ has to satisfy the boundary condition $f \to 1$ as $x^2 \to \infty$. Putting this into the self-duality equation in (2.110) we find

$$f(1-f) - x^2 f' = 0. \tag{2.119}$$

The solution of this equation is $f = \frac{x^2}{x^2+\rho^2}$ where the integration constant $\rho$ represents the size of the instanton. For the gauge field we obtain

$$A^a_\mu(x) = \frac{2\,\eta_{a\mu\nu}\,x_\nu}{x^2+\rho^2}. \tag{2.120}$$

which is known as the Belavin-Polyakov-Schwartz-Tyupkin instanton solution [26]. To obtain a solution for $Q = -1$ we have to replace $\eta_{a\mu\nu}$ by $\bar{\eta}_{a\mu\nu}$. Finally, the corresponding field strength is

$$(F^a_{\mu\nu})^2 = \frac{192\rho^4}{(x^2+\rho^2)^4}. \tag{2.121}$$

We see that the instanton solution is well localized and $F^a_{\mu\nu}$ falls off for $x$ as $1/x^4$. Because the instanton is also localized in time it was named like a quasi-particle.

The instanton has several degrees of freedom. In the case of SU(2) we have the instanton size $\rho$, the position $z_\mu$ of the instanton, and three further parameters which determine the color orientation. The color orientation in group space can be determined by some SU(2) matrix $U$ which acts on the field, $A_\mu \to U A_\mu U^\dagger$, or by the rotation matrix $R^{ab} = \frac{1}{2}\mathrm{Tr}(U\sigma^a U^\dagger \sigma^b)$ with $A^a_\mu \to R^{ab}A^b_\mu$. Note that the instanton is rotationally invariant and therefore ordinary rotations do not generate different solutions. For SU(3) we can embed the SU(2) instanton solution. We note that for $|Q| = 1$ there are no new SU(3) solutions. Only the number of the degrees of freedom increases as for the color orientation we obtain 7 free parameters (not 8 because one generator of the SU(3) leaves the instanton invariant).

Let us return to the subject of tunneling. The transition amplitude for a tunneling process of two topologically different vacua is given by

$$W_T = \left\langle j\middle|\mathrm{e}^{-H\tau}\middle|i\right\rangle = \int \mathrm{D}[A]\ \mathrm{e}^{-S_g}. \tag{2.122}$$

Let us expand the field around the classical solution, $A_\mu = A^{\mathrm{kl}}_\mu + \delta A_\mu$, and express Eq. (2.122) in terms of this decomposition,

$$W_T = \mathrm{e}^{-S_g(A^{\mathrm{kl}})} \int \mathrm{D}[\delta A]\,\mathrm{e}^{-\frac{1}{2}\,\delta A\,\frac{\delta^2}{\delta x^2}S_g\big|_{A^{\mathrm{kl}}}\,\delta A + \cdots}. \tag{2.123}$$

We see that the linear term vanishes. This is simply because $A_\mu^{\rm kl}$ fulfills the equation of motion. We put the constant term of the expansion in front of the integral. Note that $S_g(A^{\rm kl})$ is given by $S_g = 8\pi^2 \frac{|Q|}{g^2}$. Therefore, we obtain for the tunneling amplitude for our instanton solution we just constructed ($Q = 1$),

$$W_T \sim \mathrm{e}^{-\frac{8\pi^2}{g^2}}. \tag{2.124}$$

We now can take into account the fluctuations around the classical solution. We therefore have to evaluate the following path integral

$$\int \mathrm{D}[\delta A]\, \mathrm{e}^{-\frac{1}{2}\,\delta A\, \frac{\delta^2}{\delta x^2} S_g\big|_{A^{\rm kl}}\, \delta A}. \tag{2.125}$$

The calculation of this path integral is rather tedious, so we refer the interested reader to Ref. [27].

### 2.5.3 Zero Modes

The most important feature of an instanton for our purposes is that it possesses a fermionic zero mode satisfying $\mathrm{i}\not{D}\psi_0 = 0$. Before we will discuss the importance of this fermionic zero mode and its relation to chiral symmetry breaking we like to sketch how to calculate the wave function of the zero mode. We restrict ourselves to the case of SU(2). Let us start with the squared Dirac operator which can be written as follows

$$(\mathrm{i}\not{D})^2 = \left(-D^2 + \frac{1}{2}\sigma_{\mu\nu}F_{\mu\nu}\right), \tag{2.126}$$

where $\sigma_{\mu\nu} = \frac{\mathrm{i}}{2}[\gamma_\mu, \gamma_\nu]$. Let us use the relation $\sigma_{\mu\nu}F^{\pm}_{\mu\nu} = \mp\gamma_5\sigma_{\mu\nu}F^{\pm}_{\mu\nu}$ for (anti) self-dual fields $F^{\pm}_{\mu\nu}$. Then, for a self-dual field we obtain with the help of the Dirac equation $\mathrm{i}\not{D}\psi = 0$ and the decomposition into left-handed and right-handed fermion fields $\psi = \chi_L + \chi_R$ the following equations

$$\left(-D^2 + \frac{1}{2}\sigma_{\mu\nu}F^{+}_{\mu\nu}\right)\chi_L = 0, \quad -D^2\chi_R = 0. \tag{2.127}$$

The same equation holds for anti-self-dual fields if we exchange ($+ \leftrightarrow -$, $L \leftrightarrow R$). We see that $\chi_R$ has to vanish since $-D^2$ is a positive operator. We see that the zero mode is left-handed in the background field of an instanton and left-handed in an anti-instanton background. If we solve the equation above, we obtain for the wave function of the fermionic zero mode [28, 29]

$$\psi_0(x) = \frac{\rho}{\pi}\,\frac{1}{(x^2+\rho^2)^{\frac{3}{2}}}\,\frac{\gamma\cdot x}{\sqrt{x^2}}\,\frac{1+\gamma_5}{2}\,\phi, \tag{2.128}$$

where $\phi^{\alpha m} = \frac{1}{\sqrt{2}}\epsilon^{\alpha m}$ is a constant spinor in which the SU(2) color index $\alpha$ is coupled to the spin index $m = 1, 2$. Again, the SU(3) solution can be obtained by embedding.

### 2.5.4 Instantons and Chiral Symmetry Breaking

Because of the presence of fermions single instantons cannot exist in the chiral limit. This can be seen as follows. The tunneling amplitude in (2.122) is modified by the fermions,

$$W_T = \left\langle j \middle| \mathrm{e}^{-H\tau} \middle| i \right\rangle = \int \mathrm{D}[A]\,\mathrm{D}[\bar{\psi}]\,\mathrm{D}[\psi]\ \mathrm{e}^{-S_g - S_q}, \tag{2.129}$$

where the Euclidean action $S_q$ for $N_f$ fermions is given by

$$S_q = \sum_{f=1}^{N_f} \int \mathrm{d}^4x\ \bar{\psi}_f(x)(\not{D} + m_f)\psi_f(x). \tag{2.130}$$

Integrating out the quark fields we obtain

$$W_T = \int \mathrm{D}[A]\ \mathrm{e}^{-S_g} \prod_f \det[\not{D} + m_f]. \tag{2.131}$$

The determinant now can be written in terms of the eigenmodes of the Dirac operator, $\mathrm{i}\not{D}\psi_\lambda = \lambda\psi_\lambda$. Using the fact that the eigenvalues $\lambda$ come in pairs of $\pm\lambda$ we obtain

$$\det[\not{D} + m] = m^\nu \prod_{\lambda>0} (\lambda^2 + m^2), \tag{2.132}$$

where $\nu$ is the number of zero modes. We see that in the chiral limit ($m_f \to 0$) the tunneling amplitude vanishes. However, we know that chiral symmetry is spontaneously broken which means that we can have a nonzero tunneling amplitude anyway.

Let us consider chiral symmetry breaking in more detail, see also Refs. [30, 31]. In Sec. 2.4 we presented an order parameter for the chiral phase transition, the chiral condensate

$$\langle \bar{q}q \rangle = \mathrm{i} \int \mathrm{d}^4x\, \mathrm{Tr}[S(x,x)], \tag{2.133}$$

which is the probability amplitude for a quark to flip its chirality. In the chiral limit, only the zero modes do contribute to the quark condensate. Since the quark propagator for the zero mode is given by

$$S(x,y) = -\frac{\psi_0(x)\psi_0^\dagger(y)}{im} \tag{2.134}$$

the contribution of a single instanton is just $-1/m$. The contribution of an ensemble of (isolated) instantons to the chiral condensate then is given by

$$\langle \bar{q}q \rangle = -\frac{N}{V}\frac{1}{m}, \tag{2.135}$$

where $N/V$ is the density of instantons. Because the density of the instantons behaves like

$$\frac{N}{V} \sim m^{N_f} \tag{2.136}$$

we can see that for $N_f > 1$ the chiral condensate vanishes. So at a first look we may think that instantons cannot be used for the description of chiral symmetry breaking. But this is wrong as we shall see in the following. Let us consider an ensemble of instantons. If the instantons are well separated we can treat them as single instantons which do not interact with each other. In this case, as we just have seen, the instantons lead to a vanishing chiral condensate. On the other hand, if the instantons are not so well separated they begin to interact, not only through their gauge fields but also through fermionic exchanges. Without going into details we will present an illustrative picture how an ensemble of interacting instantons describe chiral symmetry breaking. We make use of an analogy where instantons correspond to atoms and light quarks correspond to valence electrons.

We can think of instantons as atoms which have an unsaturated bond. In principle massive quarks can saturate the bonds but because of chiral symmetry we have only massless quarks. So the simplest object which is neutral in this sense is an instanton-anti–instanton (IA) molecule. If the interaction between instantons and anti–instantons is strong the formation of IA molecules is favored. The zero modes of the Dirac operator in the background of the instanton and anti–instanton which form a molecule are strongly mixing which means that the eigenvalue density near zero vanishes. From our discussion in Sec. 2.4 we know that this means that chiral symmetry is restored. For low instanton densities this phase can be characterized as a gas phase consisting of IA molecules. Indeed, lattice simulations confirm that the instanton density is decreasing for large temperatures, i.e. in the chirally symmetric phase [32, 33]. For the localization properties of the eigenmodes of the Dirac operator this means that the quarks, which are bound to the IA molecules, are localized. On the other hand, for weakly interacting instantons the corresponding zero modes are mixing weakly. Therefore, the eigenvalue density near zero is nonzero and chiral symmetry is broken. The instanton density is supposed to be constant which leads us to the picture of an instanton liquid. The zero modes of the instantons become collective in this liquid and therefore the quarks are delocalized. In terms of our analogy we can say that the conductivity is nonzero.

Let us summarize this picture of chiral symmetry breaking. Chiral symmetry breaking can be described by means of an ensemble of interacting instantons and anti–instantons. In the high temperature phase where chiral symmetry is restored the instantons are supposed to interact strongly forming IA molecules. The zero modes are mixing strongly resulting in a vanishing eigenvalue density near zero. According to the Banks-Casher relation chiral symmetry is therefore restored. The density of the instantons is low and one speaks of an instanton gas consisting of IA molecules. In the low temperature phase chiral symmetry is spontaneously broken. We expect that the instantons are weakly interacting building an instanton liquid. The zero modes are only mixing weakly which tells us that chiral symmetry is broken. Because

of the collective zero modes in this phase the eigenmodes of the Dirac operator are delocalized while for the chirally symmetric phase the quarks are localized. So, we expect as the instanton interaction gets stronger the system undergoes a phase transition from the instanton liquid to the instanton gas. This explains the mechanism of chiral symmetry breaking. Note that the localization properties can act as a signature for this picture and may help us to validate it. We will come back to this topic in Chapter 4.

# Chapter 3

# Chiral Symmetry and Confinement

Two main properties of QCD are the chiral and the confinement phase transition. For many years intense work has been invested and much progress has been achieved already. Nevertheless, there are still open questions which are subject of recent investigations. In this chapter we will aim at one specific question which we are going to formulate in the following.

## 3.1 The Connection between Chiral Symmetry and Confinement

Other than for example electrons, quarks are color charged. But this color charge we do not observe. In nature we only observe colorless states built from two or three quarks, but there exist no colored states. This property of QCD goes under the name of confinement. However, it is believed that QCD undergoes a phase transition. At high temperatures we expect QCD to exhibit a phase which allows colored charges to propagate freely. This phase is called deconfinement phase and is probed currently by heavy ion collisions. In lattice simulations we already observe this deconfinement phase. Anyway, the mechanism of the confinement phase transition remains unknown and is a major subject of current investigations in QCD.

On the other hand, the chiral phase transition is well understood. We have the very successful instanton picture of chiral symmetry breaking, see Sec. 2.5, in which the fermionic zero modes of the instantons play a crucial role. According to the Banks-Casher relation in Eq. (2.99) a non vanishing density of eigenvalues of the Dirac operator near to zero signals that chiral symmetry is broken while if the eigenvalue density is zero, chiral symmetry is restored. The zero modes of an ensemble of weakly interacting instantons and anti–instantons are mixing weakly and generate a finite eigenvalue density near zero indicating that chiral symmetry is broken. For larger temperature the instantons strongly interact with the anti–instantons. The result is that the eigenvalues are mixing strongly and the eigenvalue density near the origin disappears. Chiral symmetry is restored.

The interesting point about the confinement phase transition and the chiral phase transition is that we expect them to be related. From lattice studies [34] we know

that the critical point of both phase transitions should be at the same temperature. If the phase transitions are not related somehow this would be a very big accident which is hard to understand. The first guess, of course, leads to the instantons as they describe the chiral phase transition so well. Unfortunately, instantons cannot describe confinement. The reason is that the field of an instanton falls off too rapidly. It looks like a dipole field and falls off like $1/r^4$. (Although in three dimensions the instanton field looks like a monopole leading to confinement.) But we need a long range field to describe the heavy quark potential. Other promising objects are monopoles which are subject of recent investigations but this topic is beyond the scope of this thesis. We like to focus on a different, though related question which we will post in the following.

In Sec. 2.3 we found that the pure gauge action is $Z_3$ invariant which enabled us to define an order parameter of the confinement phase transition, namely the Polyakov loop. We have seen that in the deconfinement phase the Polyakov loop clusters around the elements of the $Z_3$ center group. We divided the complex plane of the Polyakov loop into the real sector where the real element of the center group lies, and the complex sector which contains the remaining two complex elements, see Fig. 2.2. As we already mentioned above the critical point of the chiral and of the confinement phase transition is at the same temperature. We now can raise the question whether the critical point for chiral phase transition depends on the $Z_3$ sector. What does this mean? For every temperature above $T_c$ we can divide our ensemble of gauge fields into two classes, gauge fields which have real or complex Polyakov loop. We can do this also below the critical temperature and let gauge field configurations with $-\pi/3 < \arg P < +\pi/3$ correspond to the real sector while the other configurations correspond to the complex sector. This split-up is, of course, arbitrary because the $Z_3$ symmetry is restored and configurations of different sectors are physically not distinguishable. We just introduce it for convenience. We want to study the question whether the critical point of the chiral phase transition calculated only from configurations of the real sector differs from $T_c$ calculated only from configurations of the complex sector. From a first look it seems that this cannot be the case because above we said that the critical point of the two phase transitions coincide. So, how should $T_c$ depend on the $Z_3$ sector? But, as we will see, this is in principle possible.

In "full" QCD (with dynamical fermions) the three sectors of the Polyakov loop are no longer equivalent. If we take a look at the Euclidean QCD partition function in Eq. (2.12) we see that the partition function can be written as an integral over the gauge fields weighted by the fermion determinant. So we can, in principle, determine the "full" QCD partition function from the quenched ensemble by re-weighting each configuration with its fermion determinant. Unfortunately, the fermion determinant is heavily fluctuating which means that in practice this approach is useless since the statistics currently are to small. Anyway, in principle we can perform this re-weighting procedure and we will find that configurations in the real sector of the Polyakov loop are favored (above $T_c$). This can be seen as follows. As we mentioned at the end of Sec. 2.3 the low-lying eigenvalues are about three times larger for configurations in the real sector than for configurations in the complex sector. Looking at the partition

function in (2.12) we see that, therefore, the determinant for configurations in the real sector of the Polyakov loop is larger which means that the weight in the partition function is larger for those configurations. Hence, the real sector of the Polyakov loop is favored.

But how does this affect the dependence of the critical point on the Polyakov loop sectors? The argument is the following: Because the real sector of the Polyakov loop is favored in "full" QCD the critical points of the confinement and chiral phase transitions should coincide for configurations in the real sector. But configurations in the complex sector, then, contribute only less to the partition function and, hence, it is possible that the critical points of the confinement and chiral phase transition differ. We see, although far from obvious, the critical points of the two phase transitions may actually depend on the $Z_3$ sector. If this really is the case, this observation could provide a crucial hint as to which microscopical field configurations are responsible for confinement and chiral symmetry breaking. We should expect that the mechanism which is responsible for the dependence of the critical point on the $Z_3$ sector is intimately connected to the coincidence of the critical point of the two phase transitions.

Indeed, Christ and Chandrasekharan in Ref. [35] found some evidence for different critical temperatures depending on the Polyakov loop sectors. Several possible mechanism were discussed [36, 37, 38]. They investigated the chiral condensate for staggered fermions. But staggered fermions have bad chiral properties. They only possess a residual chiral symmetry. We like to do a similar analysis but we will use chirally improved fermions. These fermions have much better chiral properties because the corresponding Dirac operator fulfills the Ginsparg-Wilson equation approximately. In particular they have numerically exact zero modes. These zero modes are also to a good approximation eigenvalues of $\gamma_5$. Neither is true for staggered fermions reflecting the bad chiral properties. Obviously, the topic is so interesting that it should be reinvestigated with chiral fermions. We will follow a different approach than the authors of Ref. [35] but we will perform our analysis also for staggered fermions to have a cross check.

## 3.2 The Low-Lying Eigenvalues of the Dirac Operator

In this section we will focus on the low-lying eigenvalues of the Dirac operator and their connection to the chiral phase transition. We know from Sec. 2.4 that the eigenvalue density of the Dirac operator near zero is an order parameter. If there is a finite eigenvalue density then chiral symmetry is broken. Else if the density vanishes chiral symmetry is restored. Let us have a deeper look at the eigenvalues for chirally improved fermions.

Chirally improved fermions approximately fulfill the Ginsparg-Wilson relation

$$\gamma_5 D + D\gamma_5 = a\, D\gamma_5 D, \tag{3.1}$$

where $D$ is the Dirac operator and $a$ is the lattice spacing. We see that as $a \to 0$ the Dirac operator anti–commutes with $\gamma_5$ reflecting chiral symmetry in the continuum.

Fermions on the lattice which respect the Ginsparg-Wilson equation are invariant under a lattice version of chiral transformations [32]. The eigenvalues of the Dirac operator of those fermions lie on a circle in the complex plane. The radius of the circle is of order $1/a$ and in the limit $a \to 0$ all eigenvalues lie on the imaginary axis. For illustration look at Fig. 3.1. We plotted the lowest eigenvalues for three different gauge field configurations with the Lüscher-Weisz gauge action. We see the eigenvalues lie in a good approximation on the so-called Ginsparg-Wilson circle. Note that for the chirally improved fermions only the low-lying eigenvalues lie on the Ginsparg-Wilson circle approximately. The larger the eigenvalues are the larger are the deviations

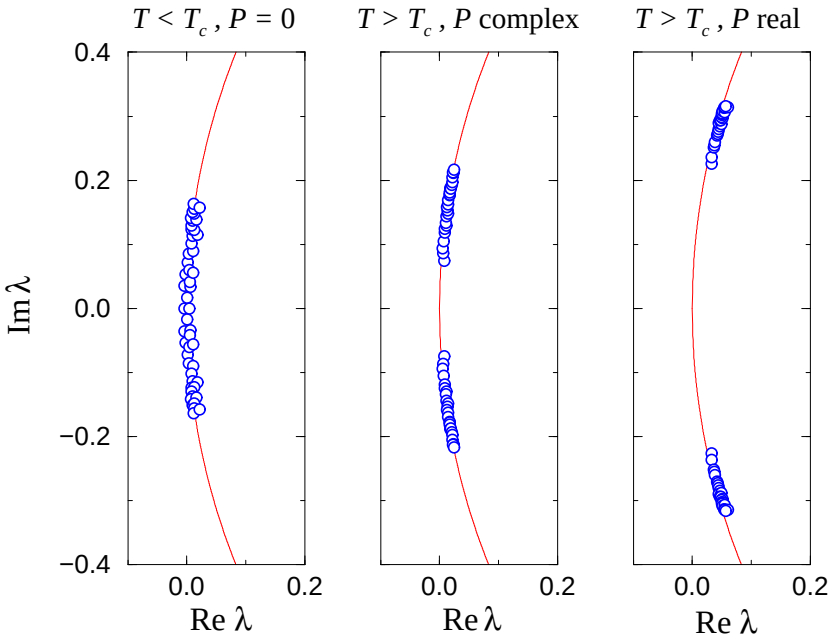


**Figure 3.1:** Smallest eigenvalues of the Dirac operator for 3 different gauge field configurations. The eigenvalues are plotted in the complex plane and lie on the Ginsparg-Wilson circle (red line). The plot on the left hand side corresponds to a configuration in the confined phase. We find a vanishing spectral gap. The center plot and the plot on the left hand show data for complex and real Polyakov loop, respectively. Both configurations belong to ensembles with the same temperature being above the critical temperature of the chiral and confinement phase transition. We see, the spectral gap is larger for the plot on the right hand side (real Polyakov loop).

from the circle. This is because chirally improved fermions fulfill only approximately the Ginsparg-Wilson relation. Note that it is also possible to have chirally improved fermions for which the large eigenvalues (large in the sense that they lie at the other side of the circle) lie on the Ginsparg-Wilson circle and the low-lying eigenvalues differ from the circle. If fermions fulfill the Ginsparg-Wilson equation exactly all eigenvalues of the Dirac operator lie exactly on the Ginsparg-Wilson circle.

Let us return to Fig. 3.1. On the plot on the left hand side we see the lowest eigenvalues of the Dirac operator for a typical gauge field configuration belonging to

an ensemble with temperature below the critical temperature $T_c$ of the confinement phase transition. The Polyakov loops for this ensemble cluster around zero which we denoted by $P = 0$. In the following we will refer to the critical temperature of the confinement phase transition as $T_c$ while the critical temperatures of the chiral phase transition we denote by $T_c^{real}$ and $T_c^{complex}$ for the real and complex Polyakov loop sector, respectively. Before we will focus on the lowest eigenvalues (the eigenvalues closest to zero) we note that the eigenvalues on the upper and lower half of the Ginsparg-Wilson circle are not independent but related by symmetry. (This is because in the continuum the eigenvalues of the Dirac operator come in purely imaginary pairs of $\pm i\lambda_i$.) Our first observation for the plot on the left hand side is that the lowest eigenvalues lie very close to zero. Because this is a typical configuration we have a finite density of eigenvalues near zero and, thus, we know from the Banks-Casher relation (2.99) that chiral symmetry is broken. We have seen what we already mentioned above, below $T_c$ we are in the confined phase and chiral symmetry is broken.

On the center plot and the plot on the right hand side of Fig. 3.1 we show two configurations of an ensemble with $T > T_c$. The center plot corresponds to a configuration which has the Polyakov loop in the complex sector while the plot on the right hand side shows a configuration with the Polyakov loop in the real sector. In both plots we clearly see that there is a gap between the lowest eigenvalue and zero. We call this gap the spectral gap, or sometimes simply the gap. Both configurations also represent the typical behavior of the ensemble, so we will find a vanishing density of the eigenvalues near zero. That means we are in the chirally symmetric phase for both configurations.

Note that chirally improved fermions also can have numerically exact zero modes. We already removed the zero modes from Fig. 3.1 because zero modes are not relevant for our considerations of the chiral phase transition, see Sec. 2.4. Therefore, we will omit the zero modes in all calculations below. We like to emphasize that the removal of the zero modes is important for the correct calculation of the chiral condensate. We will come back to this topic in more detail later on. Note, that for staggered fermions we cannot remove the zero modes from our calculations since staggered fermions have no exact zero modes. This may have some impact on the calculations Christ and Chandrasekharan have done.

Note that there is still a "microscopic" gap for the configuration in the plot on the left hand side in Fig. 3.1. By microscopic gap we mean that if we perform the ensemble average the eigenvalue density (microscopically) close to zero vanishes although on a scale of several level spacings the eigenvalue density is finite near to zero, see Eq. (2.100). The appearance of such a microscopic gap does not really mean that we are in the chirally symmetric phase. The reason for this gap is because we are on a finite lattice and, hence, chiral symmetry cannot be spontaneously broken at all. Only in the thermodynamic limit the microscopic gap will vanish and chiral symmetry can be spontaneously broken. However, by looking at Fig. 3.1 and Eq. (2.100) we detect that we have a criterion for the chiral phase transition anyway. If (on a scale of several level spacings) we find a finite density of eigenvalues of the Dirac operator we claim we are in the chirally broken phase while for a vanishing density we remain in the

chirally restored phase. We can find a critical temperature for this "phase transition". This critical temperature, then, will give the true critical temperature of the chiral phase transition in the thermodynamic limit. So from the scaling behavior of this critical temperature in the thermodynamic limit we should be able to extract the real critical temperature of the chiral phase transition at the end.

Finally, note that the spectral gap for configurations of ensembles with equal temperature is somewhat larger for configurations in the real Polyakov loop sector than for configurations in the complex Polyakov loop sector. If we consider the spectral gap as a function of the temperature we can say that the spectral gap opens up faster in the real Polyakov loop sector than in the complex Polyakov loop sector. We also do have an explanation for this behavior. At the end of Sec. 2.3 we found that the lowest eigenvalue of the Dirac operator in the free theory depends on the Polyakov loop sector. The lowest eigenvalue of a corresponding configuration with a real Polyakov loop is 3 times larger than for configurations with complex Polyakov loop sector. So, we expect to find a similar behavior also for the interacting theory. This claim is indeed correct as we see by comparing the plots in the center and on the right hand side in Fig. 3.1.

After this analysis of the low-lying eigenvalues of the Dirac operator we like to introduce a new order parameter for the chiral phase transition. From our discussion above it is clear that the spectral gap is an order parameter of the chiral phase transition. The spectral gap is correlated to the eigenvalue density of the Dirac operator near zero and, hence, to the chiral condensate. However, it is not clear how the relation between the two order parameters is in detail, but we can say for sure that if the spectral gap (averaged over the ensemble) vanishes, we must have a finite density of eigenvalues near zero and chiral symmetry is broken. On the other hand, if the (averaged) spectral gap is not zero then we must have a vanishing eigenvalue density near zero and chiral symmetry is restored. We will investigate the properties of the spectral gap as an order parameter in the following section.

## 3.3 The Distribution of the Spectral Gap

In this section we will explore the properties of the spectral gap and, finally, we will show how to use the spectral gap as an order parameter of the chiral phase transition. As noted in Sec. 3.2 a vanishing spectral gap indicates the spontaneous breaking of chiral symmetry, a finite gap signals that chiral symmetry is restored. Before we will go into details let us give a precise definition of the spectral gap. We see in Fig. 3.1 that the low-lying eigenvalues of the chirally improved fermions approximately lie on the Ginsparg-Wilson circle. We define the spectral gap $g_\lambda$ as the (positive) imaginary part of the smallest nonzero eigenvalue.

A good way to extract more information from the spectral gap might be to look how the values for the spectral gap are distributed. We, therefore, plotted a histogram of the spectral gap for three different ensembles with temperatures above, below, and approximately at the critical temperature. We did this both for the real and complex sector of the Polyakov loop, see Fig. 3.2. Let us concentrate on the upper plots in

Fig. 3.2. From left to right we see histograms of the spectral gap for $T < T_c$, $T \sim T_c$, and $T > T_c$, respectively. Let us start with the plot on the left hand side. We see that the spectral gap is peaked very close to zero. Note that the histogram of the spectral gap vanishes close to zero which means that the probability to find a configuration with a (very) small spectral gap tends to zero. The reason for this behavior is that

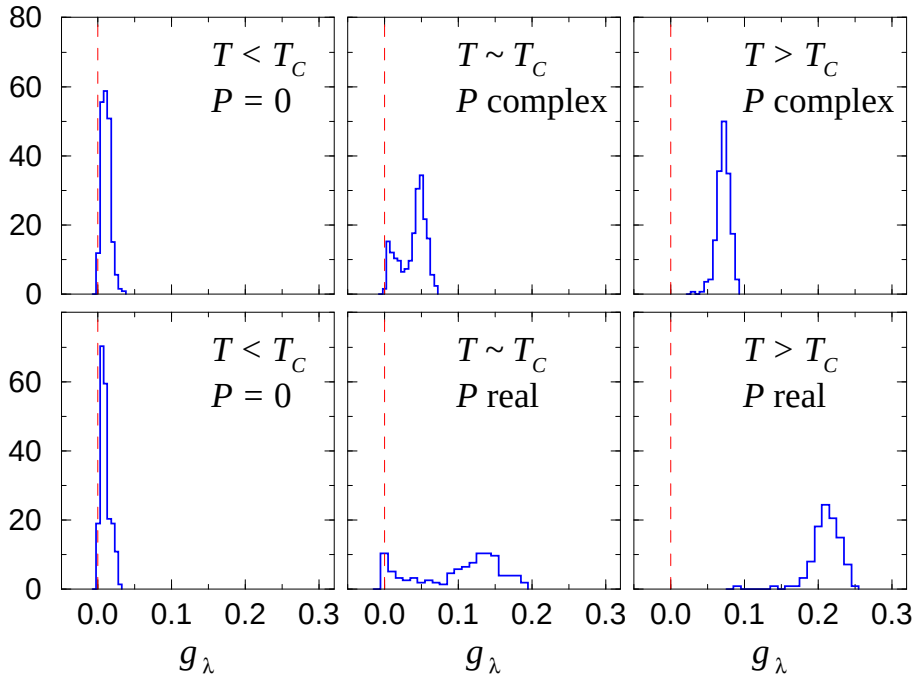


**Figure 3.2:** Histogram of the smallest (nonzero) eigenvalue. The upper plots correspond to configurations with complex Polyakov loop, the lower plots to those with real Polyakov loop. On the plots on the left (right) hand side we see that chiral symmetry is broken (restored). The center plots show that near the critical temperature both phases coexist.

we are on a finite lattice and, as we have discussed in Sec. 3.2, on a finite lattice there exists a microscopic gap. We conclude that the probability to find a configuration below the typical value of the microscopic gap has to vanish. We can estimate the typical value of the microscopic gap by the shift of the peak of the distribution away from zero. However, we can see that (beside the microscopic gap) the spectral gap also vanishes and, therefore, we are in the chirally broken phase. This is the expected behavior since we are well below $T_c$, the critical temperature of the confinement phase transition, and we know that chiral symmetry has to be broken there. Remember our discussion in Sec. 3.1.

Let us now discuss the upper plot on the right hand side. We are above $T_c$ in the confinement phase and the Polyakov loop sector of the corresponding configurations is still complex. Again we can find that the histogram of the spectral gap is strongly peaked about some value. But now the peak is largely shifted away from zero. We see that the spectral gap is finite for almost all configurations. This clearly indicates that we are in the chirally restored phase. Again, this is as expected, since we are

well above $T_c$. The interesting regime is where $T \sim T_c$. The center plot in the upper row shows the histogram of the spectral gap for that temperature regime with the Polyakov loop in the complex sector. We see that the histogram is double-peaked which means that we have a mixing of the two phases. The peak on the right and left hand side of the histogram correspond to the chirally symmetric phase and chirally restored phase, respectively. In the region near the critical point both phases coexist. This tells us that the chiral phase transition is of first order. For a second order phase transition we have no regime where both phases coexist. In this case we would find that the spectral gap is zero below the critical point of the phase transition and, as the temperature of the system crosses the critical temperature, the spectral gap acquires a finite value instantly, at least in the thermodynamic limit.

Let us now come to the plot in the lower row of Fig. 3.2 which correspond to configurations with real Polyakov loop sector. Because the statistics for the real Polyakov loop sector is always half of the complex one we doubled the bins for the plots with real Polyakov loop sector for $T \sim T_c$ and $T > T_c$. We can see that for the real sector of the Polyakov loop the scenario is similar to the complex Polyakov loop sector. Of course, for $T < T_c$ we find the same peak as for the complex case since below $T_c$ the center symmetry is restored. Above $T_c$ the shift of the peak from zero is larger than in the complex case. Further, the width of the histogram is also larger for the real Polyakov loop sector. The reason for the difference in the two sectors is obvious. As we have seen in Fig. 3.1 the spectral gap for the real sector is simply larger than for the complex sector of the Polyakov loop.

| $\beta_1$ | 8.10, 8.20, 8.25, 8.30, 8.45, 8.60 |
|---|---|
| $L_s \times L_t$ | $16^3 \times 6$, $20^3 \times 6$ |
| # configs. | 800, 400 |

**Table 3.1:** Overview of the different lattices. We have used chirally improved fermions with Lüscher-Weisz gauge action.

Let us summarize. Below the critical point of the confinement phase transition the histogram of the spectral gap is peaked near zero indicating that chiral symmetry is broken. Above $T_c$ the peak is strongly shifted away from zero, which means that we are in the chirally symmetric phase. In between the histogram is double-peaked and both phases coexist indicating a first order phase transition [39]. Our findings are qualitatively the same for both the complex and real sector of the Polyakov loop. Now, that we have seen that the spectral gap is well suited as an order parameter of the chiral phase transition, our next task is to extract the critical temperature from lattice data. It is clear what we have to do: We have to study the averaged spectral gap with respect to the temperature of the system.

## 3.4 The Averaged Spectral Gap I

To analyze the dependence of the averaged spectral gap $\langle g_\lambda \rangle$ we generated lattice QCD data for different temperatures and two lattice sizes. See Table 3.1 for the details. In Fig. 3.3 we plotted the results of our numerical calculations.

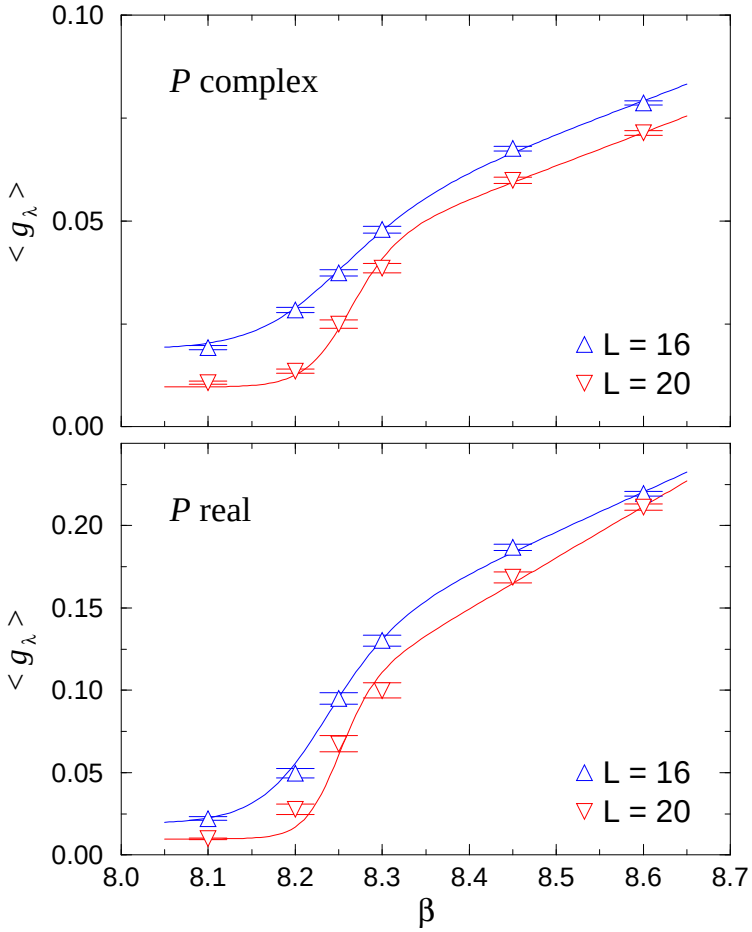


**Figure 3.3:** $\langle g_\lambda \rangle$ vs. $\beta_1$. We plotted the averaged spectral gap for the volumes $V = 16^3 \times 6$ and $V = 20^3 \times 6$. The upper (lower) plot shows the data for the two volumes for the complex (real) Polyakov loop sector. For the low(est) temperatures (below $T_c$) the averaged spectral gap is constant while for high temperatures (above $T_c$) we have a linear behavior. Near $T_c$ the system changes its phase. This causes the averaged spectral gap to change its behavior from constant to linear. The symbols correspond to the data while the curves are fits to the corresponding data.

On the upper plot we see the data for the configurations in the complex Polyakov loop sector while on the lower plot the Polyakov loop sector is real. On both plots we present lattice data for the two different volumes, $V = 16^3 \times 6$ and $V = 20^3 \times 6$. Let us start to discuss the curves for the lowest temperatures, i.e. for $T < T_c$. Note that low temperature means low $\beta$. For the lowest temperature we find that the averaged spectral gap also acquires its lowest value. We note that for the larger volume the

averaged spectral gap is smaller. This is what we expect since we know from the discussion in the last section that the value of the averaged spectral gap below $T_c$ should be of the order of the microscopic gap. Therefore, below $T_c$ the averaged spectral gap should vanish in the thermodynamic limit which is suggested by the data.

At high temperatures, i.e. above $T_c$, we see, that the averaged spectral gap increases. Approximately, the averaged spectral gap shows a linear behavior for both volumes and both sectors of the Polyakov loop. For the smaller volume we find that the averaged spectral gap is always larger in the temperature range we investigated. In the interesting regime where the temperature is near the critical point we see that the averaged spectral gap changes its behavior dramatically. As we reach the critical point from the high temperature regime the linear behavior stops and the averaged spectral gap falls of rapidly to acquire a somehow constant value of the microscopic gap. Again, this behavior is qualitatively the same for all four curves but note that for the larger volume the averaged spectral gap falls of more rapidly than for the smaller volume. The reason for this behavior is easy to understand. For temperatures in the chirally broken phase the averaged spectral gap has a constant behavior. For temperatures in the chirally restored phase we see a linear behavior. On finite lattices there is a smooth crossover of the two phases. In the thermodynamic limit this smooth crossover turns into a discontinuity. At the critical temperature the system "jumps" from the one phase into the other. Below $T_c$ the averaged spectral gap is constant and at $T_c$ it instantly changes its behavior, following the linear behavior of the chirally symmetric phase. However, on the finite lattice we do not have such a sharp transition but it is clear that, as we increase the volume, the smooth change of the averaged spectral gap becomes sharper. This volume dependence is exactly what we observe in our data in Fig. 3.3.

Finally, we have to extract the critical temperature from our data. It is clear that the critical temperature has to be somewhere near to the regime where the averaged spectral gap falls off. A natural approach for extracting the critical temperature would be to take the value of $T$ where the averaged spectral gap becomes steepest and study its behavior in the thermodynamic limit. We will follow a somehow different approach in the next sections.

### 3.4.1 Results for the Polyakov Loop

Before we will determine the critical temperature for the chiral phase transition, we first like to investigate the confinement phase transition and develop a procedure to extract the critical temperature which we will use afterwards to the case of the chiral phase transition. Let us take a look to Fig. 3.4. We plotted the expectation value of the modulus of the Polyakov loop. We know that this quantity is (nearly) zero in the confining phase and finite in the deconfined phase as a look at Fig. 2.2 suggests. From Fig. 3.4 we find that $\langle |P| \rangle$ for high temperatures, i.e. in the deconfinement phase, rises linearly with the temperature. Note that the linear behavior in the high temperature phase does not depend on the volume. In the confinement phase the absolute value of

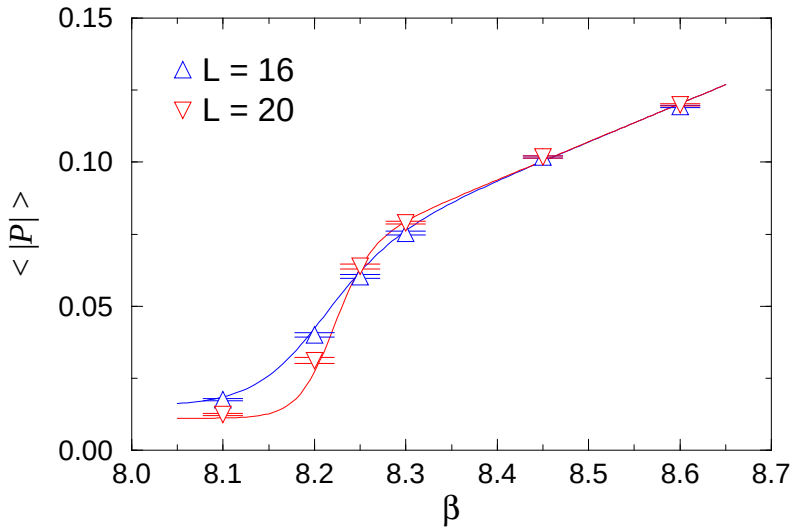


**Figure 3.4:** We plotted the expectation value $\langle|P|\rangle$ of the modulus of the Polyakov loop as a function of $\beta$. The numerical results are shown by the symbols while the full curve is a fit to Formula (3.2). We display results for $16^3 \times 6$ and $20^3 \times 6$ lattices.

the Polyakov loop is expected to be constant and should scale like $L^{-3/2}$ [40], where $L$ is the spatial extent of the lattice. Furthermore, note the similar behavior of $\langle|P|\rangle$ and the averaged spectral gap. Both rise linearly in the high temperature regime and scale with some power of $L$ in the low temperature regime.

Following the ideas of Refs. [41, 42] we now can make the following ansatz for $\langle|P|\rangle$ for a first order phase transition on a finite lattice,

$$\langle|P|\rangle = \frac{cL^{-3/2}\, e^{-\Delta f L^3(\beta-\beta_c)} \;+\; 3[d + k(\beta-\beta_c)]}{e^{-\Delta f L^3(\beta-\beta_c)} \;+\; 3} \;. \tag{3.2}$$

We will fit this formula to the lattice QCD data and extract $\beta_c$, the critical value of $\beta$, from which we can determine the critical temperature. Let us make some comments on this expression. The second term in the numerator of (3.2) reflects the linear behavior of the deconfinement phase. The constants $d$ and $k$ parameterize the high temperature regime. Note that they are not depended on the volume. The factor of the first term in the numerator comes from the constant behavior in the low temperature regime where we know that the modulus of the Polyakov loop behaves like $cL^{-3/2}$. The difference of the free energy of the two phases is denoted by $\Delta f$. Note that we have introduced a factor of 3 which we did because of the 3 different sectors to which the Polyakov loop can belong (although only two of them are physically different). Before we will present numerical data, let us ensure that Eq. (3.2) has the desired asymptotic behavior. In the high temperature regime, where $\beta \to \infty$, the exponentials tend to zero and $\langle|P|\rangle$ shows the linear behavior parameterized by $d$ and $k$. On the other hand, in the low temperature regime ($\beta \to 0$) the exponents of expression (3.2) become positive and in the thermodynamic limit Eq. (3.2) is dominated by the exponentials. Thus we find that the averaged modulus of the Polyakov loop, $\langle|P|\rangle$, behaves like $cL^{-3/2}$ and we

see that $\langle|P|\rangle$ shows the desired asymptotic behavior.

Now, all we have to do is to fit the 5 parameters $c$, $d$, $k$, $\Delta f$, and $\beta_c$ to the lattice data. Note that $\beta_c$ in our ansatz in (3.2) does not depend on the volume because this ansatz was designed for a finite lattice, which means that $\beta_c$ from our ansatz should already be a good estimation of the critical value in the thermodynamic limit. Therefore, we have performed a common fit to both volumes using a Jackknife analysis. The curves in Fig. 3.4 show the fit to the data of the two volumes. We see that our ansatz reproduces the data very well. We obtain a value of $\beta_c = 8.24(1)$ for the critical point of the confinement phase transition with the corresponding statistical error. The small dependence on the volume of $\beta_c$ is the big advantage of our approach. This means, that already for the relatively small lattices we used (compared to the thermodynamic limit) we can achieve a good estimate of the critical value in the thermodynamic limit. Finally, we remark that the critical temperature of the chiral phase transition we obtained is $T = 296(3)$ MeV which could be determined with the help of Ref. [43]. This value (for the Lüscher-Weisz action) is slightly larger than the corresponding value for the Wilson action.

### 3.4.2 Results for the Dirac Eigenvalues

Let us repeat the same analysis for the averaged spectral gap in order to determine the critical point of the chiral phase transition. We know that the averaged spectral gap for high temperature behaves linearly, i.e. we have

$$\langle g_\lambda \rangle \sim k_{r,c}(L_s)(\beta - \beta_c). \tag{3.3}$$

However, there is a difference between $\langle|P|\rangle$ and $\langle g_\lambda\rangle$ in the high temperature regime. While for $\langle|P|\rangle$ we found no dependence of the slope on the (spatial) volume this is not the case for the averaged spectral gap. Therefore, the parameters $d$ and $k$ will depend on the spatial lattice $L_s$ which we denote by $d_{r,c}(L_s)$ and $k_{r,c}(L_s)$, respectively. Furthermore, the averaged spectral gap behaves differently in the two sectors of the Polyakov loop. We account for this by introducing the indices $r$ and $c$.

For the low temperature regime there is a further difference which we have to account for. The volume dependence of the averaged spectral gap appears to be like $L_s^{-3}$ [44]. So for the low temperature regime we make the following ansatz for the averaged spectral gap

$$\langle g_\lambda \rangle \sim c' L_s^{-3}. \tag{3.4}$$

Taking into account Eqs. (3.3) and (3.4) we find that the ansatz for the fitting function of $\langle|P|\rangle$ in (3.2) translates into

$$\langle g_\lambda \rangle_{r,c} = \frac{c' L_s^{-3}\, e^{-\Delta f L_s^3(\beta-\beta_c)} + 3[d_{r,c}(L_s) + k_{r,c}(L_s)(\beta-\beta_c)]}{e^{-\Delta f L_s^3(\beta-\beta_c)} + 3} \tag{3.5}$$

for the averaged spectral gap on a finite lattice. Again, we use a Jackknife analysis to fit the above expression to both volumes of the lattice data. In Fig. 3.3 we show the

fitting results which are represented by the curves. We see that the curves describe the data very well. The values for the critical points of the chiral phase transition for the real and complex sectors of the Polyakov loop obtained from our fits are listed in Table 3.2. We find that the critical values of $\beta$ are approximately the same for the real and complex sector of the Polyakov loop and also coincide with the critical value of the confinement phase transition. This is really an interesting result because in [35] it was claimed that the critical point of the chiral phase transition **should** depend on the sector of the Polyakov loop. Of course, we like to know why we found a different result,

| Measurement | $\langle \lvert P \rvert \rangle$ | $\langle g_\lambda \rangle_{complex}$ | $\langle g_\lambda \rangle_{real}$ |
|---|---|---|---|
| $\beta_c$ | 8.24(1) | 8.29(2) | 8.27(2) |
| $T_c$ [MeV] | 296(3) | 308(5) | 303(5) |

**Table 3.2:** Results for the fits to the lattice data. We listed the critical values of $\beta$ and the corresponding temperatures for the chiral and confinement phase transition.

so let us recapitulate what we have done so far. We determined the critical point of the chiral phase transition for the different sectors of the Polyakov loop. We used the averaged spectral gap as an order parameter of the phase transition. Furthermore, we used chirally improved fermions with the Lüscher-Weisz gauge action, while the authors in Ref. [35] used staggered fermions and their order parameter was the chiral condensate. For the sake of clarity we like to perform the same analysis from above again, but this time we will use staggered fermions with Wilson gauge action. Then we will know if the use of the staggered fermions is responsible for the different results.

## 3.5 The Averaged Spectral Gap II

In this section we will repeat our analysis of the averaged spectral gap of Sec. 3.4.2 but now we will use staggered fermions with Wilson gauge action. As before we start with an analysis of the lowest eigenvalues. We calculated the lowest eigenvalues of the Dirac operator for different values of $\beta$. An overview of the lattices sizes and statistics we used can be found in Table 3.3. In Fig. 3.5 we plotted a histogram of the lowest two eigenvalues, similar to Fig.3.2. We have used the lowest two eigenvalues for staggered fermions because in the continuum the eigenvalues become fourfold degenerate (two positive and two negative eigenvalues reassemble to one fourfold degenerate eigenvalue). Let us start with the high temperature regime, i.e. with $T > T_c$. The lower plot on the right hand side corresponds to an ensemble of gauge field configurations in the high temperature regime with the corresponding Polyakov loop in the real sector. We have used about 500 configurations which means that we have about 1000 eigenvalues of the Dirac operator. We see a similar behavior like in the case of chirally improved fermions. The histogram is peaked at a value which is strongly shifted away from zero. This means that the eigenvalue density near zero must vanish and, therefore, chiral symmetry is restored. This is also true for the complex sector of the Polyakov loop, see the upper plot on the right hand side. Note

the different scale of $\lambda$ for the lower plot. Again, we see that the eigenvalues in the real sector of the Polyakov loop are about three times larger than in the complex sector. Furthermore, note that, in contrast to our results for the chirally improved fermions, there are some eigenvalues near zero which are far away from the peak, see the lower plot on the right hand side. The reason why there are such small

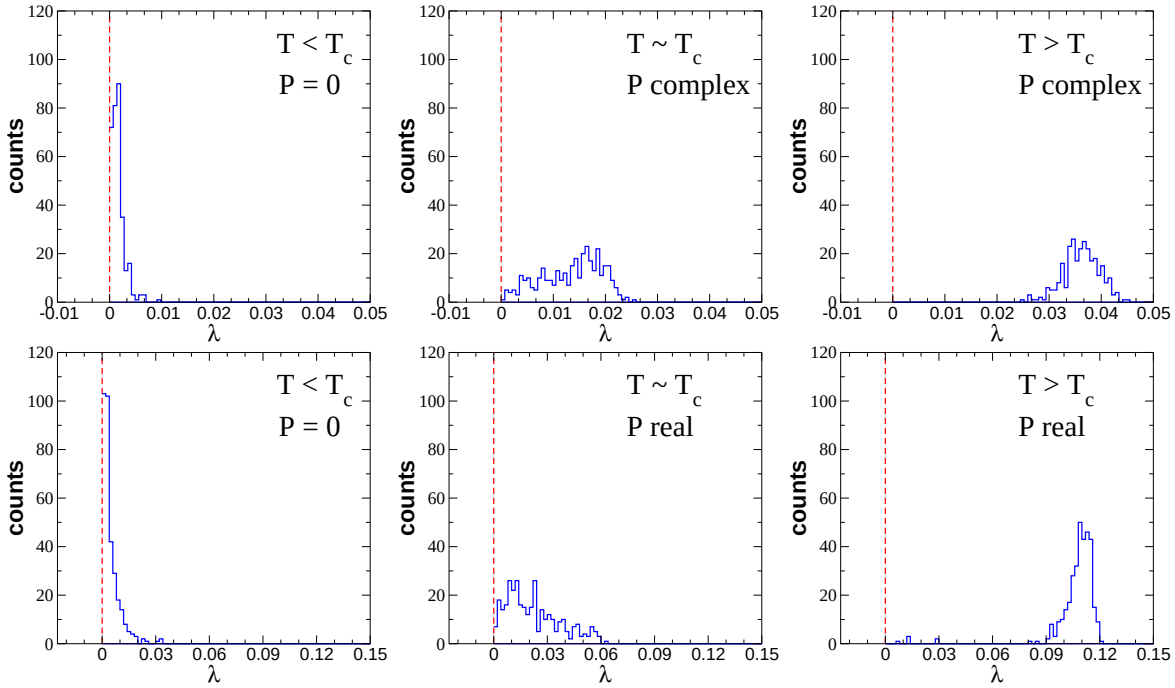


**Figure 3.5:** Histogram of two smallest (nonzero) eigenvalue for staggered fermions. The upper (lower) plots correspond to configurations with complex (real) Polyakov loop, from left to right the temperature $T$ is below, near, and above the critical temperature $T_c$. For all histograms we find a similar behavior as for chirally improved fermions, see Fig. 3.2, although the quasi-zero modes modify the shape of the histograms for intermediate and low temperatures.

eigenvalues in the case of staggered fermions is that staggered fermions have bad chiral properties, i.e. they do not have exact zero modes, just quasi-zero modes. This means that the zero modes are mixing with the eigenvalues of the bulk spectrum. Only in the continuum limit we obtain exact zero modes. Note that in the case of chirally improved fermions we have removed the zero modes from our calculations of the averaged spectral gap. We did so because the zero modes do not contribute in the thermodynamic limit. In the case of staggered fermions we are not able to remove the (quasi) zero modes (at least in a controlled way). We should expect, that this has some impact on the averaged spectral gap and, hence, on the critical point of the chiral phase transition. However, the small eigenvalues in the lower plot on the right hand side correspond to the quasi-zero modes. These quasi-zero modes do not only appear at high temperatures[1] but also in the low temperature regime we find that

[1]Note that in the high temperature regime the quasi-zero modes disappear, because from lattice calculations we know that the instanton density vanishes for large $T$ [32, 33]. Therefore, we find only

they modify the histogram of the lowest eigenvalues. In the lower plot on the left hand side we plotted the histogram of the spectral gap for the real Polyakov loop below $T_c$. Again, for both the real and complex sector, the peak is very close to zero which indicates that chiral symmetry is broken. Compared to the chirally improved fermions of Fig. 3.2 there are much more very small eigenvalues for staggered fermions resulting in a higher value of the histogram near zero. The quasi-zero modes are responsible for this difference.

For temperatures near $T_c$ we find a similar scenario although the two phase signal does not show up as clear as for chirally improved fermions. We suppose that the quasi-zero modes smear the signal. We see that the fact that we cannot remove the quasi-zero modes has impact on the spectral gap. We assume that this remains also true for the averaged spectral gap which we will investigate next.

### 3.5.1 Results for Staggered Fermions

In this section we will calculate the averaged spectral gap for staggered fermions with Wilson gauge action and fit our ansatz in Eq. 3.5 to the numerical data. An overview of the generated lattice QCD data can be found in Table 3.3. In this section we

| $\beta$ | 5.8 - 6.3 (11 values) |
|---|---|
| $L_s \times L_t$ | $16^3 \times 4$, $20^3 \times 6$ |
| # configs. | 500 |

**Table 3.3:** Overview of the different lattices. We have used staggered fermions with Wilson gauge action.

will investigate only the larger lattice with spatial volume $20^3$ and temporal extent $L_t = 6$. In Fig. 3.6 we show the averaged spectral gap and the corresponding fits. On the plot on the left hand side we show the data for the real sector of the Polyakov loop while on the right hand side the data for the complex sector are depicted. For high temperatures, i.e. high values of $\beta$, we find a linear behavior while for low temperatures $\langle g_\lambda \rangle$ is constant. The same was found for chirally improved fermions, so there is no difference here and we can be sure that our approach from above will still apply. However, if we compare the curves for the fits of the averaged spectral gap of the two different types of fermions we can observe that in the case of staggered fermions the averaged spectral gap does not show the usual rapid fall-off near the critical point, see Fig. 3.3 for chirally improved fermions and Fig. 3.6 for staggered fermions. It seems that for staggered fermions the curves near the critical point are flatter, in contrast to the case of chirally improved fermions where near $\beta_c$ the curves change their behavior dramatically. For the complex sector this behavior of the curve is less apparent which means that the linear behavior of the averaged spectral gap stops at a somewhat higher value of $\beta$. This leads us to the conclusion that the critical point of the chiral phase transition appears at a somewhat higher temperature for the complex sector

a few quasi-zero modes in the high temperature regime.

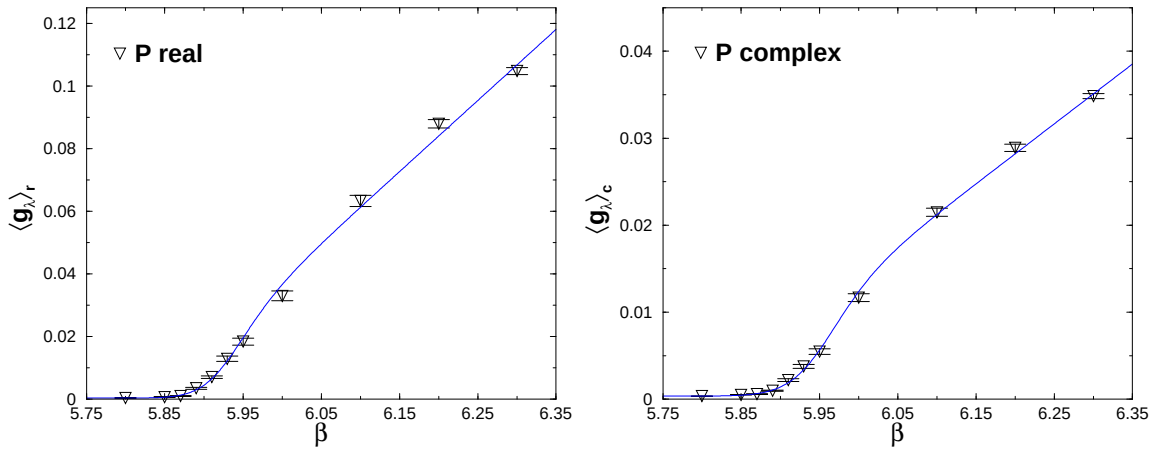


**Figure 3.6:** $\langle g_\lambda \rangle$ vs. $\beta$. We plotted the averaged spectral gap for V=$20^3$x6 for both sectors of the Polyakov loop for staggered fermions. The curves correspond to the fits with the fitting function from ansatz 3.5.

of the Polyakov loop. This is exactly what Christ and Chandrasekharan found in their investigations. Anyway, we can give a more qualitative argument. Let us simply compare the critical values $\beta_c$ for both sectors of the Polyakov loop extracted from our fits. We list them in Table 3.4 and also the value of the critical value $\beta_c^{conf}$ of the confinement phase transition which has been obtained by lattice QCD studies and can be found in Ref. [39]. Indeed we see that the critical value for the complex sector lies above the value for the real sector. This is exactly what we already predicted from our analysis above although we have to emphasize that the difference of the values is small. It is just of a few percentage. The same is true for the difference of the critical values of the chiral phase transition to $\beta_c$ of the confinement phase transition which leads us to the conclusion that the critical point of the chiral phase transition does not depend on the sector of the Polyakov loop and coincide with $\beta_c$ of the confinement phase transition. This is exactly what we found for chirally improved fermions and contradicts the conclusions of Christ and Chandrasekharan.

| Measurement | $\beta_c^{conf}$ | $\langle g_\lambda \rangle_{complex}$ | $\langle g_\lambda \rangle_{real}$ |
|---|---|---|---|
| $\beta_c$ (full) | 5.89 | 5.982 | 5.955 |

**Table 3.4:** Results for the critical values of the chiral and confinement phase transition for staggered fermions with Wilson gauge action.

Thus, even for staggered fermions we cannot verify the claims of Christ and Chandrasekharan. Of course, we like to know how this can come about. Therefore, we will study the influence of the bad chiral properties of the staggered fermions still in more detail in the following.

### 3.5.2 Staggered Fermions and Chiral Symmetry

We know that chiral symmetry on the lattice is always a problem. For Wilson fermions chiral symmetry is explicitly broken and for staggered fermions we just have a kind of residual chiral symmetry. But with these fermions calculations can be performed with relatively low computer power. We can perform calculations with staggered fermions on commonly available home computers. Ginsparg-Wilson fermions, for which we can define a lattice version of chiral symmetry, are much more expensive. Thus, many calculations are still made with staggered or Wilson fermions despite their bad chiral properties. In the following we will investigate the chiral properties of the low-lying eigenvalues of the Dirac operator for staggered fermions. This will help us to get a better understanding of the numerical results obtained in Chapters 3 and 4.

Chiral symmetry is intimately related to the zero modes of the Dirac operator. This can be easily seen by the following argument. The (massless) Dirac operator $\not{D}$ obeys the following equation

$$\not{D}^\dagger = \gamma_5 \not{D} \gamma_5. \tag{3.6}$$

This equation holds also on the lattice. If $\not{D}$ has no degeneracies, an eigenvector $\psi$ of the Dirac operator with eigenvalue $\lambda$ satisfy the equation $\psi^\dagger \gamma_5 \psi \neq 0$ if and only if $\lambda$ is real. Furthermore, in the continuum the Dirac operator is anti–hermitian and therefore the eigenvalues lie on the imaginary axis. Thus, the only real eigenvalue of $\not{D}$ is zero. Note that chirality provides an additional distinction between zero modes and nonzero modes. While the zero modes have chirality of $\psi^\dagger \gamma_5 \psi = \pm 1$ the nonzero modes have zero chirality. Because the eigenvalues and their corresponding chirality depend continuously on the gauge field the zero modes cannot be shifted away from zero by a continuous deformation of the gauge field.

This argument does not work on the lattice in general, since the Dirac operator is not necessarily anti-hermitian. This means that the eigenvalues do not have to be imaginary anymore, but can be distributed arbitrarily in the complex plane. Therefore, the chiral modes (modes with $\langle \gamma_5 \rangle = \psi^\dagger \gamma_5 \psi \neq 0$) will no longer lie at zero only, but are distributed on the real axis. However, we can make a continuous transformation on the gauge fields such that zero modes are shifted away from zero along the real axis. Since also the chirality depends continuously on the gauge field, the chirality of the zero mode can vary. Note that there is no smooth transformation on the gauge field such that we can shift away an eigenvalue from the real axis, because then the chirality would jump from a finite value to zero. We see that in this sense there are no exact zero modes on the lattice in general (as long as we do not adjust the gauge field appropriately). The modes on the real axis correspond to the zero modes in the continuum.

The connection to chiral symmetry can now be seen as follows. If chiral symmetry is explicitly manifest then the Dirac operator anti–commutes with $\gamma_5$, $\{\not{D}, \gamma_5\} = 0$. Together with Eq. (3.6) it would follow that $\not{D}$ is anti–hermitian. As we know chiral symmetry has to be explicitly broken on the lattice to avoid fermion doubling. Therefore, we do not have exact zero modes with definite chirality on the lattice. Let us note that Ginsparg-Wilson fermions break chiral symmetry in the mildest possible

way. For those fermions we can define a lattice version of chiral symmetry which becomes the continuum chiral symmetry as the lattice spacing goes to zero. The chiral properties for these fermions are best on the lattice which is the reason why they are subject of intense investigations.

In this work we have used staggered fermions in most calculations. In order to get detailed information about the chiral properties of staggered fermions we like to derive an expression which corresponds to chirality in the continuum limit and depends on the staggered fields $\bar{\chi}$ and $\chi$. This is useful because the eigenmodes we obtain in our numerical calculations are expressed in terms of these fields. We start with the flavor fields $\bar{q}$ and $q$ of the staggered fermions defined in (2.40). Note that these fields correspond to four quark flavors in the continuum limit. We will calculate the chirality $\langle \bar{q}\gamma_5 F_\rho q\rangle$ where $F_\rho$ is some flavor matrix of the form $F_\rho^T \equiv \Gamma_\rho$ and $\Gamma_\rho$ is defined by

$$\Gamma_\rho \equiv (\gamma_1)^{\rho_1}(\gamma_2)^{\rho_2}(\gamma_3)^{\rho_3}(\gamma_4)^{\rho_4}, \tag{3.7}$$

see Eq. 2.41. Remember, the components $\rho_i$ of $\rho \equiv (\rho_1, \rho_2, \rho_3, \rho_4)$ can be either 1 or 0. In particular we are interested in $\Gamma_\rho = \mathbb{1}$ because the staggered action in (2.47) is diagonal in flavor space in the continuum limit. But also other flavor structures might be of interest because in the staggered action on a finite lattice there is also a flavor matrix in the second term, so we will perform our derivation for general flavor structures in the following.

$$\begin{aligned}
\langle \bar{q}\gamma_5 F_\rho q\rangle &= 16 \sum_{\substack{y;\alpha\alpha' \\ aa'}} \bar{q}_y^{a\alpha}\gamma_5^{\alpha\alpha'} F_\rho^{aa'} q_y^{\alpha' a'} \\
&= \frac{1}{4} \sum_{\substack{y;\eta\eta' \\ \alpha\alpha';aa'}} \bar{\chi}_{2y+\eta}\, \chi_{2y+\eta'}\, \Gamma_\eta^{\dagger\, a\alpha}\gamma_5^{\alpha\alpha'} F_\rho^{aa'} \Gamma_{\eta'}^{\alpha' a'} \\
&= \frac{1}{4} \sum_{y;\eta\eta'} \bar{\chi}_{2y+\eta}\, \chi_{2y+\eta'}\, \mathrm{Tr}\left(\Gamma_\eta^\dagger \gamma_5 \Gamma_{\eta'} F_\rho^T\right).
\end{aligned} \tag{3.8}$$

Evaluating the trace we arrive at the following structure

$$\begin{aligned}
\langle \bar{q}\gamma_5 F_\rho q\rangle &= \sum_{y;\eta} \bar{\chi}_{2y+\eta+\rho}\, \chi_{2y+\eta}\, z_{2y+\eta;\rho} \\
&= \sum_x \bar{\chi}_{x+\bar{\rho}}\, \chi_x\, z_{x\rho},
\end{aligned} \tag{3.9}$$

where $\bar{\rho}$ is defined by exchanging all components of $\rho$ which are equal to 1 by 0 and vice versa. The phase $z_{x\rho}$ is given by

$$\begin{aligned}
z_{x\rho} &= (-1)^{x_1+x_3+\rho_1+\rho_3+\sum_{\nu<\mu}\rho_\nu x_\mu} \\
&= (-1)^{\rho_1+\rho_3+x_1+x_2\rho_1+x_3(1+\rho_1+\rho_2)+x_4(\rho_1+\rho_2+\rho_3)}.
\end{aligned} \tag{3.10}$$

Now we can easily evaluate the chirality for different flavor structures. Some examples for $F_\rho$ with the corresponding phase of $z_{x\rho}$ are listed in Table 3.5. Let us investigate

| $\rho$ | $F_\rho^T$ | | $z_{x\rho}$ | |
|---|---|---|---|---|
| $(0,0,0,0)$ | $\Gamma_0$ | $= \mathbb{1}$ | $z_{x;0}$ | $= (-1)^{x_1+x_3}$ |
| $(1,1,0,0)$ | $\Gamma_{12} = \gamma_1\gamma_2$ | $= \mathrm{i}\begin{pmatrix}\sigma_3 & 0\\ 0 & \sigma_3\end{pmatrix}$ | $z_{x;12}$ | $= (-1)^{1+x_1+x_2+x_3}$ |
| $(0,0,1,1)$ | $\Gamma_{34} = \gamma_3\gamma_4$ | $= \mathrm{i}\begin{pmatrix}\sigma_3 & 0\\ 0 & -\sigma_3\end{pmatrix}$ | $z_{x;34}$ | $= (-1)^{1+x_1+x_3+x_4}$ |
| $(1,1,1,1)$ | $\Gamma_{1234} = \gamma_1\gamma_2\gamma_3\gamma_4$ | $= \mathrm{i}\begin{pmatrix}-1 & 0\\ 0 & 1\end{pmatrix}$ | $z_{x;1234}$ | $= (-1)^{x_1+x_2+x_3+x_4}$ |

with $\gamma_j = \mathrm{i}\begin{pmatrix}0 & \sigma_j\\ -\sigma_j & 0\end{pmatrix}$ $(j=1,2,3)$ and $\gamma_4 = \mathrm{i}\begin{pmatrix}0 & 1\\ 1 & 0\end{pmatrix}$

**Table 3.5:** Examples for the phase $z_{x\rho}$ for different flavor structures $F_\rho^T$. The most interesting case is $F_\rho = \mathbb{1}$.

expression (3.9) in more detail for the most interesting case of $F_\rho = \mathbb{1}$. This means we have $\rho = (0,0,0,0)$ and $\bar{\rho} = (1,1,1,1)$. We obtain from Eq. 3.9

$$\langle \bar{q}\gamma_5 q\rangle = \sum_x (-1)^{x_1+x_3}\ \bar{\chi}_{\left(x+\sum_{i=1}^4 \hat{x}_i\right)}\chi_x, \tag{3.11}$$

where we sum over all lattice sites and $(x+\hat{x}_i)$ denotes the next lattice site in $i$-direction. Note that $\left(x+\sum_{i=1}^4 \hat{x}_i\right)$ is a lattice site which sits on one diagonal of the hypercube around $x$.

We see that $\langle \bar{q}\gamma_5 q\rangle$ is a non-local object which is not gauge-invariant. To maintain gauge invariance we have to add gauge links between $\bar{\chi}_{\left(x+\sum_{i=1}^4 \hat{x}_i\right)}$ and $\chi_x$ along the shortest connection between the two lattice sites (Note, that there are 4! possibilities for the shortest path.). To maintain invariance of lattice transformations we have to average over all $2^4$ hyper-diagonals. So, finally, we obtain the following gauge-invariant expression for the chirality of staggered fermions

$$\langle \gamma_5\rangle \equiv \langle \bar{q}\gamma_5 q\rangle = \frac{1}{2^4 4!}\sum_{\substack{x\mu\\ \mu_i\neq\mu_j}} (-1)^{x_1+x_3}\ \bar{\chi}_{\left(x+\sum_{i=1}^4 \hat{\mu}_i\right)} \prod_{j=1}^{4} U^\dagger_{\left(x+\sum_{i=1}^{j-1}\hat{\mu}_i\right)\mu_j}\chi_x, \tag{3.12}$$

where $U^\dagger_{x\mu_j}$ denotes the link variable on the link based at $x$ in direction $\mu_j$ and $\mu_j$ can take the values $\pm1, \pm2, \pm3, \pm4$ with $j = 1,2,3,4$. The next lattice site from $x$ in $\mu_j$-direction is denoted by $(x+\hat{\mu}_j)$. The summation in (3.12) is over all lattice sites $x$ and all possible shortest paths reaching the hyper-diagonal site $\left(x+\sum_{i=1}^4 \hat{\mu}_i\right)$.

Now, we can apply this formula to numerical data. In Fig. 3.7 we give some examples of the chirality of the lowest 10 eigenvalues for different ensembles. The column on the left hand shows data for the real sector of the Polyakov loop, the

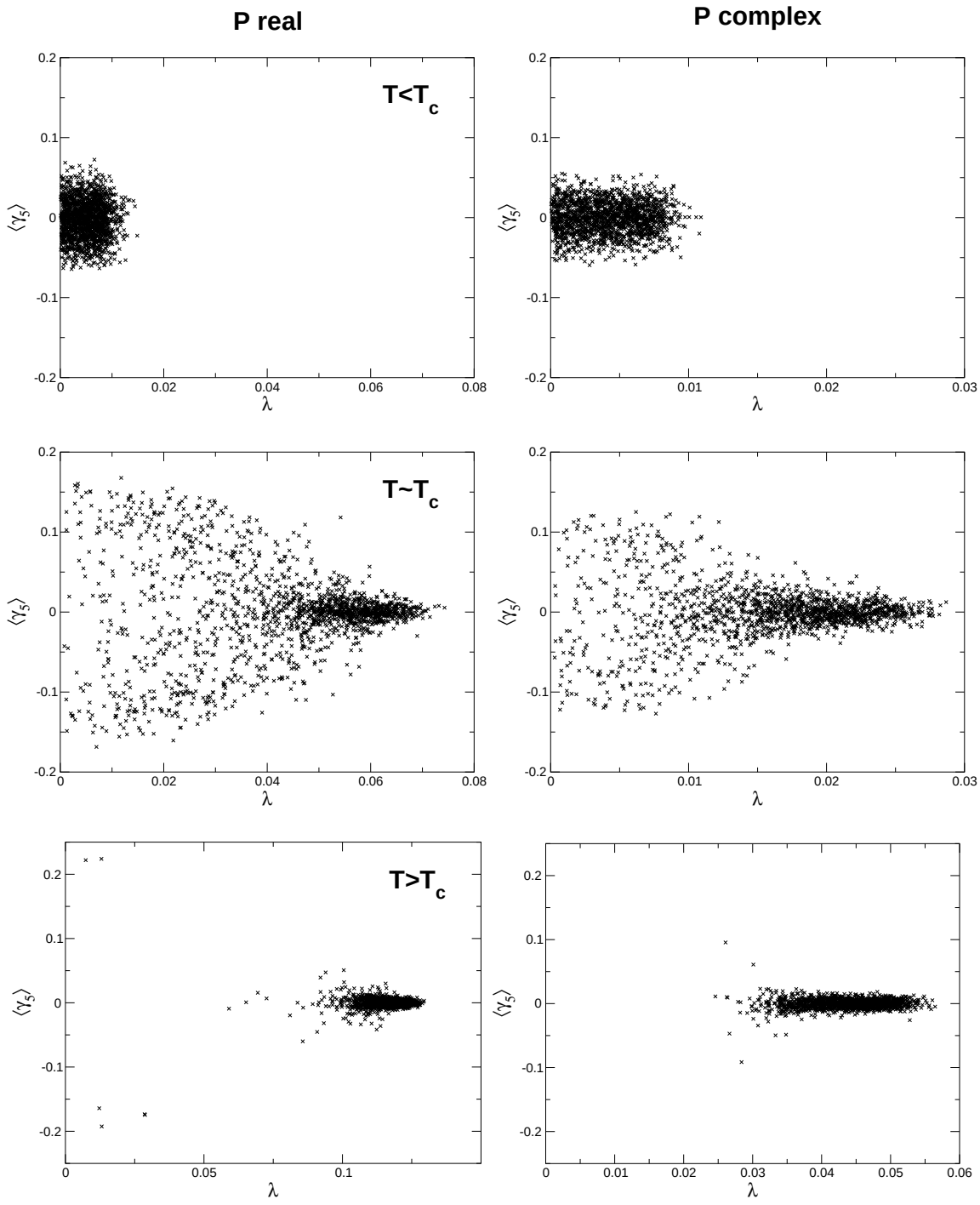


**Figure 3.7:** Chirality $\langle\gamma_5\rangle$ vs. Dirac eigenvalue $\lambda$. We plotted the chirality for the 10 lowest eigenvalues for three different ensembles with $T < T_c$, $T \sim T_c$, and $T > T_c$ (from top to bottom). The column on the left (right) hand side shows data for the real (complex) Polyakov loop sector.

column on the right hand side corresponds to the complex sector, see Sec. 2.3 for details on the Polyakov loop. The plots show the chirality of eigenmodes of about 500 configurations with Wilson gauge action which means that we see about 5000 data points. The lattice volume is $20^3 \times 6$. The ensembles in the first row have temperature $T$ below the critical temperature $T_c$ of the confinement phase transition. We find that the chirality is homogeneously distributed along the lowest eigenvalues we plotted. The maximum value of the chirality is about 0.05 which is far away from one but, compared to the data in the plots in the last row, also far away from zero. Therefore, we conclude that for this temperature regime the (quasi-)zero modes[2] strongly mix with the nonzero modes. We see, that although the lattice spacing is relatively small (compared to lattices used in common calculations) we do not have good chiral properties. Note that qualitatively there is no difference between the real and complex sector of the Polyakov loop.

In the second row of Fig. 3.7 the temperature is close to $\beta_c$. We see that the maximum value of the chirality is now larger and close to 0.2. There are two regions, the region below $\lambda \approx 0.015$ (for the complex sector of the Polyakov loop and 0.045 for the real sector) where the chirality acquires large values, and the region above 0.015 (0.045) where the chirality only fluctuates around zero. We conclude that the quasi-zero modes mix less with the bulk modes [45]. Therefore, the chirality of the quasi-zero modes is enlarged and these eigenmodes are supposed to become exact zero modes in the continuum limit.

For even higher temperatures, i.e. $T > T_c$, we observe that eigenmodes with large or medium large chirality have almost disappeared. We mostly can find only nonzero modes which have chirality near zero. This can be explained by the instanton picture. Every isolated instanton possesses an exact zero modes (in the continuum). In the high temperature phase instantons and anti–instantons are strongly mixing and the probability to find isolated instantons vanishes. Hence, we should find fewer zero modes which agrees with our observations. Note that also the density of the eigenvalues near $\lambda = 0$ vanishes implying that chiral symmetry is restored, see Sec. 2.4.

### 3.5.3 The Influence of the Quasi-Zero Modes

In Sec. 3.5.1 we found that the critical point of the chiral phase transition does also not depend on the $Z_3$ sectors of the Polyakov loop for staggered fermions but we have seen that the critical temperature $T_c^{complex}$ for the complex sector is somewhat larger than $T_c^{real}$ and both temperatures are also larger than $T_c$ of the confinement phase transition. In this section we will study the influence of the bad chiral behavior of the staggered fermions on these findings.

As already mentioned, staggered fermions do not have exact zero modes so we can not remove them from our calculation of the spectral gap and, hence, of the critical temperature. We conjectured that this may have some impact on the results. In

[2]We denote the eigenmodes which are supposed to become zero modes in the continuum limit also as quasi-zero modes. Note that the properties of these modes are due to lattice artifacts and they are of different origin than the modes which are responsible for the chiral phase transition.

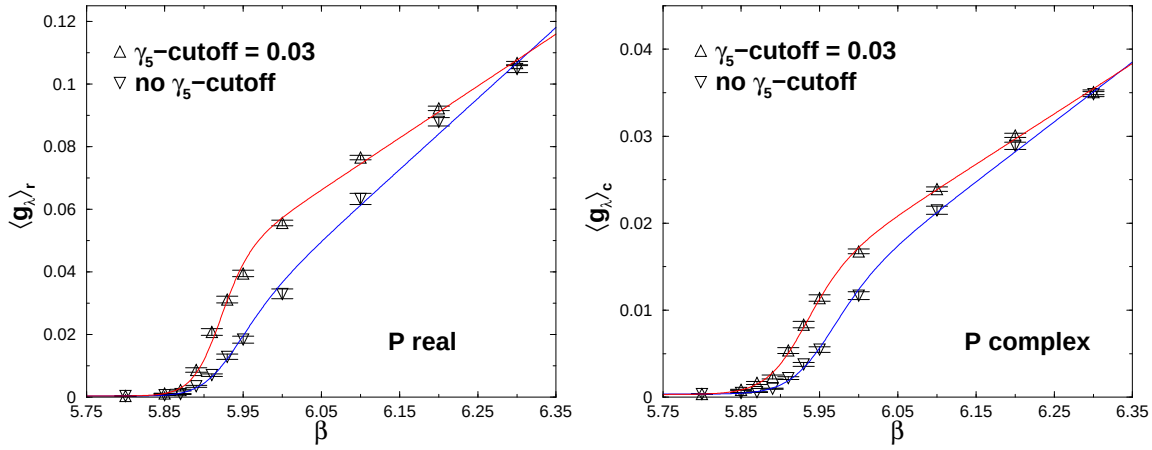


**Figure 3.8:** $\langle g_\lambda \rangle$ vs. $\beta$. The blue fit curves and corresponding data are the same as in Fig. 3.6, the red curves with corresponding data represent the modified data with chirality cut off. The averaged spectral gap is enhanced for both the real (plot on the left hand side) and complex (plot on the right hand side) sector of the Polyakov loop.

the following we will give some evidence that indeed the quasi-zero modes play an important role.

In the center row of Fig. 3.7 we plotted the chirality for staggered fermions for $T \sim T_c$. In Sec. 3.5.2 we concluded that the modes with high chirality, which we nicely see in this plot, correspond to exact zero modes in the continuum limit. These quasi-zero modes do not contribute to the spectral gap in the continuum limit but for finite $a$ they may have some impact on the results. To study the impact of these modes for finite $a$ we should get rid of them somehow. This can be done by identifying all modes which have chirality larger than some value as quasi-zero modes and do not take them into account for the calculations. We do not expect of course that

| Measurement | $\beta_c^{conf}$ | $\langle g_\lambda \rangle_{complex}$ | $\langle g_\lambda \rangle_{real}$ |
|---|---|---|---|
| $\beta_c$ ($\gamma_5$-cutoff) | 5.89 | 5.952 | 5.938 |
| $\beta_c$ (full) | 5.89 | 5.982 | 5.955 |

**Table 3.6:** Results for the critical values of $\beta$ for the fits of the original and modified data. The values with the chirality cut off lie closer to $\beta_c^{conf}$ of the confinement phase transition.

this procedure removes the influence of the quasi-zero modes completely because the quasi-zero modes are mixing with the non zero modes. But we should expect that our results should improve. Note that for $T < T_c$ the mixing of the zero modes is stronger and, therefore, the removal of the quasi-zero modes may not result in a dramatic improvement. But for $T \sim T_c$ and $T > T_c$ the mixing of the quasi-zero modes is weaker and we expect our approach to work. As most of our data is for the intermediate and high temperature regime, there should not be any serious problem.

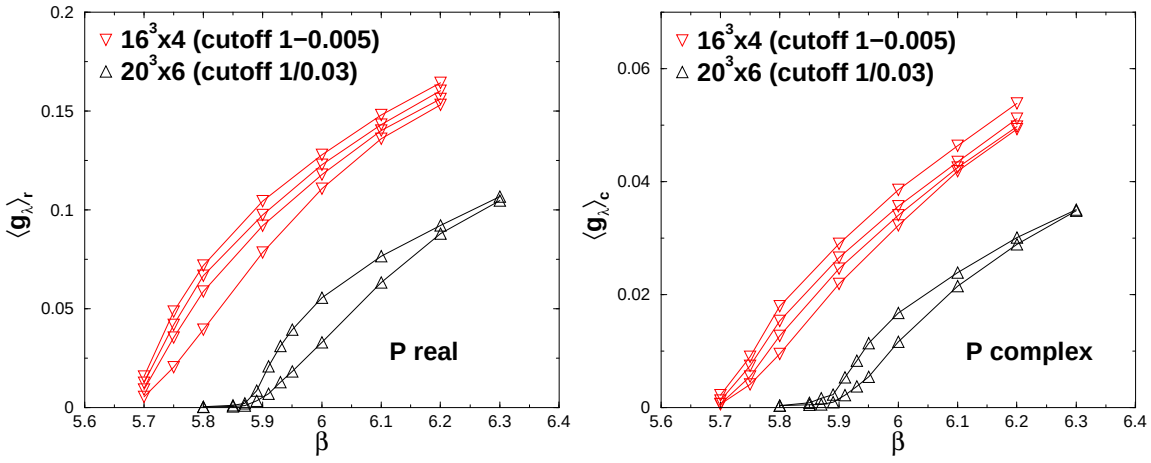


**Figure 3.9:** We plotted the averaged spectral gap $\langle g_\lambda \rangle$ for two volumes $V = 20^3 \times 6$, $V = 16^3 \times 4$ and different cut-off values for the chirality (1 and 0.03 for $V = 20^3 \times 6$, and 1, 0.02, 0.01, and 0.005 for $V = 16^3 \times 4$). The upper triangles correspond to the data which we have shown already in Fig. 3.8. We observe that the averaged spectral gap is more enhanced for smaller cut-off.

What we now have to do is to find a suitable cut-off value for the chirality above which we will ignore the quasi-zero modes. By looking at Fig. 3.7 we can deduce it. In the last row we have $T > T_c$ and we have nearly no quasi-zero modes. The maximum value of the chirality in the bulk spectrum is about 0.03. So we expect all eigenmodes with chirality lower than this value to be nonzero modes in the continuum limit. We conclude that this is a natural value for cutting off the quasi-zero modes.

Let us now present some numerical data. In Fig. 3.8 the upper triangles correspond to the same data as in Fig. 3.6. The lower triangles correspond to the modified data where we simply ignored all eigenvalues with chirality larger than 0.03. This means that for the calculation of the spectral gap we did not use the lowest (first) eigenvalue but we used the first eigenvalue which has chirality below 0.03. This may be the second, third, etc. eigenvalue or the first one. The first observation we make is that the averaged spectral gap for the modified data is enhanced. This is not surprising because we have seen in Fig. 3.7 that the lowest eigenvalues also have the largest chirality. Further we see that the curves now look much more like the averaged spectral gap for chirally improved fermions, see Fig. 3.3. The flat behavior of the curves of the raw data has now vanished and near the critical point the curves are much steeper. Let us see how this affects the fitted values. In Table 3.6 we listed the critical values of $\beta$ for both the raw and modified data. We see that the critical values are closer to the critical value of the confinement phase transition and, thus, the situation has indeed improved. We have shown that the influence of the quasi-zero modes and, therefore, the bad chiral behavior of staggered fermions indeed have some (negative) impact on the critical temperatures of the chiral phase transition in both sectors of the Polyakov loop.

Before we are going to conclude this chapter we still want to present another inves-

tigation which is connected to the different findings of Christ and Chandrasekharan. Christ and Chandrasekharan used lattices with temporal extent of 4 while we used for our analysis with chirally improved fermions and staggered fermions lattices with temporal extent 6. To be sure that this difference is not responsible for the different findings we will apply our approach to staggered fermions on a lattice with $L_t = 4$ and $L_s = 16$. In Fig. 3.9 we plotted both volumes $V = 20^3 \times 6$ and $V = 16^3 \times 4$ with different cut-off values for the chirality. In Table 3.7 we listed the corresponding values of the fits. First note that the three values of $\beta_c$ for the two phase transitions coincide within a few percent. So we find no different behavior for the data with $L_t = 4$. Secondly, we see that for very small cut-off values $\beta_c$ is increasing again. This is because we have started to remove modes which are no quasi-zero modes. This of course has some uncontrolled impact on our calculations. Therefore, a cut-off value of about 0.01 seems to be reasonable.

| Measurement | $\gamma_5$-cutoff | $\beta_c^{conf}$ | $\langle g_\lambda \rangle_{complex}$ | $\langle g_\lambda \rangle_{real}$ |
|---|---|---|---|---|
| $\beta_c$ | 1 (full) | 5.69 | 5.78(5) | 5.82(5) |
| | 0.1 | 5.69 | 5.78(5) | 5.82(5) |
| | 0.05 | 5.69 | 5.77(3) | 5.82(4) |
| | 0.03 | 5.69 | 5.76(2) | 5.81(4) |
| | 0.01 | 5.69 | 5.76(2) | 5.79(4) |
| | 0.005 | 5.69 | 5.76(2) | 5.79(4) |
| | 0.001 | 5.69 | 5.77(3) | 5.81(6) |

**Table 3.7:** Results for the critical values $\beta_c$ of the chiral phase transition for $V = 16^3 \times 4$. The value for $\beta_c^{conf}$ of the confinement phase transition is taken from [39].

Let us conclude this chapter. We started with the question whether the critical point of the chiral phase transition depends on the two different sectors of the Polyakov loop. If so, this would be very important for the understanding of confinement and chiral symmetry breaking. Such a result may be a link to the unsolved problem of how the chiral and confinement phase transition are connected. Christ and Chandrasekharan claimed that they found a dependence of the critical temperature on the sectors. In their studies they investigated the chiral condensate with staggered fermions and Wilson action on lattices with $L_t = 4$. Motivated by this puzzle we reinvestigated this problem again but now with chirally improved fermions with Lüscher-Weisz gauge action and a different order parameter for the chiral phase transition, namely the averaged spectral gap. We observed, in contrast to Christ and Chandrasekharan, that the critical points of the real and complex sector of the Polyakov loop coincide. In order to see whether our findings depend on the different choice of the fermions, we investigated the problem with staggered fermions and Wilson action. However, the results for our approach with staggered fermions agree with those we obtained from chirally improved fermions. Furthermore, we could not observe a dependence of our results for staggered fermions for a different extent in the temporal direction. We studied $L_t = 6$ and $L_t = 4$. We could show that the

bad chiral behavior of the staggered fermions has some impact on the results and could have affected the analysis of [35]. So we could indeed find that by reducing the quasi-zero modes and improving the chiral properties the critical points for the chiral phase transition $\beta_c^{real}$ and $\beta_c^{complex}$ are closer to the critical $\beta$ of the confinement phase transition, and, further, that $\beta_c^{complex}$ is approaching $\beta_c^{real}$. Altogether, we did not find any dependence of the critical point on the Polyakov loop sector. However, this does not have to be the case for other order parameters like e.g. the chiral condensate. So our explanation for the different findings compared to the results of Christ and Chandrasekharan is that the bad chiral behavior of the staggered fermions simply leads to larger artifacts in the case of the chiral condensate.

# Chapter 4

# Searching Calorons on the Lattice

In Chapter 3 we concentrated on the connection between the chiral and confinement phase transition. Whereas the mechanism of the confinement phase transition is still not well understood, we have a well established picture of the chiral phase transition, namely the instanton picture we introduced in Sec. 2.5. In this picture the vacuum consists of weakly interacting instantons and anti–instantons in the chirally broken phase, which become strongly interacting in the chirally symmetric phase forming so-called instanton-anti–instanton (IA) molecules. The crucial property of the instanton is the fermionic zero mode. In the liquid phase, where instantons are weakly interacting and the density of the instantons is constant with respect to the temperature, the zero modes of the instantons are perturbed weakly which means that they are slightly shifted away from zero. The density of eigenvalues near zero is therefore finite and chiral symmetry is broken. In the high temperature phase IA molecules are formed and the zero modes mix strongly, i.e. chiral symmetry is restored.

This picture qualitatively describes the mechanism of chiral symmetry breaking. Of course, we like to validate this picture. Beside analytical analysis the lattice description of QCD offers an ideal approach probing the vacuum for instantons because instantons are non-perturbative objects. Unfortunately, it turns out that the basic methods investigating the topological properties of lattice QCD are less helpful. For example, if we are calculating a naive lattice version of the topological charge of (2.111) on the lattice we observe that we do not obtain an integer number as we do in the continuum. The reason for this is that the gauge field configurations on the lattice show strong fluctuations compared to the lattice spacing which means that we have large lattice artifacts for observables which are sensitive on small distances (compared to the lattice spacing). One possibility to improve the situation is cooling. If we cool down a gauge configuration we reduce the fluctuations and the gauge field approaches its classical solution. So, reducing the ultraviolet fluctuations, in principle, would allow us to obtain reasonable values for the topological charge, but there is the problem that objects on the lattice are not topologically save. This means that during the cooling procedure instantons can "fall through" the lattice or, the other way round, new instantons can be created. In the continuum the global topological properties of gauge field configurations are protected in the sense that continuous transformations of the gauge field cannot change the topological properties. This is no longer true

on the lattice since there are no continuous transformations anymore. Now it is also clear, why strong ultraviolet fluctuations are problematic for the calculation of the topological charge. For strong ultraviolet fluctuations on the lattice we cannot say for sure whether a small instanton is an instanton or not. So, in order to obtain reasonable results for the topological charge subtle methods are used.

Another way to access the topological properties of the gauge field on the lattice is to look at fermionic properties. This approach measures the topological content of a gauge field indirectly. For example, we can measure the topological charge $Q$ via the index theorem (or Atiyah-Singer theorem) [46]

$$Q = n_+ - n_-, \tag{4.1}$$

where $n_+$ and $n_-$ denotes the number of left- and right-handed zero modes, respectively. It can be shown that the theorem also holds for fermions on the lattice which obey the Ginsparg-Wilson equation exactly [47, 48, 49]. Also with fermions which do not exactly fulfill the Ginsparg-Wilson relation (like chirally improved fermions) the index theorem can be applied because left-handed and right-handed zero modes can be identified very well, see Ref. [12] for details. Another way to search for instantons on the lattice is to look at their localization properties. As we have mentioned already in Sec. 2.5, we expect that the Dirac eigenmodes in the liquid phase, i.e. in the chirally broken phase, become collective and therefore are delocalized. On the other hand, in the gas phase, where IA molecules dominate the vacuum, the quarks are bound to the IA molecules and the Dirac eigenmodes are localized. We see that the localization properties of the Dirac eigenmodes allow us to validate the instanton picture of chiral symmetry breaking. Of course, only observing the expected localization properties on the lattice does mean that we have shown the correctness of the instanton picture. But it can provide a piece of evidence which should fit into the whole, or, say it the other way round, if we do not observe the localization properties of the fermions, which we expect for chiral symmetry breaking, then the instanton picture is not correct and we have to think of an other mechanism for chiral symmetry breaking.

In Refs. [51, 52] it was found that the lowest eigenmodes indeed show the correct localization properties for zero temperature. Being investigated for the first time we like to analyze the localization properties of the lowest Dirac eigenmodes for finite temperature. We therefore will discuss the concept of instantons at finite temperature in Sec. 4.1. Before we will present numerical results in Sec. 4.3 we define a quantity which allows us to measure the localization of an eigenmode of the Dirac operator, see Sec. 4.2.

## 4.1 Calorons

In Sec. 2.5 we have presented an instanton solution for $T = 0$, see Eq. (2.120). An instanton solution for finite temperature can also be constructed. This solution is usually called caloron (for a review see Ref. [53]). From Sec. 2.2 we know how to study QCD at finite temperature. In the temporal direction we have to impose periodic

boundary conditions for the gauge fields and anti-periodic boundary conditions for the fermion fields. Further, we have to remember that the (finite) temporal lattice extent corresponds to the temperature. For the caloron solution this simply means that instantons are periodically repeated in time direction. In other words, we have to line up the zero-temperature instantons in time direction. We can construct such solutions using the multi-instanton approach first derived by 't Hooft [54]. An explicit expression for the gauge field was given first by Harrington and Shepard [55],

$$A^a_\mu = \bar{\eta}^a_{\mu\nu} \Pi(x)\, \partial_\nu \Pi^{-1}(x), \tag{4.2}$$

where

$$\Pi(x) = 1 + \frac{\pi\rho^2}{\beta r} \frac{\sinh(2\pi r/\beta)}{\cosh(2\pi r/\beta) - \cos(2\pi r/\beta)}\,. \tag{4.3}$$

The topological charge of the instanton is one, $Q = 1$, and the action is $S = 8\pi^2/g^2$. Note that the action does not depend on the temperature. We can also construct calorons with $Q = -1$ by simply replacing $\bar{\eta}^a_{\mu\nu} \to \eta^a_{\mu\nu}$.

Let us discuss the caloron in more detail. For low temperatures, i.e. $T\rho \ll 1$, we easily find that the caloron solution looks like an isolated instanton. For high temperature, i.e. $T\rho \gg 1$, the situation changes [53]. In the far region, where $r > \mathcal{O}(\rho^2/\beta)$, the caloron looks like a three-dimensional dipole field, $E^a_i = B^a_i \sim \mathcal{O}(1/r^3)$, whereas in the intermediate region, $\mathcal{O}(\beta) r < \mathcal{O}(\rho^2/\beta)$, the caloron resembles a (temperature independent) dyon with unit magnetic and electric charges,

$$E^a_i = B^a_i = \frac{\hat{r}^a \hat{r}^i}{r^2}. \tag{4.4}$$

Note that the caloron also possesses a fermionic zero mode [56, 57]. An explicit expression for the zero mode can be found in Ref. [27]. It is clear that the instanton picture of chiral symmetry breaking qualitatively is still true for calorons. So we expect that there is also a liquid phase for low temperatures and a gas phase for high temperatures. However, there are some differences to the zero temperature phase. For example, for higher temperatures (compared to $T_c$) the fermionic zero mode becomes more delocalized in time, though it remains localized in space. Furthermore, we still have to embed these SU(2) solutions into SU(3). The naive embedding leads to solutions which correspond to the real sector of the Polyakov loop, i.e. $\theta_P = 0$. In Refs. [58, 59] it is described how to obtain embedded solutions for SU(3). It turns out that the embedded zero mode of the caloron strongly depends on the Polyakov loop sector. It falls off asymptotically like

$$|\psi|^2 \sim \exp[-2(\pi - |\theta_P|) r T]/r^2, \tag{4.5}$$

where $r$ denotes the three-dimensional distance from the caloron axis. Note that for a single instanton $|\psi|^2$ falls off like a power of $r$. From (4.5) it follows that for the complex sectors of the Polyakov loop the radius of the modes is about 3 times larger, which means that they occupy a larger volume. We see that the localization properties

of the zero modes show strong differences in the two different Polyakov loop sectors. This observation can act as a signature for calorons, which means if there are calorons on the lattice we should observe the different localization properties in the different sectors. In Sec. 4.3 we will search for such a signature on the lattice. But before we will introduce an quantity which allows us to measure the localization of a mode.

## 4.2 The Inverse Participation Ratio

In order to decide whether an eigenmode of the Dirac operator is localized or not we have to study the density $\psi^\dagger(x)\psi(x)$ where $\psi(x)$ is an eigenvector of the Dirac operator $\not{D}$, $\not{D}\psi = \pm i\lambda\psi$. Of course, it is much more comfortable to have a quantity which measures the localization of the eigenmode instead of looking at every single configuration. We introduce the inverse participation ratio (IPR) which is usually defined by

$$I_{cont} = V_0 \int_{V_0} d^4x \sum_{\alpha=1}^{4} \sum_{c=1}^{N} |\psi_{\alpha c}(x)|^4, \tag{4.6}$$

where $V_0$ denotes the space-time volume in the continuum, $\alpha$ and $c$ are the Dirac and color indices, respectively. $N$ denotes the number of colors which is in our case equal to three. We assume that the eigenmodes are normalized according to $\int_{V_0} d^4r \sum_\alpha \sum_{c=1}^{3} |\psi_{\alpha c}(x)|^2 = 1$. On the lattice we obtain for the IPR

$$I_{lat} = V a^4 \sum_{x\alpha c} |\psi_{x,\alpha c}|^4, \tag{4.7}$$

where $V = L_t L_s^3$ refers to the number of lattice sites and $a$ is the lattice spacing which we set as usual to one. Note that the analog of this definition in condensed matter physics is widely used. However, in QCD the definition of the IPR in (4.6) is not gauge-invariant so we have to redefine the IPR for our purposes. A simple gauge-invariant version of the IPR is given by

$$I = V \sum_x p_\lambda(x)^2. \tag{4.8}$$

where $p_\lambda(x)$ is the (normalized) gauge-invariant probability density

$$p_\lambda(x) = \sum_{\alpha c} |\psi_{x,\alpha c}|^2. \tag{4.9}$$

Since in Sec. 4.3 we will perform numerical studies with staggered fermions we will work with the following expression for the IPR for staggered fermions

$$I = V \sum_x \left( \sum_c |\chi_{xc}|^2 \right)^2, \tag{4.10}$$

where $\chi_{xc}$ is the one-component staggered field which is normalized to $\sum_{xc} |\chi_{xc}|^2 = 1$. In order analyze the properties of the IPR we calculate the IPR for a completely delocalized state, where completely delocalized means that $p_\lambda(x)$ is the same for all lattice sites, $p_\lambda(x) = 1/V$. In this case we obtain $I = 1$. On the other hand, if the state is completely localized, which means that the state is localized on a single lattice site, $p_\lambda(x) = \delta_{xx_0}$, then we can easily find $I = V$.

In Sec. 4.3 we also will show results for the averaged inverse participation ratio $\langle I \rangle$. In particular we have calculated the lowest eigenvalues. In order to perform the ensemble average we calculate the IPR for every calculated eigenvalue for all configurations. Then we take the average for (say) the lowest eigenvalue of each configuration, and then the average for the second lowest eigenvalue and so on. Furthermore, we also build the average of the lowest eigenvalue, and the second lowest and so. Finally, we plot the averaged IPR vs. the corresponding averaged eigenvalues. Note that we will show only plots for positive eigenvalues since the eigenvalues of the Dirac operator come in pairs of $\pm\lambda$, so we cannot gather no new information from that.

Finally, we like to compare the IPR from our lattice QCD results with the chiral random matrix prediction. Note that for staggered fermions we have to use the chiral Gaussian unitary ensemble (chGUE). In this case we obtain for the averaged IPR for arbitrary $N$ [58, 60]

$$\langle I_2 \rangle = \frac{(N+1)V}{NV+2} \overset{V\to\infty}{\longrightarrow} 1 + \frac{1}{N} \quad \text{for } N \geq 3\,. \tag{4.11}$$

In our case we obtain a value for the averaged IPR of 4/3. So, the eigenmodes of the Dirac operator are delocalized. This can be motivated because we know that the Dirac operator in random matrix theory has random entries. Therefore, we expect that the eigenvectors of the Dirac operator also show a random localization somehow. This is exactly what we obtain. Note that the result for the chRMT prediction does not depend on the eigenvalue.

## 4.3 Calorons on the Lattice: Numerical Results

In this section we will search for calorons on the lattice. In doing so we will not use properties of the gauge field but of the fermion field only, i.e. we will not use any cooling methods. (For investigations using cooling, see, e.g., Refs. [61, 62].) By using only the fermion fields for our analysis we circumvent the problems connected to the direct investigation of global topological properties of the gauge fields.

In the following we use staggered fermions with Wilson and Lüscher-Weisz gauge action for our lattice studies. For an overview of the used lattices see Table 4.1. Note that the ensembles with Lüscher-Weisz gauge action with $\beta = 8.10$ and $\beta = 8.45$ correspond to temperatures below and above the confinement phase transition, respectively. The three ensembles with Wilson action with $\beta = 5.8/6.1/6.3$ have temperatures which are below, at, and above $T_c$.

We begin with the plot in Fig. 4.1 which is similar to those presented in Fig. 3.7. We plotted the chirality of the lowest 10 eigenvalues for Wilson gauge action for

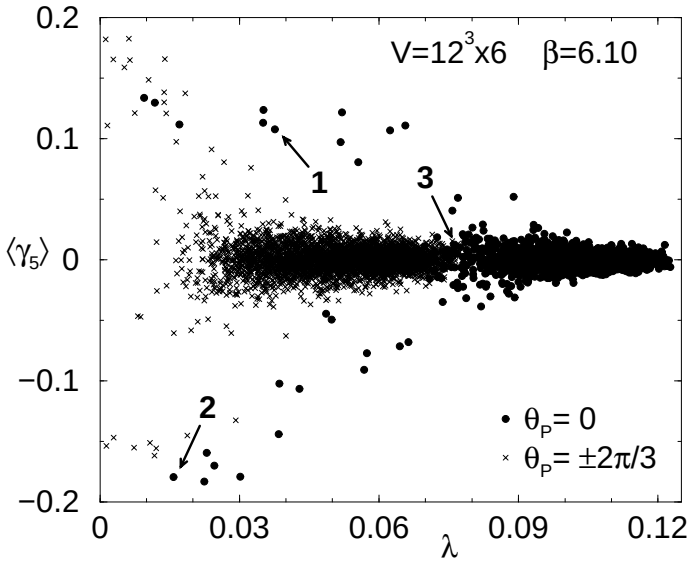


**Figure 4.1:** $\langle\gamma_5\rangle$ vs. $\lambda$. We plotted the lowest 10 eigenvalues. We used the Wilson gauge action on a $12^3 \times 6$ lattice at $\beta = 6.10$ for both sectors, $\theta_P = 0$ and $\theta_P = \pm 2\pi/3$.

both sectors of the Polyakov loop near the critical temperature $T_c$ of the confinement phase transition. As already discussed in Sec. 3.5.2, for both sectors we find small eigenvalues with high chirality while the larger eigenvalues (of the bulk spectrum) have chirality near zero. The low-lying eigenvalues with a large value of $\langle\gamma_5\rangle$ are supposed to be of topological origin. In the following we will take a deeper look at three special eigenvalues which we labeled 1 to 3 in Fig. 4.1. These eigenvalues represent the typical properties of such eigenvalues. This means that other low-lying eigenvalues with large chirality show similar localization properties like eigenvalues one and two. The same is true for eigenvalue number three. Note that eigenvalue number three belongs to the low-lying eigenvalues of the bulk spectrum. It turns out that the low-lying eigenvalues of the bulk in general show different localization properties than the large eigenvalues of the bulk.

Eigenvalues number one and two are small eigenvalues with large chirality while eigenvalue number three has low chirality. Let us investigate the localization of the eigenmodes with respect to their chirality. In Fig. 4.2 we present a scatter plot of the localization of the eigenmodes, i.e. the IPR, vs. $\langle\gamma_5\rangle$. The same eigenvalues as in Fig. 4.1 are depicted. First, we notice that the eigenvalues of the real Polyakov sector are more localized in general than the eigenvalues of the complex sector, which can be seen by the larger values of the IPR. This is a first sign indicating that there are indeed calorons on the lattice, since we have learned in Sec. 4.1 that the zero modes of calorons are more localized in the real sector than in the complex sector. However, most eigenvalues have low chirality and are less localized. As we can guess from Fig. 4.1 these eigenvalues are from the bulk of the spectrum and correspond to the nonzero modes in the continuum. Furthermore, there are several eigenvalues which are more localized and have a more or less high value of $\langle\gamma_5\rangle$. These modes are

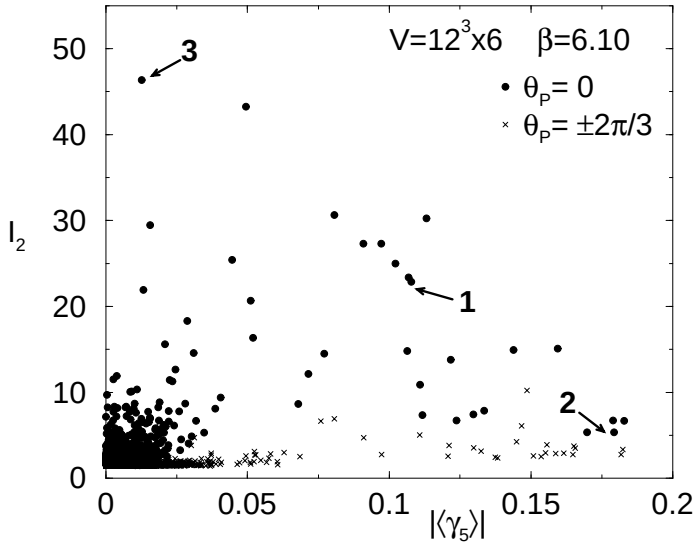


**Figure 4.2:** A scatter plot of the localization vs. chirality. We show the same eigenvalues as in Fig. 4.1.

supposed to be calorons. We already mentioned that those modes are more localized in the real sector which is one fermionic property of the caloron. We will study this effect later on in more detail. Before we will check another property common to the zero mode of the caloron let us have a look onto the highly localized eigenvalues with low chirality. These modes are not expected to be of topological origin because of the low chirality they have. However, let us be inspired by the instanton picture of chiral symmetry breaking. Because we are near the critical temperature we expect the ensemble under investigation to show properties of the instanton liquid phase as well as of the instanton gas phase. In the gas phase we expect to find IA molecules. The low-lying modes of these molecules are supposed to be strongly localized and have zero chirality. Further, the eigenvalues are shifted away from zero. Eigenvalue number three shows all these properties which suggests that this eigenvalue corresponds to an IA molecule. We will present more evidence for this claim later on.

In the following we will investigate the localization patterns of the eigenmodes of our numerical data. We know that the zero mode of a caloron is localized in space and delocalized in time. This is different to the single instanton solution which is

| $\beta_1/\beta$ | 5.8 | 6.1 | 6.3 | 8.10 | 8.45 |
|---|---|---|---|---|---|
| SU(3) $12^3 \times 6$ | 500 | 500 | 500 | 1000 | 1000 |
| SU(3) $16^3 \times 6$ | – | – | – | 500 | 500 |
| SU(3) $20^3 \times 6$ | – | – | – | 350 | 350 |

**Table 4.1:** Overview of the calculated ensembles for the Wilson and Lüscher-Weisz gauge action. The values with $\beta_1 = 8.10$ and $\beta_1 = 8.45$ correspond to the Lüscher-Weisz gauge action while the other three values of $\beta$ correspond to the Wilson gauge action.

localized in space and time. We begin with mode number one of Fig. 4.2, which is supposed to be a caloron state. In the upper plot on the left hand side of Fig. 4.3 we show the density $|\psi(x)|^2$ of mode 1 for the full four-dimensional space-time. This way of plotting maybe not clear at once. Therefore we will explain this plot in more detail. We start at time $t = 0$. For fixed time we have a three-dimensional spatial lattice which, in this case, is a cube. We divide this cube into two-dimensional planes with (say) fixed $z$. We line up these planes (say) in $y$-direction (or in $j$-direction, see Fig. 4.2). The same can be done for the cube with $t = 1$. Again, we line up the slices of this cube next (in $x$-direction or $i$-direction) to the line of $t = 0$, and so on. We obtain a plane which consists of $N_t \times N_s$ two-dimensional $x$-$y$-slices which shows the full space-time. (If this is not yet clear enough, take a look at the caption in Fig. 4.3.)

Let us analyze the plot now. We start with $t = 0$ and the first slice in $j$-direction. We nicely see that the eigenmode is localized in space. For the $j$-direction we find that the modes is localized around $j = 100$. This corresponds to a value of $z$ of about 8. By looking at a single $x$-$y$-slice we also find that the eigenmode is localized around $x = 11$ and $y = 1$. By looking at the other $t$-slices in $i$-direction we observe that the eigenmode is delocalized in time, although the mode is peaked about $t = 4$. This is exactly what we expect for the zero modes of calorons. Another piece of evidence can be given by looking at the chiral density which we plotted in the lower plot on the left hand side of Fig. 4.3. The chiral density is just the local chirality which is given by expression (3.12) without averaging over space-time,

$$\langle \gamma_5 \rangle (x) = \frac{1}{2^4 4!} \sum_{\substack{\mu \\ \mu_i \neq \mu_j}} (-1)^{x_1+x_3} \, \bar{\chi}_{\left(x+\sum_{i=1}^{4} \hat{\mu}_i\right)} \prod_{j=1}^{4} U^{\dagger}_{\left(x+\sum_{i=1}^{j-1} \hat{\mu}_i\right)\mu_j} \chi_x. \tag{4.12}$$

In the plot we observe that the chiral density is not arbitrary distributed but follows the density of the eigenmode. This means that the localized volume of the mode is of topological origin which is further evidence for our assumption that the eigenmode under investigation is a caloron. Similar plots of an eigenmode of the Dirac operator which is supposed to be a zero mode of a caloron are shown in Fig. 4.4 and Fig. 4.5. On the left hand side of Fig. 4.4 we plotted isosurfaces of the density, on the right hand side we show the corresponding isosurfaces of the chiral density. In the upper row we plotted the three-dimensional lattice for a fixed value of $z$. The full density in the volume, which is covered by the isosurface has a value which larger than some parameter value. Illustratively, this means that the quark mostly can be found in the volume covered by the isosurface. From the plots in the first row it follows that the mode is delocalized in time and that the chiral density follows the density. In the plots of the lower row we hold the time fixed and plotted the spatial volume. We see that the mode is clearly localized in space as it is predicted for a zero mode of the caloron. Again, the chiral density follows the density of the eigenmode. This we illustrate in more detail in Fig. 4.5 where we plotted the chiral density and the density into one plot, each for fixed $t$ and fixed $z$. We nicely see that the density and the chiral density are localized at the same region.

Note that mode 2 of Fig. 4.1 shows a similar localization pattern like mode 1, but the width of mode 2 is larger which is the reason for its lower value of the IPR. This

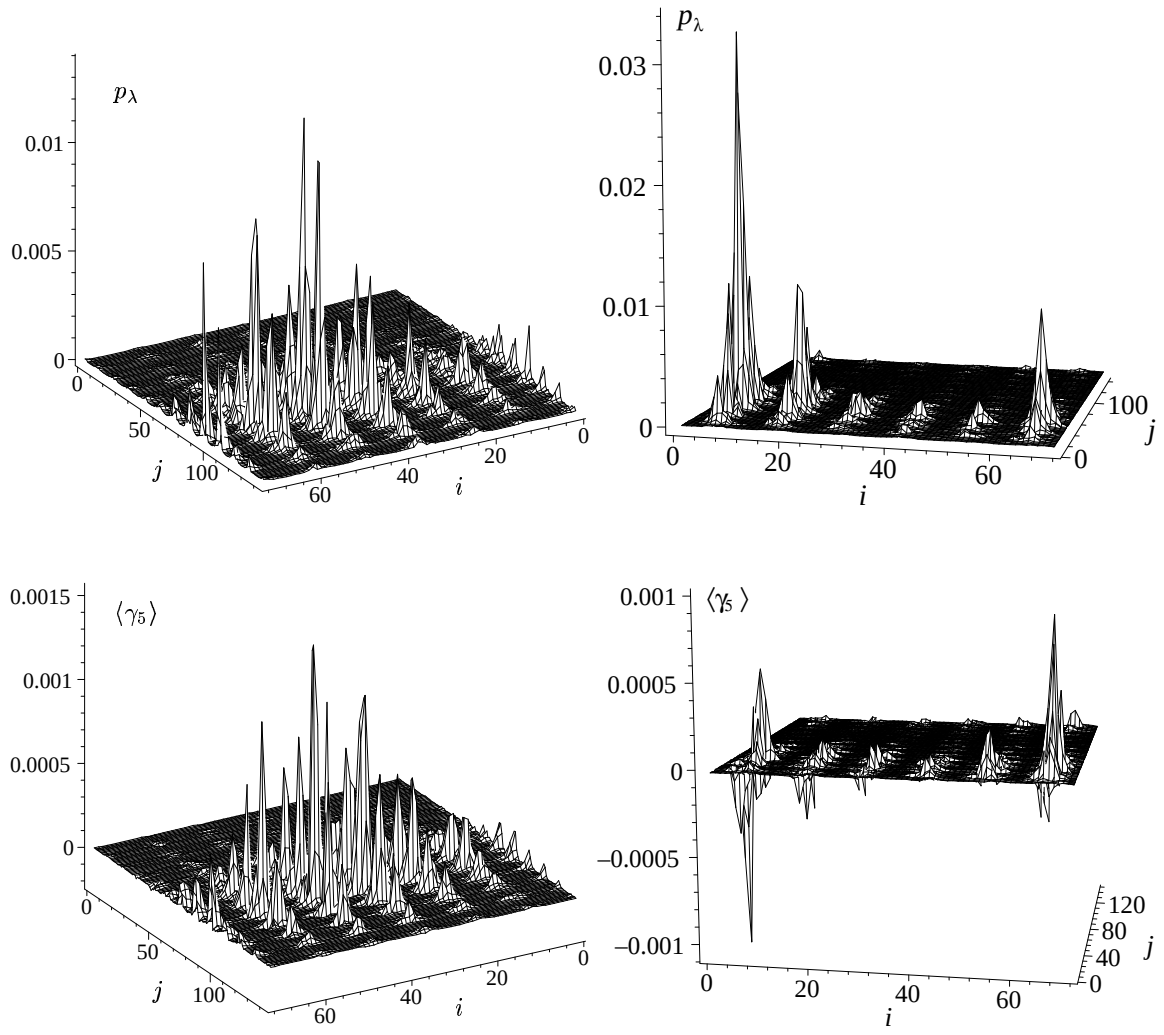


**Figure 4.3:** In the upper plots we show the density of mode 1 (left-hand side) and mode 3 (right-hand side) of Figs. 4.1 and 4.2 on a $12^3 \times 6$ lattice for $\beta = 6.1$ in the $\theta_P = 0$ sector. We have defined the coordinates $i = x + 12t$ and $j = y + 12z$ with the lattice coordinates $x, y, z = 0, 1, \ldots, 11$ and $t = 0, \ldots, 5$. The corresponding local expectation value of $\gamma_5$ is plotted in lower row.

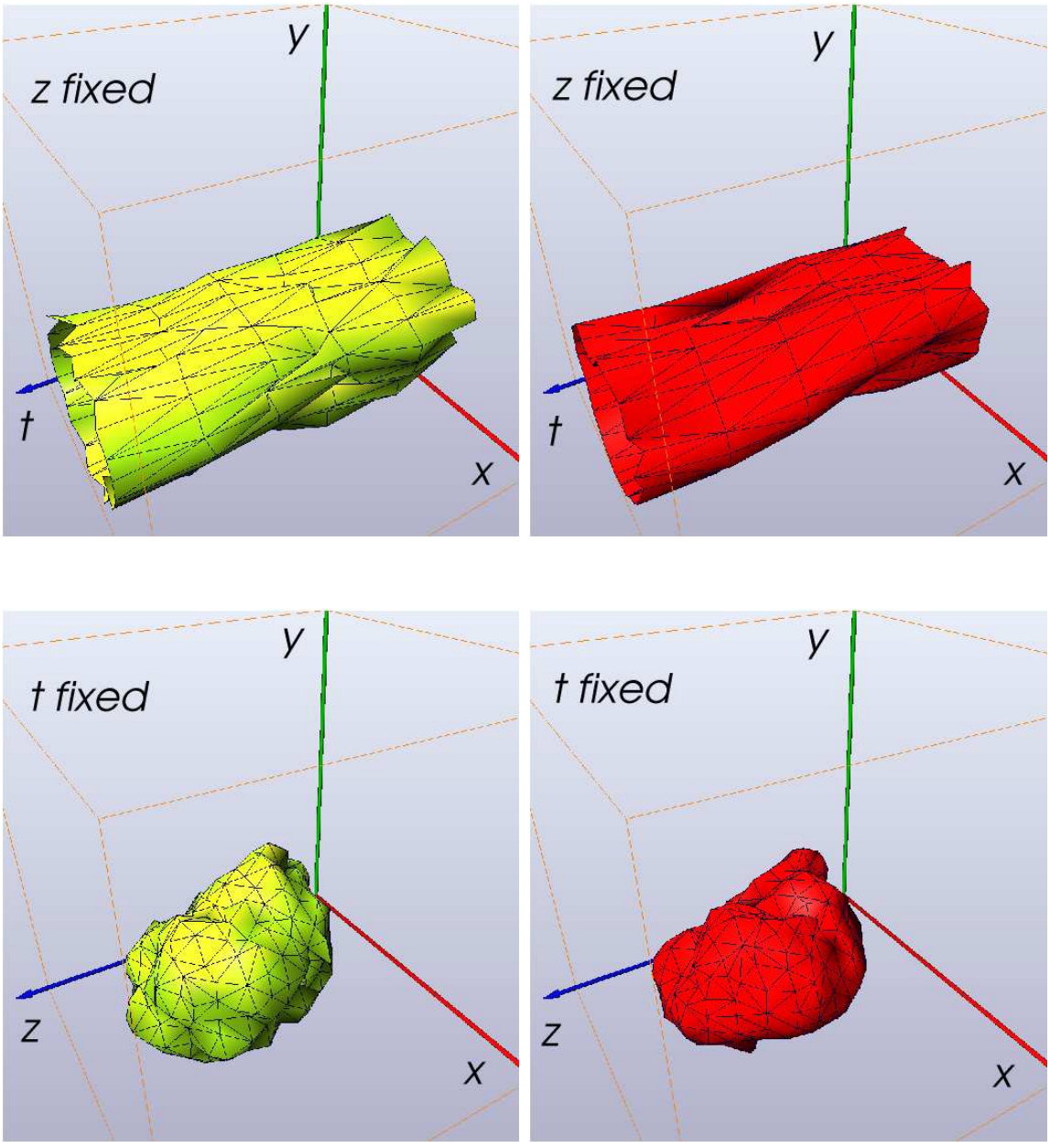


**Figure 4.4:** Isosurfaces of a 'caloron' state which has similar properties like mode 1 or 2 of Figs. 4.1 and 4.2. The columns on the left hand side show the localization while on the right hand side we plotted the corresponding local chirality. In the upper row we show the three-dimensional lattice with fixed $z$ coordinate. We see that both quantities are extended in time. In lower row we hold the time coordinate fixed and plotted the spatial lattices. We observe that both, the density and the chiral density are localized in space.

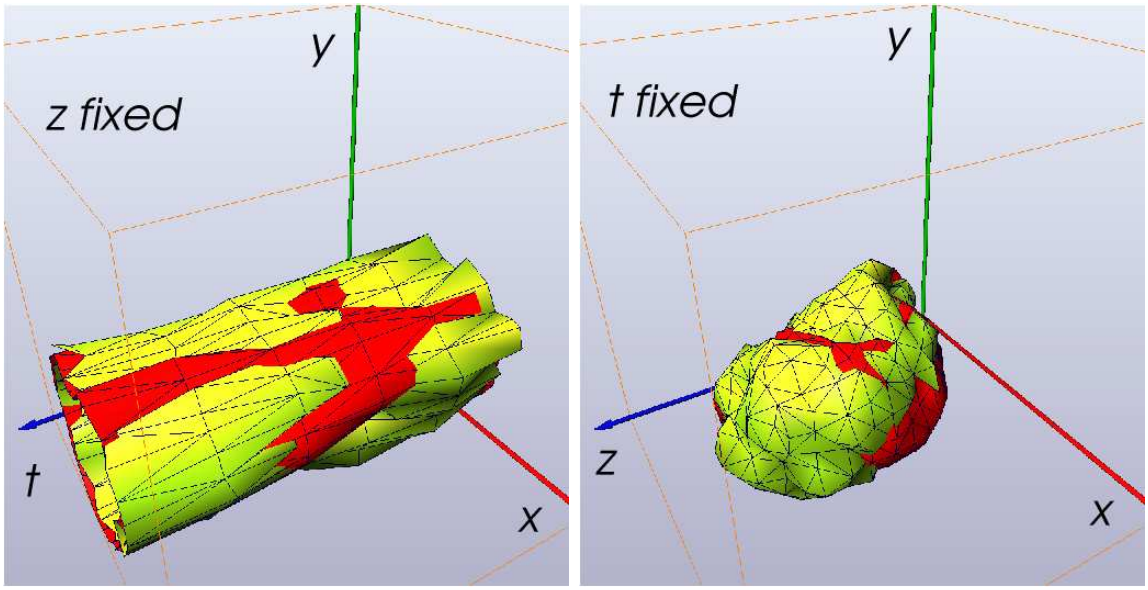


**Figure 4.5:** We plotted the same isosurfaces of the local chirality and the density of Fig. 4.4 in one plot, each for fixed $t$ and fixed $z$. We see that the chiral density follows the density which reflects the topological property of the mode.

suggests that mode 2 corresponds to a zero mode of a calorons which has a larger size $\rho$ than the corresponding caloron of mode 1. Mode 3 has a completely different localization pattern, see Fig. 4.3 on the right hand side. Although the chirality of the mode is small we find that there is a region of positive values of the chiral density right next to a region with negative values. We interpret this observation as follows: The region with positive chirality corresponds to a (left-handed) instanton with topological charge $Q = 1$ while the region with negative chirality corresponds to (right-handed) anti–instanton with $Q = -1$. The instanton sits right next to the anti–instanton. Furthermore, we find that the mode is strongly localized. All these observations suggests that mode 3 is a fermionic mode of an IA molecule.

Let us come back to the difference of the localization in the different sectors of the Polyakov loop. In Fig. 4.6 we plotted the averaged IPR vs. the averaged eigenvalue for three different ensembles with temperatures below, at, and above $T_c$. In the low temperature regime we find, of course, no difference in the different sectors since the $Z_3$ symmetry is restored. As we noted already for Fig. 4.2, for temperatures at ($\beta = 6.1$) and above ($\beta = 6.3$) the critical temperature we clearly see the difference in the two different sectors. We observe that the IPR for the real sector is approximately three times larger than for the complex sector. Note that the width of the zero modes of the caloron in the real sector is three times larger than in the complex sector. If a mode occupies a volume which is three times smaller than that of an other mode, i.e. the mode is three times more localized than the other, the IPR of the more localized mode is three times larger. This observation also supports our assumption that there are indeed calorons on the lattice. Note that the bulk of the spectrum Fig. 4.6 follows approximately the prediction of random matrix theory.

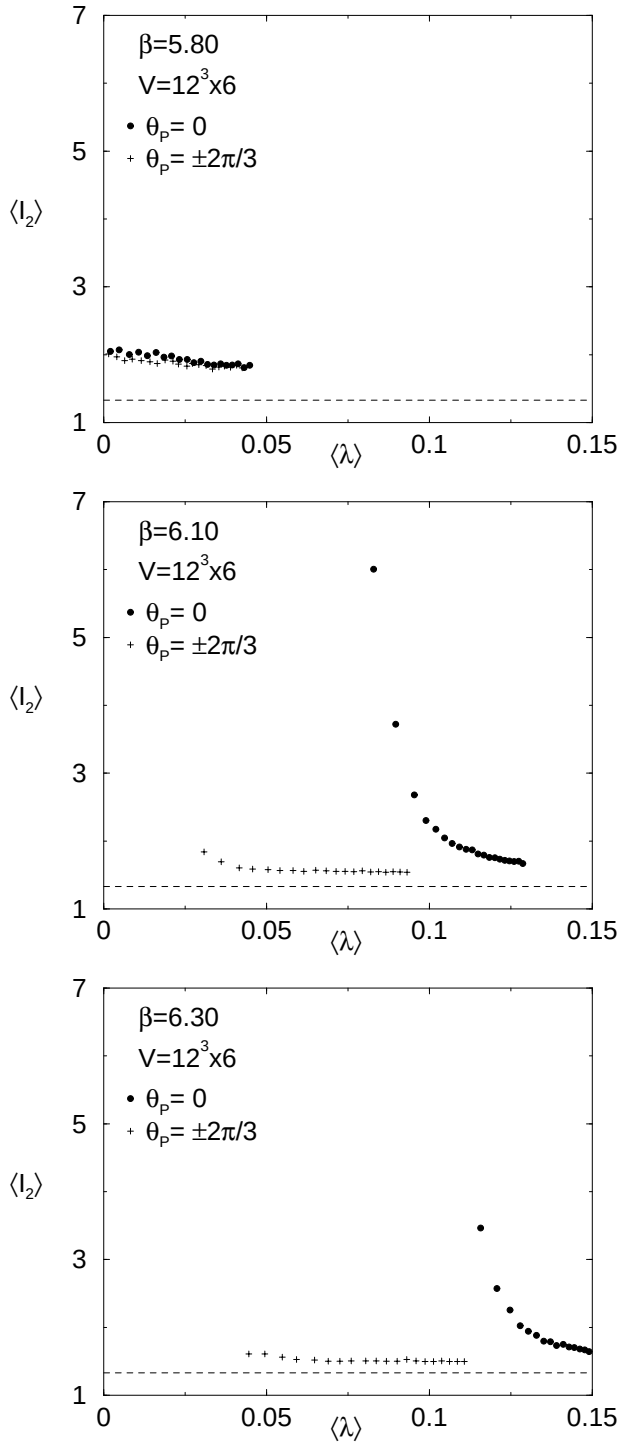


**Figure 4.6:** From top to bottom we plotted the average IPR vs. the averaged eigenvalue for temperatures below, near, and above the chiral phase transition separately for the $Z_3$ sector with $\theta_P = 0$ and the $Z_3$ sectors with $\theta_P = \pm 2\pi/3$. We performed the average for the $1^{\text{st}}$, $2^{\text{nd}}$, ... , $20^{\text{th}}$ eigenvalue of each gauge field configuration. The dashed line is the RMT prediction, 4/3.

Let us summarize this chapter. While for the confinement phase transition the underlying mechanism remains still unclear, we have the instanton picture for the breaking of chiral symmetry. We have discussed the problems of observing instantons or, in general, any topological objects on the lattice. The problems arise because the lattice is not "topologically safe", which means that in lattice simulations instantons can be arbitrarily created or destroyed. In order to circumvent these problems we used other, indirect methods to get informations about the instantons on the lattice. In our studies (at finite temperature) with staggered fermions and Wilson gauge action we searched for calorons on the lattice through the localization properties of the low-lying fermionic modes near and above the chiral phase transition. We found that there are indeed low-lying eigenmodes of the Dirac operator which are supposed to be of topological origin, i.e. modes with high chirality. Furthermore, it turned out that these modes show the characteristic difference of the localization in the different sectors of the Polyakov loop, i.e. the modes are more localized in the real sector than in the complex. The typical localization pattern of 'caloron' states also shows up. That means that the modes under investigation are localized in space but not in time. All in all we have found all the localization properties we expect for calorons which strongly supports the instanton picture. Finally, we note that we also found indications for the existence of IA molecules which is further evidence for the correctness of the instanton picture.

# Chapter 5

# Normal Modes in Random Matrix Theory and QCD

The history of random matrix theory (RMT) begins about 50 years ago with Wigner in the field of nuclear physics. He studied the statistical properties of excited energy levels of complex nuclei. Those systems are characterized by their complicated dynamics. Wigner, nevertheless, found a way to describe certain properties of such systems. He had the idea to replace the complicated matrix of the Hamiltonian by a random matrix with appropriate symmetry properties. Observables are then calculated by averaging over an ensemble of random matrices which follow a certain probability distribution, usually taken to be Gaussian. This probability distribution depends on the symmetries of the underlying theory. Without going into all the details we just want to give examples. If the quantum mechanical Hamiltonian is not invariant under time reversal transformations the corresponding random matrix has to be complex Hermitian and the RMT ensemble is called unitary ensemble (UE) or Gaussian unitary ensemble (GUE) if a Gaussian distribution is used. A system which is rotationally invariant and also invariant under time reversal is described by a real symmetric matrix. The corresponding ensemble is the orthogonal ensemble (OE) or GOE if a Gaussian distribution is used. An nice overview of RMT can be found in Ref. [63].

Anyway, if we know which RMT ensemble should describe our system under investigation then the task is to determine quantities which do not depend on the details of the dynamics of the systems but only on the global symmetries of the problem. These quantities are called universal quantities. Usually, universal quantities can be calculated more easily in RMT than in the original theory. But it is easy to guess that a formal proof of the universality of those quantities is difficult because of the complex structure of the underlying theory. Anyway, since Wigner's great idea huge progress has been made in a variety of different fields including QCD.

In this chapter we will introduce and apply an interesting tool which turns out to be very useful in RMT, namely the so-called normal modes. Normal modes are the eigenmodes of a specific correlation matrix. As mentioned above in RMT the random matrices follow a certain probability distribution $P$. This probability distribution can

be represented as a function of the $N$ eigenvalues of the $N \times N$ random matrices, so, we can treat it as function which takes $N$ arguments. This function has a maximum somewhere. If we expand around this maximum up to second order, the linear term vanishes and the quadratic term is given by a correlation matrix. The eigenmodes of this matrix are the normal modes providing us with a natural basis describing the correlated fluctuations near the maximum of $P$. We will derive an analytical expression for the normal modes for the Gaussian ensembles, the Poisson ensemble, and the chiral Gaussian ensembles, see Sec. 5.1, 5.2, and 5.4, respectively. The chiral ensembles (chGUE, chOE, chSE) are expected to describe universal features of chiral QCD. We will compare the predictions of chiral random matrix theory (chRMT), see Sec. 5.3, for the normal modes to lattice QCD data hoping to get some deeper inside into the theory. We won't let the cat out of the bag yet in the introduction but we will see that normal modes are connected to the Thouless energy, the energy which sets the scale for the validity of RMT, see Sec. 5.6.

Beside the comparison of chRMT to lattice QCD, normal modes are related to another interesting feature. The authors in Ref. [64] showed that the zeros of the QCD partition function are trapped by the position of the eigenvalues of the maximum of the probability distribution. The zeros of the partition function, known as the Yang-Lee zeros [65], are related to the chiral phase transition. Yang and Lee showed that at the point when the phase transition occurs the zeros of the QCD partition function hit the real axis. As already mentioned above, the normal modes provide a natural basis near the maximum of the probability distribution and, hence, can be used as tool for studying the Yang-Lee zeros. But this topic will not be the subject of the following work.

We will concentrate on the normal modes and the comparison of chRMT to lattice QCD, investigated here for the first time. We begin with an illustrative example for the case of the GUE to get a better understanding of normal modes.

## 5.1 Normal Modes and the Gaussian Ensembles

We start with the joint probability distribution for the $N$ eigenvalues $x_1, x_2, \ldots, x_N$ for the Gaussian ensembles of $N \times N$ matrices

$$P_{N\beta}(x_1, x_2, \ldots, x_N) = C_{N\beta} \prod_{1 \le i < j \le N} |x_i - x_j|^\beta \, \mathrm{e}^{-\frac{\beta}{2} N \sum_{i=1}^N x_i^2}. \tag{5.1}$$

$\beta = 1, 2, 4$ corresponds to the Gaussian orthogonal (GOE), unitary (GUE), and symplectic ensembles (GSE), respectively. $C_{N\beta}$ is a normalization constant given by

$$C_{N\beta} = \frac{(N\beta)^{N/2+\beta N(N-1)/4}}{(2\pi)^{N/2}} \frac{\Gamma^N(1+\beta/2)}{\prod_{n=1}^N \Gamma(1+\beta n/2)} \, . \tag{5.2}$$

The variance of the Gaussian in Eq. (5.1) is simply given by $\sigma = \frac{1}{\beta N}$. Sometimes, the scaling is different in the literature. Often used variances are $1/\beta$, $2/\beta$, and $\frac{2}{N\beta}$.

With our choice we find for the spectral density $\rho$ for large $N$

$$\rho(x) = \frac{N}{\pi}\sqrt{2 - x^2}. \tag{5.3}$$

So $\rho$ for large $N$ is given by a semicircle which Wigner first derived in 1957. Note that the spectral density is independent of $\beta$ which stays true for any other choice of the variance. This behavior is different for the radius of the semicircle which is independent of $N$ in our particular choice. For example for $\sigma = 1/\beta$ we get $\rho(x) = \frac{1}{\pi}\sqrt{2N - x^2}$.

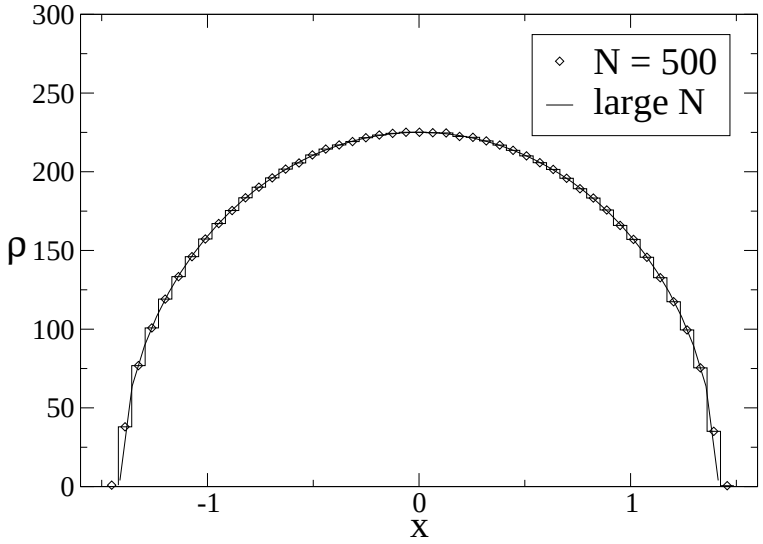


**Figure 5.1:** The analytical result for the eigenvalue density $\rho(x)$ for large N compared to the numerical result for the GUE for $N = 500$. The ensemble contains 2500 configurations.

In the following we will demonstrate how to obtain numerical results out of RMT. For illustration we compare the analytical result for $\rho$ in Eq. (5.3) to the numerical one for the GUE. First, we have to generate an ensemble of $N \times N$ random matrices with complex entries which are normally distributed. We provide hermiticity for the matrices by hand adding the complex conjugate matrix and dividing by 2, $W' = (W + W^\dagger)/2$. Now, we calculate the $N$ eigenvalues for every matrix and determine the spectral density by averaging over the entire ensemble. In Fig. 5.1 we give an example for about 2500 matrices with $N = 500$. The binning of the histogram is about 0.032. The smooth curve is the analytical prediction for the spectral density for large $N$, Eq. (5.3), which is already in very good agreement with the result for $N = 500$. This procedure can be applied in the same way for all numerical calculations of observables which depend on the eigenvalues and eigenvectors of random matrices.

Let us return to the subject of normal modes. The function $P_{N\beta}$ depends on $N$ variables $x_i$. It follows from Eq. (5.1) that $P_{N\beta}$ is symmetric in all its arguments. Therefore, it is sufficient to consider $P_{N\beta}$ only for $x_1 < x_2 < \cdots < x_N$ if we are interested in the extrema. Let us denote the maximum value of $P_{N\beta}$ for this region by $P^0_{N\beta}$. For the equilibrium positions of the $x_i$ one easily obtains the following set of

equations

$$\sum_{i \neq j} \frac{1}{x_i - x_j} - N x_i = 0. \tag{5.4}$$

Near the maximum we can approximate the logarithm of $P_{N\beta}$ by

$$\ln P_{N\beta} = \ln P^0_{N\beta} + \frac{1}{2}\beta \sum_{i,j} \delta x_i \, C_{ij} \, \delta x_j, \tag{5.5}$$

where the matrix $C_{ij}$ is evaluated at the maximum,

$$C_{ij} = \frac{1}{\beta} \frac{\partial^2}{\partial x_i \partial x_j} \ln P_{N\beta} \Big|_{maximum}. \tag{5.6}$$

$C_{ij}$ can be easily calculated and we find

$$C_{ii} = -\sum_{i \neq j} \frac{1}{(x_i - x_j)^2} - N \tag{5.7}$$

$$C_{ij} = \frac{1}{(x_i - x_j)^2}, \quad i \neq j. \tag{5.8}$$

Obviously, this matrix is diagonalizable having real eigenvalues. The corresponding eigenvectors are the so-called normal modes. A normal mode describes a statistically independent mode of correlated motion of the eigenvalues $x_i$. This can be easily understood by looking at Eq. (5.5). By diagonalizing $C_{ij}$ we simply change the coordinate system, $\delta x_i \to \delta y_i$. In the new coordinates (also called normal coordinates) Eq. (5.5) becomes

$$\ln P_{N\beta} = \ln P^0_{N\beta} + \frac{1}{2}\beta \sum_{i,j} \delta y_i \, C'_{ij} \, \delta y_j = \ln P^0_{N\beta} + \frac{1}{2}\beta \sum_i C'_{ii} \, (\delta y_i)^2. \tag{5.9}$$

An analogy can be found in mechanics. Determining the equation of state for a system of masses coupled via springs leads to a set of coupled differential equations. This set can be written in the form "matrix times vector" where the matrix contains the couplings of masses to each other. The matrix can be diagonalized ending up in a system in new coordinates and a set of differential equations which are now decoupled. So for the normal modes this means that they are uncorrelated modes describing a collective motion of the eigenvalues of the random matrix.

To calculate the eigenvalues and eigenvectors of $C_{ij}$ we first have to determine the equilibrium positions $x^0_i$ from Eq. (5.4). With the help of Hermite's differential equation,

$$H''_N(x) - 2xH'_N(x) + 2NH_N(x) = 0, \tag{5.10}$$

which reduces to Eq. (5.4) at the zeros of $H_N$, the $x^0_i$ are given by the zeros of the Hermite polynomial $H_N$ [66]

$$H_N(\sqrt{N} x^0_i) = 0. \tag{5.11}$$

Now the eigenvalues $\widetilde{\omega}_k^G$ and eigenvectors $\delta y_i^{(k)}$ of $C_{ij}$,

$$\sum_{j=1}^{N} C_{ij}\,\delta y_j^{(k)} = \widetilde{\omega}_k^G\,\delta y_i^{(k)}, \tag{5.12}$$

can be determined which is shown in Ref. [67]. The $N$ eigenvalues show up to have a very simple form,

$$\widetilde{\omega}_k^G = -k\,N. \tag{5.13}$$

The $i$-th component of the eigenvectors behave like polynomials of order $k-1$ evaluated at $x_i^0$. For illustration we show the first 4 normalized eigenvectors

$$\delta y_i^{(1)} = \frac{1}{\sqrt{N}} \tag{5.14}$$

$$\delta y_i^{(2)} = \sqrt{\frac{2}{N-1}}\;x_i^0 \tag{5.15}$$

$$\delta y_i^{(3)} = \sqrt{\frac{N-1}{N(N-2)}}\;\left(1-\frac{2N}{N-1}\,(x_i^0)^2\right) \tag{5.16}$$

$$\delta y_i^{(4)} = \sqrt{\frac{2(2N-3)^2}{(N-1)(N-2)(N-3)}}\left(x_i^0-\frac{2N}{2N-3}\,(x_i^0)^2\right). \tag{5.17}$$

One can show that in the limit of large $N$ the $k$-th eigenvector is proportional to the Chebyshev polynomial of the second kind $U_{k-1}(x)$ evaluated at $x = x_i^0/\sqrt{2}$,

$$\delta y_i^{(k)} = \sqrt{N}\,U_{k-1}\left(\frac{x_i^0}{\sqrt{2}}\right). \tag{5.18}$$

This result is not surprising since the orthogonality relation of the eigenvectors,

$$\sum_{i=1}^{N} \delta y_i^{(k)} \delta y_i^{(l)} = \delta_{kl}, \tag{5.19}$$

can be approximated for large $N$ by

$$\int_{-\sqrt{2}}^{\sqrt{2}} \mathrm{d}x\,\rho(x)\;\delta y^{(k)}(x)\;\delta y^{(l)}(x) = \delta_{kl}, \tag{5.20}$$

where $\rho(x)$ is defined by Eq. (5.3). Replacing $\delta y^{(k)}(x)$ above by its approximation from Eq. (5.18),

$$y^{(k)}(x) = \sqrt{N}\,U_{k-1}\left(\frac{x}{\sqrt{2}}\right), \tag{5.21}$$

we find Eq. (5.20) to be the orthogonality relation for Chebyshev polynomials of second kind.

## 5.2 Normal Modes and the Poisson Ensemble

We would like to compare the result for the normal modes for the Gaussian ensembles to that of the Poisson ensemble. We will see that we can also calculate the normal eigenvalues and eigenvectors in that case. However, it is convenient to choose a different approach which is equivalent to the approach above to the extent that the quadratic approximation of $P_{N\beta}$ in Eq. (5.5) is exact.

Instead of calculating the eigenmodes of $C_{ij}$ defined in Eq. (5.6) we calculate the eigenmodes of the following correlation matrix

$$D_{ij} = \langle (x_i - \langle x_i \rangle)(x_j - \langle x_j \rangle) \rangle = \langle x_i x_j \rangle - \langle x_i \rangle \langle x_j \rangle . \tag{5.22}$$

It turns out that the eigenvectors in both approaches are the same and the eigenvalues are the negative reciprocals of one another (if the quadratic approximation is exact). We will denote eigenvalues of $D$ by $\widetilde{\omega}$ while for eigenvalues of the corresponding $C$ matrix we will omit the tilde. So, the eigenvalues are related by $\widetilde{\omega} = -1/\omega$.

Again, we start with the adjoint probability distribution which is given by

$$P_N(x_1, x_2, \ldots, x_N) = \mathrm{e}^{-x_1}\, \theta(x_1) \prod_{i=1}^{N-1} \mathrm{e}^{-(x_{i+1}-x_i)}\, \theta(x_{i+1} - x_i) \tag{5.23}$$

$$= \mathrm{e}^{-x_N}\, \theta(x_1) \prod_{i=1}^{N-1} \theta(x_{i+1} - x_i). \tag{5.24}$$

This describes a spectrum of $N$ uncorrelated levels with unit mean level density. It is easy to calculate the expectation values $\langle x_i \rangle$ and $\langle x_i x_j \rangle$

$$\langle x_i \rangle = \prod_k \int \mathrm{d}x_k \; x_i \, P_N(x_1, x_2, \ldots, x_N) = i \tag{5.25}$$

$$\langle x_i x_j \rangle = \prod_k \int \mathrm{d}x_k \; x_i \, x_j \, P_N(x_1, x_2, \ldots, x_N) = \begin{cases} ij + j, & i > j \\ ij + i, & j > i \end{cases} . \tag{5.26}$$

The correlation matrix $D_{ij}$ takes the simple form

$$D_{ij} = \begin{cases} j, & i > j \\ i, & j > i \end{cases} = \min\{i, j\}. \tag{5.27}$$

Now we can determine the eigenvectors and eigenvalues of $D_{ij}$. With the following definition

$$\phi_k \equiv \frac{\pi\,(2k-1)}{(2N+1)} \tag{5.28}$$

one finds for the components of the eigenvectors [68]

$$\psi_j^{(k)} = \frac{2}{\sqrt{2N+2}} \sin(j\phi_k) \tag{5.29}$$

and the corresponding eigenvalues are

$$\omega_k^P = \frac{1}{4}\sin^{-2}\left(\frac{\phi_k}{2}\right). \tag{5.30}$$

To compare this result to that of the Gaussian ensembles we have to establish identical scales. This can be done by multiplying $\omega_k^P$ by $\frac{1}{\rho(0)^2} = \frac{\pi^2}{2N^2}$. (We have a square in the first term because $D_{ij}$ is quadratic in $x_i$.) It follows that the eigenvalues for large $k$ are of the same order. For the Gaussian ensembles we find $\widetilde{\omega}_N^G = -N^2$ and for the Poisson ensemble we have

$$\widetilde{\omega}_N^P = -\frac{\rho^2(0)}{\omega_N^P} - \frac{\pi^2}{2N^2}\frac{1}{\omega_N^P} = -\left(\frac{8}{\pi}\right)^2 N^2. \tag{5.31}$$

For the soft edge of the spectrum, where "soft" refers to small values of $k$, we find a different behavior. In the uncorrelated case the eigenvalues show a quadratic behavior, $-2k^2$, while for the Gaussian case we have a linear one, $-kN$. This regime of the spectrum will be of particular interest for our numerical calculations which we will present in the next sections.

## 5.3 The Chiral Random Matrix Model

For the derivation of the chiral random matrix model we begin with the QCD partition function in Euclidean space which we formulated in Sec. 2.1.1. The goal is to establish the partition function of QCD in terms of an integral over random matrices. In particular the chiral nature of the Dirac operator plays an important role. We found in Eq. (2.95) that $\not{D}$ has block diagonal form. The first step now is to replace the off-diagonal blocks $T$ in (2.95) by purely random matrices $W$ with appropriate symmetry properties,

$$\not{D} \to \begin{pmatrix} 0 & \mathrm{i}W \\ \mathrm{i}W^\dagger & 0 \end{pmatrix}. \tag{5.32}$$

The entries of the matrix $W$ are random numbers which are generated according to a particular probability distribution. In the case of QCD and for gauge groups $\mathrm{SU}(N_c)$ with $N_c > 3$ the Dirac operator in the fundamental representation has no further symmetries so the random matrix $W$ has to be chosen arbitrary complex. We will see below that if the Dirac operator has certain symmetries we have to account for this. Anyway, the ensemble above is called the chiral unitary ensemble or chUE. If a Gaussian probability distribution is used for the matrix entries it is called chiral Gaussian unitary ensembles or chGUE.

For $N_c = 2$ and fermions in the fundamental representation, see [69], there is indeed an additional symmetry of $\not{D}$. The operator $C\tau_2 K$ commutes with $\mathrm{i}\not{D}$, $[C\tau_2 K, \mathrm{i}\not{D}] = 0$, where $C$ is the charge conjugation operator, $\tau_i$ are the Pauli matrices, and $K$ is the operator of complex conjugation. This symmetry enables us to choose a basis in which

$W$ is real [69, 70]. This is called the chiral orthogonal ensemble (chOE or chGOE in case of a Gaussian probability distribution).

Finally, a third ensemble enters the game. Fermions in the adjoint representation of the gauge group, see [69], also have a particular symmetry. Without going into details we claim that the Dirac operator commutes with $CK$ and thus can be diagonalized by a symplectic transformation [69, 71]. This means that the elements of $W$ are quaternions. The corresponding ensemble is the chiral symplectic ensemble (chSE or chGSE).

Note that the random matrix in Eq. (5.32) is still anti–hermitian because of the block structure. This structure can be spoiled in some random matrix models for lattice QCD. So, e.g., for Wilson fermions chiral symmetry is explicitly broken which means that the Dirac operator has no block structure any more. In this case we preserve hermiticity by choosing a hermitian matrix for the Dirac operator. The corresponding ensemble is the UE for $N_c \geq 3$ and the OE for $N_c = 2$, respectively. In our numerical studies we use staggered fermions which are described by the chUE for $N_c \geq 3$ and the chSE for $N_c = 2$, see Ref. [69].

The eigenvalues of the Dirac operator can be zero or they come in pairs of $\pm\lambda_i$. If the Dirac operator has zero modes then the corresponding gauge field has a non–vanishing topological charge. We can have zero modes also in our random matrix model and, therefore, simulate different topological sectors. We choose the matrix $W$ to be of dimension $N \times (N+\nu)$ where we assume $\nu \geq 0$. The matrix in Eq. (5.32) then has $N$ eigenvalues $\pm\lambda_i$ $(i = 1, \ldots, N)$ and $\nu$ zero modes. From lattice studies we know that gauge field configurations with large topological charge are rare, see Ref. [33, 72], so we will assume $\nu \ll N$ and we can identify the volume $V = 2N + \nu \approx N$.

For the second step we have a look at the integration in the partition function. In Eq. (2.12) we integrated out the fermions fields and only the integration over the gauge field remains. The integration can be understood as summing up all possible probabilities

$$P(A) \sim \mathrm{e}^{-S_g} \prod_{f=1}^{N_f} \det(TT^\dagger + m_f^2). \tag{5.33}$$

For the calculation of spectral quantities we have to average over the gauge fields which are distributed according to the probability given above. We simulate this in chiral RMT by replacing the average over the gauge fields by an average over random matrices. In doing so we replace the $T$-blocks of the determinant in Eq. (5.33) by random matrices $W$ as discussed above, and the gluonic part is replaced by a convenient distribution of the random matrix $W$,

$$P(W) \sim \mathrm{e}^{-NV(W)} \prod_{f=1}^{N_f} \det(WW^\dagger + m_f^2). \tag{5.34}$$

From universality arguments one can argue that all relevant results should not depend on the specific choice of $V(W)$, provided that it is well-behaved and invariant under

similarity transformations. There are several proofs of this universality conjecture, see [73, 74, 75]. A convenient choice is a Gaussian distribution,

$$V(W) = \frac{\beta\Sigma^2}{2}\mathrm{Tr}\, WW^\dagger, \tag{5.35}$$

where $\Sigma$ is the absolute value of the quark condensate, see Eq. (2.99). Note that compared to Eq. (2.99) we have an additional factor $1/N$ in our definition of $\Sigma$ and write

$$\Sigma = \lim_{\lambda\to 0}\lim_{m_f\to 0}\lim_{N\to\infty}\frac{\pi\rho(\lambda)}{N}. \tag{5.36}$$

The label in Eq. (5.35) is the so-called Dyson index. It stands for the orthogonal, unitary, and symplectic ensemble, respectively, and can take the values $\beta = 1, 2, 4$.

Now we achieved what we desired at the beginning of this section. We have written the probability distribution in Eq. (5.33) entirely in terms of random matrices and, therefore, the partition function of the chiral random matrix model can be written as an integral over random matrices,

$$Z^{N_f,m_f,\nu}_{N,\beta} = \int \mathrm{D}W \prod_{f=1}^{N_f}\det(WW^\dagger + m_f)\mathrm{e}^{-\frac{N\beta\Sigma^2}{2}\mathrm{Tr}(W^\dagger W)}. \tag{5.37}$$

This is the starting point for our calculation of the normal modes in the chiral random matrix model which we will perform in the next section.

## 5.4 Normal Modes and the Chiral Random Matrix Model

Now we are prepared to derive an analytical expression for the normal modes in the chiral random matrix model for QCD. Following Ref. [64] we begin with the partition function in Eq. (5.37). As we noted in the last section the integrand of (5.37) is invariant under similarity transformations. Therefore, we can perform the following transformation, $W \to U^\dagger W V$. Let the matrix $W$ have dimension $N$. Then, the matrix $U$ is of dimension $N \times N$ while $V$ is a $(N+\nu)\times(N+\nu)$ matrix. We can choose the transformation such that we diagonalize $W$. We have $W = U^\dagger \Lambda V$ where $\Lambda$ is a $N \times (N+\nu)$ matrix with $\Lambda_{ii} = \lambda_i$ $(i = 1, \ldots, N)$ and $\Lambda_{ij} = 0$ otherwise. So, the $\lambda_i$ are the $N$ nonzero modes (Note that there are $\nu$ zero modes). With such a transformation the partition function can be written as

$$Z^{N_f,m_f,\nu}_{N,\beta} = \left(\prod_{f=1}^{N_f} m_f^{|\nu|}\right)\int_{-\infty}^{+\infty}\cdots\int_{-\infty}^{+\infty}\prod_{k=1}^{N}\left[\mathrm{d}\lambda_k\prod_{f=1}^{N_f}(\lambda_k^2+m_f^2)\lambda_k^{\beta\nu+\beta-1}\mathrm{e}^{-\frac{N\beta}{2}\lambda_k^2}\right]\left|\Delta(\lambda^2)\right|^\beta, \tag{5.38}$$

where we have set $\Sigma = 1$. The term $(\lambda_k^2 + m_f^2)$ corresponds to the determinant in Eq. (5.37). The exponential comes from the gluonic part and the Jacobian of this transformation is given by

$$J = \left|\Delta(\lambda^2)\right|^\beta \prod_{k=1}^{N} \lambda_k^{\beta\nu+\beta-1}, \tag{5.39}$$

where the so-called Vandermonde determinant $\Delta$ is defined by

$$\Delta(\lambda^2) = \prod_{k<l}(\lambda_k^2 - \lambda_l^2). \tag{5.40}$$

As we already noted in Sec. 5.3 we can write the partition function as an integral over the probability distribution. So here we obtain

$$Z_{N,\beta}^{N_f,m_f,\nu} = \int_{-\infty}^{+\infty} \cdots \int_{-\infty}^{+\infty} \prod_{k=1}^{N} \mathrm{d}\lambda_k P_{N,\beta}^{N_f,m_f,\nu}(\lambda_1,\ldots,\lambda_N) \tag{5.41}$$

with the joint probability density

$$\begin{aligned} P_{N,\beta}^{N_f,m_f,\nu}(\lambda_1,\ldots,\lambda_N) = \\ \left(\prod_{f=1}^{N_f} m_f^{|\nu|}\right) \prod_{k=1}^{N} \left[\prod_{f=1}^{N_f} (\lambda_k^2 + m_f^2)\lambda_k^{\beta\nu+\beta-1} \mathrm{e}^{-\frac{N\beta}{2}\lambda_k^2}\right] \left|\Delta(\lambda^2)\right|^\beta . \end{aligned} \tag{5.42}$$

We now concentrate on the case $\beta = 2$, the chiral unitary ensemble. Remember that this corresponds to the universality class of QCD with 3 quarks in the fundamental representation and also to staggered fermions in lattice QCD for which we will present numerical data later on.

In order to determine the dispersion relation of the normal modes we follow the derivation of Sec. 5.1. We first like to determine the maximum of the joint probability distribution. Again we can restrict ourselves to the region of $P_N^{N_f,m_f,\nu}$ where $\lambda_1 < \lambda_2 < \cdots < \lambda_N$. We introduce new coordinates $y_i = \lambda_i^2$. Evaluating the maximum condition,

$$\frac{\partial \ln P_N^{N_f,m_f,\nu}}{\partial y_i} = 0, \tag{5.43}$$

we find for $N_f = 0$ the following set of equations

$$\left(\nu + \frac{1}{2}\right)\frac{1}{Ny_i} - 1 + \frac{1}{N}\sum_{i\neq j}\frac{2}{y_i - y_j} = 0. \tag{5.44}$$

We will concentrate on the case $N_f = 0$ because this corresponds to the quenched approximation in lattice QCD which we use in our numerical analysis. We denote the maximum position of the eigenvalues fixed by the equations above by $\lambda_i^0$, and the

maximum of $P_N^{N_f,m_f,\nu}$ by $P_{N;0}^{N_f,m_f,\nu} \equiv P_N^{N_f,m_f,\nu}(\lambda_1^0,\ldots,\lambda_N^0)$. Near the maximum the logarithm of $P_N^{N_f,m_f,\nu}$ can be approximated by

$$\ln P_N^{N_f,m_f,\nu} \approx \ln P_{N;0}^{N_f,\nu} + \frac{1}{2} C_{ij}\delta\lambda_i\delta\lambda_j, \tag{5.45}$$

where $\delta\lambda_i$ is the position of the $i$th eigenvalue relative to $\lambda_i^0$. Note that the linear term vanishes. The matrix $C_{ij}$ is defined by

$$C_{ij} = \frac{\partial^2}{\partial\lambda_i\partial\lambda_j} \log P_N^{N_f,m_f,\nu} \tag{5.46}$$

evaluated at the maximum. After a short calculation we obtain for the diagonal elements of $C_{ij}$ for $N_f = 0$

$$C_{ii} = -2N - \frac{2\nu+1}{\lambda_i^2} - 4\sum_{i\neq j} \frac{\lambda_i^2+\lambda_j^2}{(\lambda_i^2+\lambda_j^2)^2} \tag{5.47}$$

and for the off–diagonal entities one obtains

$$C_{ij} = \frac{8\lambda_i\lambda_j}{(\lambda_i^2+\lambda_j^2)^2}. \tag{5.48}$$

The eigenvectors and eigenvalues of this matrix are the desired normal modes. They are defined by the eigenvalue equation

$$\sum_{i=1}^{N} C_{ij}\phi_j^{(k)} = \omega_k^\chi \phi_i^{(k)}. \tag{5.49}$$

The normal modes can be used as a coordinate system which means that we can express the $\delta\lambda_i$s in terms of the normal modes

$$\delta\lambda_i = \sum_{k=1}^{N} c_k \phi_i^{(k)} \quad \text{with} \quad \sum_{i=1}^{N} \phi_i^{(k)}\phi_i^{(k')} = \delta_{kk'}. \tag{5.50}$$

Remember the interpretation of the normal modes (see Sec. 5.1). The normal modes describe statistically uncorrelated fluctuations of the eigenvalues of the random matrix about their most probable value.

Following the steps in Sec. 5.1 a similar derivation leads to an expression for the eigenvalues. One finds again a linear dispersion relation which is reasonable because the chiral ensembles and the Gaussian ensembles of Sec. 5.1 are very similar,

$$\omega_k^\chi = -4\,k\,N. \tag{5.51}$$

The different factor comes from the chiral structure of the random matrix model we used. Note that $\omega_k^\chi$ does not depend on the topological sector $\nu$.

As we have already done in Sec. 5.1 we can approximate the eigenvectors for large $N$ by Chebyshev polynomials evaluated at the maximum position $\lambda_i^0/2$ (i.e. up to corrections of order $1/N$)

$$\phi_i^{(k)} = \sqrt{\frac{2}{N}}\, U_{2k-1}\left(\frac{\lambda_i^0}{2}\right). \tag{5.52}$$

In this limit the orthogonality relation of Eq. (5.50) corresponds to

$$\int \mathrm{d}x\, \rho(x)\, \phi^{(k)}(x)\, \phi^{(k')}(x) = \delta_{kk'}, \tag{5.53}$$

where $\rho(x)$ is again the well-known semicircle

$$\rho(x) = \frac{N}{\pi}\sqrt{4 - x^2}. \tag{5.54}$$

Now that we have an analytical expression for the dispersion relation of the normal modes we can perform numerical calculations of "full" QCD, which in our case means quenched lattice QCD, and compare both. Before we will return to this we will have to discuss a further subtlety of RMT.

## 5.5 Unfolding

Random matrix theory can be regarded as an effective theory which describes certain properties of the underlying theory. So there are quantities for which RMT agrees with the full theory (at least for a certain regime) and quantities which show different behavior. RMT is supposed to describe quantities correctly on the smallest scale in the system. This scale is set by the mean level spacing which means that RMT applies on a scale of a few level spacings.

For illustration take a look at the global spectral density or mean level density $\rho(x)$ in Fig. 5.1. Imagine we have a certain physical problem for which we have calculated the global spectral density. We would like to compare this quantity to the result we obtained from some random matrix model. Then we would see that the RMT result cannot reproduce the data. This is simply because the quantity under consideration reflects only the global properties, not the microscopic ones.

To apply RMT to physical problems we have to eliminate the system specific dependencies. We have to go to an energy scale where the fluctuations of the eigenvalues become visible and the system specific dependence of the mean level spacing is removed. We can achieve this by a local rescaling of the energy scale. This procedure is called unfolding and is essential for comparing RMT predictions to physical systems. Let us therefore introduce new coordinates for the eigenvalues

$$\xi_p \equiv \xi_p(x_p) = \int_{-\infty}^{x_p} \rho(x'_p)\, \mathrm{d}x'_p. \tag{5.55}$$

In these new coordinates the transformed mean level density $X_1(\xi_1)$ equals unity which easily follows by integrating both sides of the transformation equation: $\rho(x_p)\,\mathrm{d}x_p = X_1(\xi_p)\,\mathrm{d}\xi_p$ where we set $X_1(\xi_p) = 1$ to get rid of the system specific dependence of the mean level density. Of course we have to express all quantities of interest in the new coordinates. We will demonstrate how to achieve this for the case of the $k$-point spectral correlation functions in the limit $N \to \infty$. The $k$-point spectral correlation functions are given by

$$R_k(x_1, \ldots, x_k) = \frac{N!}{(N-k)!} \int_{-\infty}^{+\infty} \mathrm{d}x_{k+1} \cdots \int_{-\infty}^{+\infty} \mathrm{d}x_N \, P_N^{(E)}(x_1, \ldots, x_N). \tag{5.56}$$

Here $P_N^{(E)}(x_1, \ldots, x_N)$ denotes the probability density for an arbitrary RMT ensemble. The spectral correlation functions measure the probability of finding levels at the positions $x_1, \ldots, x_k$, while the remaining levels are not observed. Notice that $\rho(x_1) \equiv R_1(x_1)$. Performing the change of coordinates in the large $N$ limit we find for the spectral correlation function times its differentials the following expression

$$X_k(\xi_1, \ldots, \xi_k)\,\mathrm{d}\xi_1 \cdots \mathrm{d}\xi_k = R_k(x_1, \ldots, x_k)\,\mathrm{d}x_1 \cdots \mathrm{d}x_k \quad (N \to \infty) \tag{5.57}$$

preserving the total probability. Note that we have $X_1(\xi_1) = 1$ by construction. Because the spectrum in the new coordinates, for large $N$, is supposed to be translational invariant it is sufficient to perform the unfolding procedure only for a small region of the spectrum (provided that in the large $N$ limit this region contains many levels). We choose this region to be around zero and have $\xi_p = x_p/D$ where $D = 1/R_1(0)$ is the mean level spacing. So the unfolded correlation functions are given by

$$X_k(\xi_1, \ldots, \xi_k) = \lim_{N\to\infty} D^k R_k(D\xi_1, \ldots, D\xi_k), \tag{5.58}$$

where the new energy variables are held fixed while taking the limit.

## 5.6 Normal Modes: Numerical Results

Now we are prepared for comparing the analytical results from above to numerical studies. Before we do so let us first recapitulate our previous result. In Sec. 5.1 we found that for the Gaussian unitary, orthogonal, and symplectic ensemble the dispersion relation of the normal modes is given by $\omega_k^G = \frac{1}{Nk}$. We can also express $\omega_k^G$ in terms of the unfolded coordinates $\xi_p$ defined by Eq. (5.55) and obtain ${\omega'}_k^G = \frac{N}{2\sqrt{2}\pi k}$, see Ref. [68]. Note that the dispersion relation in these coordinates is the same for different definitions of the probability distribution with respect to $\sigma$, see Sec. 5.1.

In Sec. 5.2 we derived the dispersion relation for the Poisson ensemble and found for the soft edge of the spectrum, ${\omega'}_k^P \approx \frac{N^2}{\pi^2 k^2}$. Note that the spectrum of the Poisson ensemble is already unfolded since it has mean level spacing equal to one. We can multiply this result by $1/\rho^2(0)$ (where $\rho$ is the spectral density of the Gaussian ensembles) to obtain the energy scale of the original Gaussian ensemble. (We denote the not unfolded ensemble by the "original" ensemble.) We find $\omega_k^P = 1/(2k^2)$.

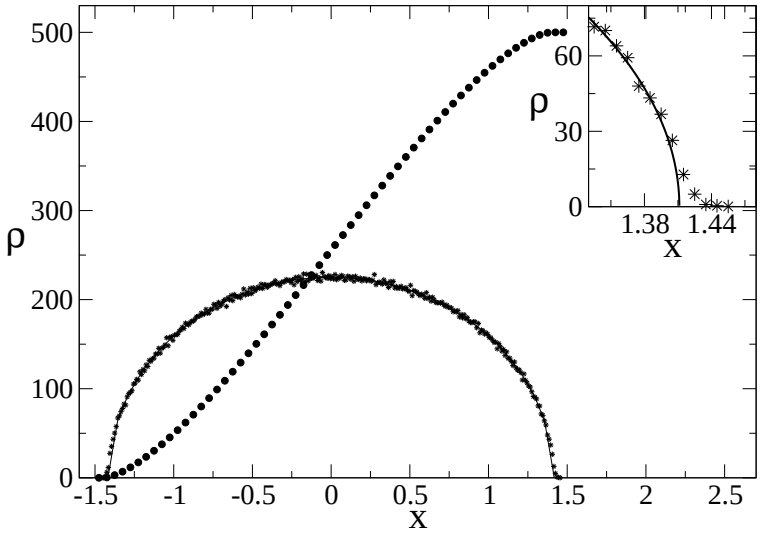


**Figure 5.2:** Numerical data for the GUE for $N = 500$. The semicircle represents the global spectral density $\rho(x)$ and the filled circles show the numerically obtained stair-case function. We see about 300 data points of $\rho$ and 60 data points of the stair-case function. The entire ensemble contains about 1000 configurations. The fitting function $\widetilde{R}_1(x)$ is mostly covered by the data points. We magnified the right end of the spectrum to point out the finite size effects.

Finally, we obtained a result for the eigenvalues of the normal modes for the chiral random matrix model. We also found a $1/k$ behavior, $\omega_k^\chi = 1/(4Nk)$. On the unfolded scale this expression turns into $\omega'_k = \frac{N}{4\sqrt{2}\pi k}$. We list these results in Table 5.1.

In the following we will present numerical data for the dispersion relation of the normal modes. We will show data for the Gaussian unitary ensemble, the chiral QCD ensemble, and finally we will compare our results to "real" lattice data from quenched QCD calculations. Let us begin with the Gaussian unitary ensemble. We already described in the beginning of Sec. 5.1 how to generate configurations numerically. So we start with a set of configurations for a given $N$, that means we have $N_E$ configurations and each configuration contains $N$ eigenvalues of a unitary random matrix which was generated according to the appropriate probability distribution.

| | original scale | unfolded scale |
|---|---|---|
| Gaussian ensembles | $\omega^G = \frac{1}{Nk}$ | $\omega'^G_k = \frac{N}{2\sqrt{2}\pi k}$ |
| Poisson ensemble | $\omega^P_k = \frac{1}{2k^2}$ | $\omega'^P_k \approx \frac{N^2}{\pi^2 k^2}$ |
| chQCD ensemble | $\omega^\chi_k = \frac{1}{4Nk}$ | $\omega'^\chi_k = \frac{N}{4\sqrt{2}\pi k}$ |

**Table 5.1:** Analytical results for the dispersion relation of the normal modes

Note that the number of configurations, $N_E$, always should be larger than the number of the eigenvalues, $N$, because otherwise the eigenvalues of the normal modes contain zero modes. Before we will come to the calculation of the normal modes let us see how to unfold the spectrum. As we saw in Sec. 5.5 we have to express the spectrum in coordinates $\xi_p$. To do so we have to perform an integration over the global spectral density,

$$\xi_p = N(x_p), \quad \text{with } N(x) = \int_{-\infty}^{x} R_1(x')\,\mathrm{d}x'. \tag{5.59}$$

The function $N(x)$ is often referred to as the stair-case function.

In Fig. 5.1 we gave an example for a numerical calculation of $\rho(x)$ for $N = 500$. Since we know the exact result for $\rho(x)$ for large $N$, the Wigner semicircle, we can fit that exact result to our numerical data. Afterwards we can determine the stair-case function $N(x)$ analytically simply by integrating over the semicircle and, finally, end up with the unfolded spectrum. So we made the following ansatz for the fitting function,

$$\widetilde{R}_1(x) = A\sqrt{(R^2 - x^2)}, \tag{5.60}$$

where we fixed the center of the semicircle to zero. We fit this function to our numerical data of Fig. 5.1. The result is shown in Fig. 5.2. We see that the fitting function reproduces the numerical data very accurately. Only at the edges of the spectrum we find discrepancies from the large $N$ result. This finding is responsible for finite size effects which we will address in a moment. For further illustration we also plotted the numerically obtained stair-case function. Another problem which arises is that there are eigenvalues which are larger than the radius of the semicircle we fitted to the data points. Therefore, we cannot unfold these eigenvalues. We solved this problem by fixing these eigenvalues to the edges of the spectrum, so we set eigenvalues at the right most edge of the spectrum to $R$ and eigenvalues at the left most edge to $-R$. This introduces errors of order $1/N$ which is unproblematic.

It is easy to calculate the stair-case function $N(x)$ from our fitting function defined in Eq. (5.60). By integrating we find

$$\widetilde{N}(x) = \frac{A}{2}\left(x\sqrt{R^2 - x^2} + R^2\left(\tan^{-1}\frac{x\sqrt{R^2 - x^2}}{R^2 - x^2} + \frac{\pi}{2}\right)\right). \tag{5.61}$$

where the tilde should emphasize that the coefficients of the function are determined by fitting. We now can unfold the spectrum and can calculate the spectral density in the unfolded coordinates. We know that the result should be constant and equal to one. This is depicted in Fig. 5.3 where we nicely see the coincidence. Because the semicircle is normalized to $N$ the unfolded spectrum starts at $\xi = 0$ and ends at $\xi = N = 500$. Note that there are deviations at the edges of the spectrum. This observation is connected to the observed deviations of the finite $N$ data of the spectral density which we found above. It is a finite size effect and we will explain how this comes about in the following.

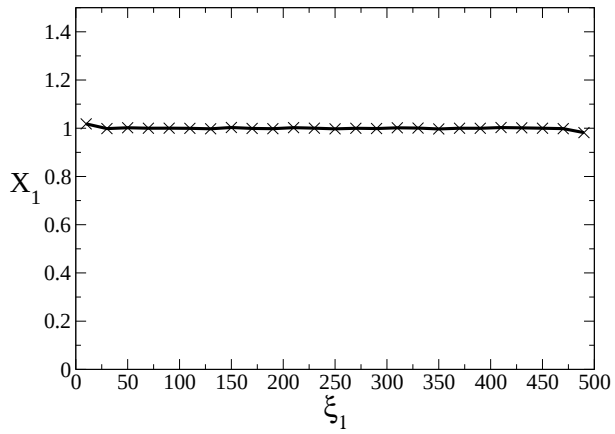


**Figure 5.3:** The unfolded spectral density $X_1(\xi_1)$ for $\rho(x)$ of Fig. 5.2. The spectrum now reaches from 0 to $N = 500$. Note the deviations at the ends of the spectrum.

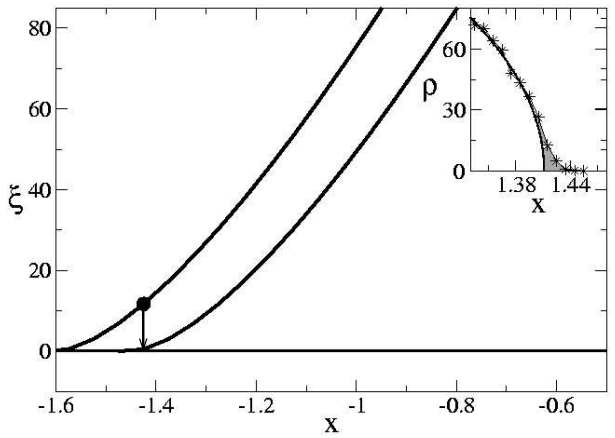


**Figure 5.4:** The curve on the right hand side shows the stair-case function resulting from integrating the fitted Wigner semicircle. The left curve corresponds to the "real" stair-case function which one gets from the finite $N$ data. The magnification shows the right edge of the semicircle of Fig. 5.2. The shift of the two curves should be of the order of the shaded area.

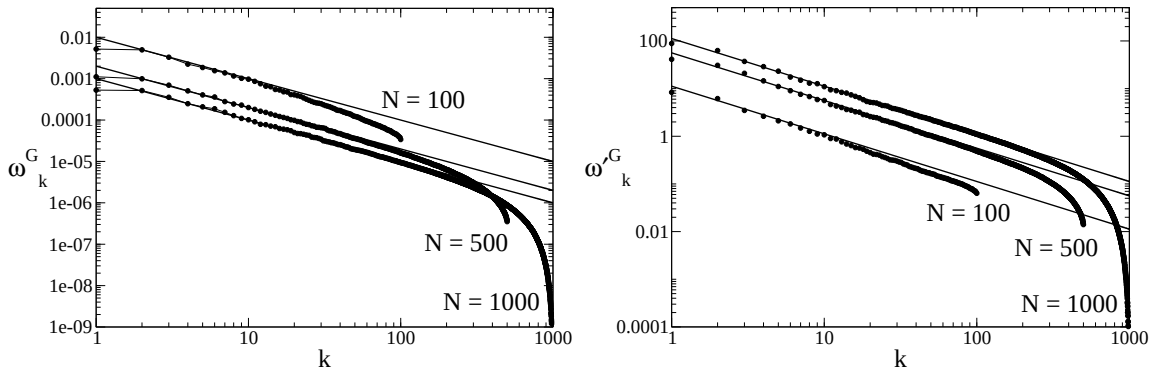


**Figure 5.5:** The dispersion relation of the normal modes for the GUE for $N = 100, 500, 1000$. On the left hand side we see data on the original scale while on the right hand side the eigenvalues are unfolded. The lines show the analytical prediction. Note that in the plot on the left hand side the lowest curve corresponds to the highest matrix dimension while on the right hand side it is the other way round. Each ensemble contains $N_E = 1000$ configurations.

The reason for the bad behavior of the unfolded spectral density at the edges of the spectrum is that we used in a sense the "wrong" stair-case function. As we can see in the magnification of the right edge of the spectrum in Fig. 5.2 the numerical data points lie above the predicted curve for large $N$. Thus, if we would use the readily calculated exact stair-case function for finite $N$, the resulting curve for the "real" stair-case function lies a little above our curve for large $N$. So, approximately, we would obtain the stair-case function for large $N$ shifted to the left by some constant. This constant is approximately the area which is given by the deviation of the finite $N$ result which is easily seen by looking at Eq. (5.59). We illustrate this in Fig. 5.4.

We see that the spectrum on the unfolded scale is shifted to smaller values. Let us focus on the highlighted data point in Fig. 5.4 which lies on the curve for finite $N$. But this data point will be unfolded by the "wrong", infinite $N$ stair-case function and, therefore, be shifted to smaller values on the unfolded scale. So all data points are shifted towards smaller values. Since the spectrum on the unfolded scale starts at zero by definition the shifted eigenvalues accumulate near zero. The result is that the density of the eigenvalues on the unfolded scale, $X_1(\xi_1)$, is enhanced near zero. The opposite happens at the end of the spectrum. Here the eigenvalues are shifted away from the edge and the eigenvalue density is lowered. Note that this is a finite size effect which vanishes as $N$ goes to infinity. We will encounter the problem of having a "wrong" stair-case function later again.

Let us now return to the subject of normal modes. We will calculate them for the GUE both on the unfolded and original scale. We are following the method used in Sec. 5.2 and calculate the normal modes by diagonalizing the matrix $D_{ij}$ defined in Eq. (5.22). In Fig. 5.5 we plotted the eigenvalues $\omega_k^G$ versus the number of the eigenvalue $k$. We generated data for $N = 100, 500, 1000$. Each set contains $N_E = 1000$ configurations. On the left hand side in Fig. 5.5 we plotted the data for the eigenvalues on the original scale while on the right hand side we see the dispersion

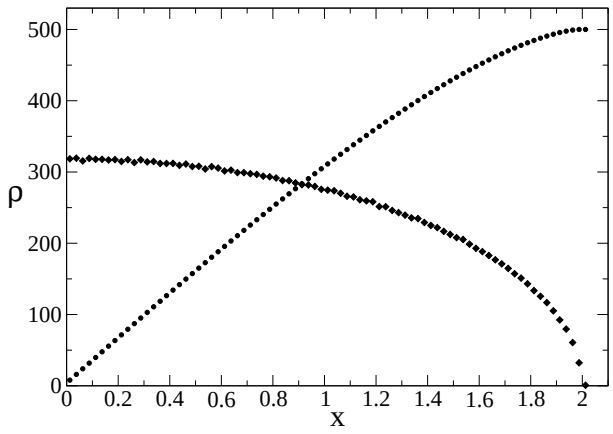


**Figure 5.6:** The curve with the diamonds is the spectral density $\rho(x)$ for the chGUE for $N = 500$. The other curve is the corresponding stair-case function.

relation of the normal modes on the unfolded scale. The straight lines represent the analytical predictions for the various matrix dimensions. As it should be no surprise we find very good agreement between the analytical prediction and our numerical data. Similar plots can be found in Ref. [68].

As a second example we will present numerical data for the chGUE. But in this case we will use a different method to determine the stair-case function. We won't make a fit to the spectral density function using the infinite $N$ result but this time we will determine the stair-case function numerically. The big advantage of this method is that it can be applied in any case, i.e., we don't have to know about the infinite $N$ result. We will use this procedure again when we will calculate the normal modes for the lattice QCD data. So this is a good test for the correctness of our evaluation code.

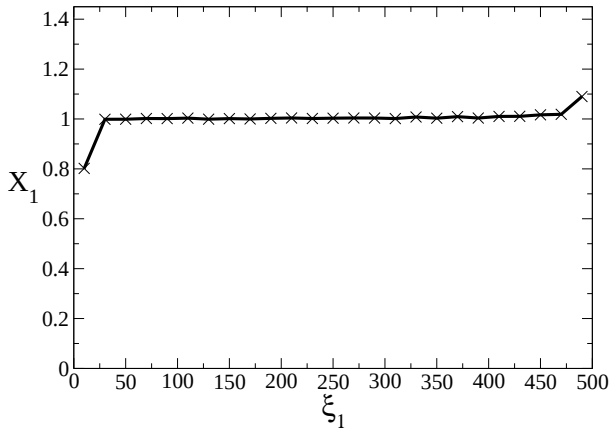


**Figure 5.7:** The unfolded spectral density $X_1(\xi_1)$ which corresponds to Fig. 5.6. We see deviations from the predicted value of one at the edges of the spectrum. The ensemble contains 2500 configurations and the matrix dimension is $N = 500$. The topological sector is zero, $\nu = 0$, and $N_f = 0$.

In Fig. 5.6 we plotted, as in Fig. 5.2, the spectral density and the corresponding stair-case function. We will concentrate on the case $N_f = 0$ and trivial topological sector, $\nu = 0$. Note that the eigenvalues now come in pairs of $\pm x_i$ so we will plot only positive eigenvalues. We determined the stair-case function numerically by simply adding up the spectral density along the $y$-axis. We use the same binning for the stair-case function as for $\rho(x)$. For the unfolding procedure we use the numerically determined stair-case function, like that of Fig. 5.6, and interpolate between the data points. From this "smooth" function we can read off the unfolded eigenvalue for a given value and determine the unfolded spectral density. We plotted $X_1(\xi_1)$ in Fig. 5.7. Note that again we encounter deviations from the large $N$ result at the edges of the spectrum. The reason for this discrepancy is the same as we already mentioned. We used a "wrong" stair-case function at the edges of the spectrum although we used a function which is correct for finite $N$. The reason for the deviation is that at the edges of the spectrum we used a (relatively) to large binning which means that we cannot resolve the fast changing of the "correct" stair-case function. The result is that the interpolation of the data points overestimates the stair-case function at the edges. So the situation is now reversed to the situation for the GUE. The "correct" stair-case function runs *below* the "wrong" one and, therefore, the eigenvalues are shifted away from zero. Obviously, this problem can be solved in principle (as long as you have enough computer power) by increasing the statistics and simultaneously making the bins more narrow.

Now we can calculate the normal modes for the chGUE. We did this again for both the unfolded and original scale. The result is plotted in Fig. 5.8. We calculated ensembles for $N = 100, 500, 1000$. For each ensemble we have 1000 configurations. Remember, we have $\nu = 0$ and $N_f = 0$. On the right (left) hand side we see the dispersion relation on the (original) unfolded scale. The straight lines represent the theoretical predictions. Again, we see very good agreement. Note that on the unfolded scale (right hand side of Fig. 5.8) the lowest curve corresponds to $N = 100$ while on the original scale the curve for the same $N$ is the upper one. An interesting point is the behavior of the different curves at high $k$. Looking at Fig. 5.8 we can see that for largest $N$ there are large deviations from the straight line at the hard edge of the spectrum (large $k$) while for the smallest $N$ we observe only small deviations. This "tail" for large $N$ at large $k$ seems to be cut off for lower $N$. We found that the reason for this tail lies in the statistics. So if we would increase the statistics for $N = 1000$ say a few times larger than $N_E = 1000$ we would see that the tail vanishes.

Now we will come to the goal of this chapter. We will compare chRMT predictions to lattice QCD data. In a sense this can be regarded as comparing a theoretical prediction (chRMT) to an experiment (lattice QCD). This is because there is no (strict) proof that chRMT should describe QCD or at least some regime of it. The only evidence is given by comparing numerical QCD data to chRMT, see e.g. Ref. [76]. We will follow this line and, therefore, provide more evidence for chRMT to be a correct theory describing QCD.

For studying the correlations of the eigenvalues of the Dirac operator we have used several gauge field configurations for different lattice sizes and calculated the

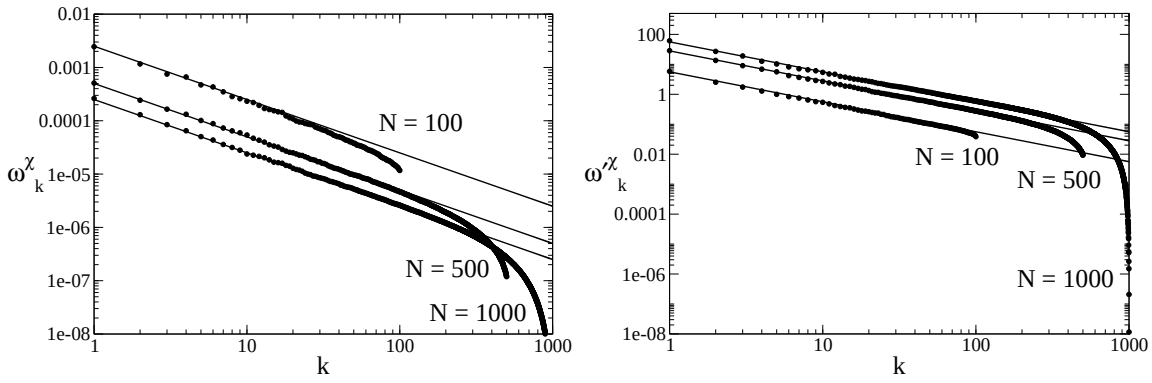


**Figure 5.8:** The dispersion relation of the normal modes for $N = 100, 500, 1000$ for the chGUE. The eigenvalues on the left hand side are on the original scale while on the right hand side the eigenvalues are unfolded. The straight lines correspond to the theoretical prediction. The lowest curve on the left hand side represents the data for the highest $N$ while on the right hand side it is the other way round. Each ensemble contains $N_E = 1000$ configurations.

eigenvalues of the staggered Dirac operator defined in (2.37) for each configuration. A list of lattice sizes, couplings, and statistics can be found in Table 5.2. The matrix

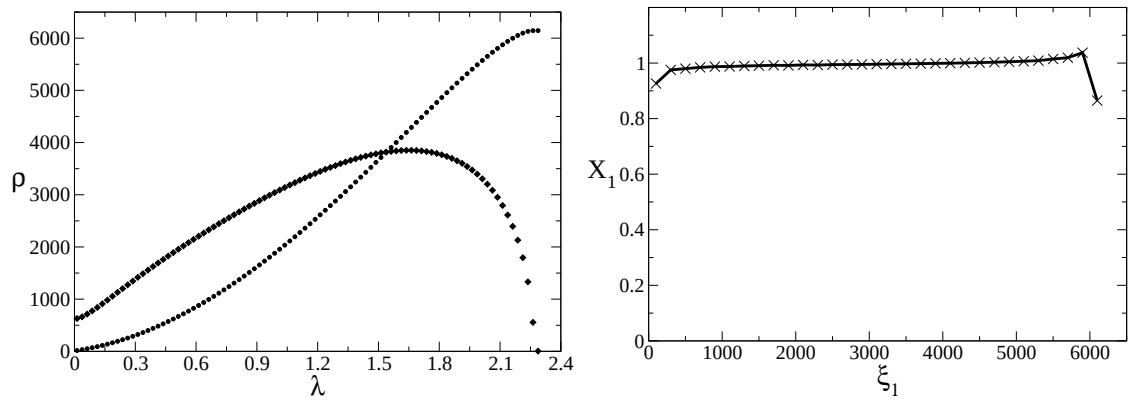


**Figure 5.9:** QCD lattice data. On the left hand side we plotted the original spectral density (diamonds) and the corresponding stair-case function (circles). On the right hand side we see the corresponding unfolded spectral density. We set $\beta = 5.6$ and $V = 8^4$.

dimension of the Dirac operator is $N_c V = 3V$ where $V$ is the four-dimensional lattice volume. Because of the fact that the eigenvalues of the Dirac operator come in pairs $\pm\lambda_i$ we will concentrate on the positive eigenvalues. Note that we have $N = \frac{N_c}{2} V = 3/2\, V$ positive eigenvalues. Let us begin again with spectral density function. In Fig. 5.9 we plotted $\rho(\lambda)$ and the corresponding stair-case function for $V = 8^4$ and $\beta = 5.6$. When we compare the spectral density of the chRMT model to our lattice data we see great differences. Of course, we should not worry about that because the not unfolded spectral density is unphysical. On the right hand side of Fig. 5.9 we see the unfolded spectral density. Again there are deviations at the edges at the spectrum which arise by the same mechanism we explained above. Note that

we used the same unfolding procedure as for the chRMT calculations which means that we unfolded the eigenvalues numerically.

| Lattice volume $V$ | $N = 3V/2$ | $\beta$ | Statistics |
|---|---|---|---|
| $4^4$ | 384 | 5.6 | 7000 |
| $6^4$ | 1944 | 5.6 | 7000 |
| $8^4$ | 6144 | 5.6 | 7000 |

**Table 5.2:** Overview of the used lattice data

Let us now determine the dispersion relation of the normal modes for our lattice data. Recall that the eigenvalues of the normal modes are the eigenvalues of the following matrix

$$D_{ij} = \langle (\lambda_i - \langle \lambda_i \rangle)(\lambda_j - \langle \lambda_j \rangle) \rangle = \langle \lambda_i \lambda_j \rangle - \langle \lambda_i \rangle \langle \lambda_j \rangle , \tag{5.62}$$

where $\langle\, \rangle$ denotes the average over the entire gauge ensemble. Note that we only use positive $\lambda_i$'s in this relation. In Fig. 5.10 we present the eigenvalues of $D_{ij}$ for $\beta = 5.6$ and volumes $V = 4^4/6^4/8^4$. Each ensemble contains 7000 configurations. We denote the eigenvalues of the normal modes of the lattice QCD data on the original scale by $\omega_k$ and on the unfolded scale by $\omega'_k$, respectively. The straight lines are the

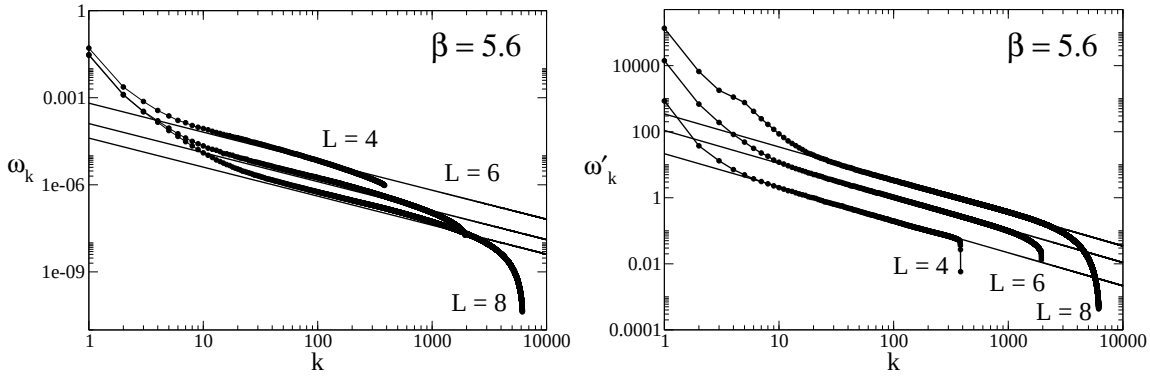


**Figure 5.10:** Lattice QCD data. We show data for $V = 4^4/6^4/8^4$ and $\beta = 5.6$. Each set contains 7000 configurations. On the left hand side we plotted the dispersion relation of the normal modes of the lattice data and corresponding chRMT prediction (straight lines) on the non unfolded scale. The lowest curve corresponds to highest volume $V = 8^4$. The plot on the right hand side shows the corresponding dispersion relation on the unfolded scale. Here the lowest curve corresponds to the lowest volume $V = 4^4$. Note the good agreement at the intermediate region and the discrepancy for small $k$.

corresponding predictions of chRMT. The plot on the left hand side shows the original eigenvalues while on the left hand side the eigenvalues are unfolded. Note that the eigenvalues on the original scale are physically not relevant. Only the eigenvalues on the unfolded scale should be compared to the predictions of chRMT. Anyway, for illustrative purposes we are presenting data on both scales. Let us begin with the

eigenvalues on the scale (left hand side). For small $k$ we see large deviations from the straight line. In the intermediate regime we have good agreement between the data and the predictions although the numerical data lie systematically above the line. We see that already on the original scale the dispersion relation of the normal modes is linear. The hard edge of the spectrum shows the usual deviations which we already saw in the numerical calculations for the chRMT above. On the right hand side of the plot in Fig. 5.10 we can see that in the intermediate regime we have perfect agreement between the lattice data and the curve of the chRMT prediction. At the hard edge of the spectrum we see the typical deviations. The interesting region is the region of small $k$. Here we see deviations from the chRMT which we never saw in our numerical chRMT data (compare to Fig. 5.8). Before we try to explain this observation let us quantify the discrepancy.

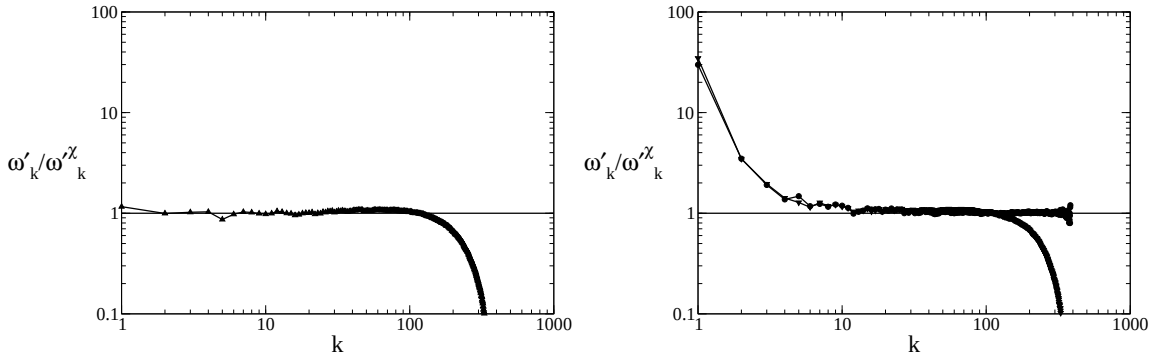


**Figure 5.11:** The plot on the left hand side shows the ratio of the numerically obtained $\omega'^{\chi}_k$ to the analytically obtained $\omega'^{\chi}_k$. We observe good agreement beside the finite size effects at large values of $k$. The two curves in the plot on the right hand side which deviate strongly from one for low values of $k$ represent the ratios of $\omega'_k$ (lattice QCD data) to the numerically (filled circles) and analytically (down triangle) obtained eigenvalues $\omega'^{\chi}_k$ of the chRMT prediction. For the numerical data we used a lattice with $V = 4^4$ and $\beta = 5.6$.

To measure the deviation of the lattice QCD data from the prediction of chRMT we divide for each $k$ the eigenvalues $\omega'_k$ of the normal modes of the lattice data by the eigenvalues $\omega'^{\chi}_k$ of the chRMT result. If, for a certain eigenvalue, this ratio is equal to one it means that the lattice data coincide with the chRMT prediction (for this particular eigenvalue). We restrict ourselves to the physical case of unfolded eigenvalues. Let us first analyze this approach. In Fig. 5.11 we present an example for $V = 4^4$ and $\beta = 5.6$. We begin with a quality check of our numerical data of the chGUE. We generated data for the chGUE similar to the data which we showed in the plot on the right hand side in Fig. 5.8, but now we use $N = 384$. On the left hand side of Fig. 5.11 we plotted the ratio of these eigenvalues of the normal modes of the chGUE to the eigenvalues of the normal modes of the theoretical expression in Table 5.1 for $N = 384$, $\omega'^{\chi}_k = \frac{384}{4\sqrt{2\pi k}}$. We see that the ratio is very close to one which confirms our observation of the good agreement of the numerical and analytical results for the chGUE. Only at large values of $k$ we see deviations but this is a finite size effect. In the plot on the right hand side we show the ratio of the eigenvalues $\omega'_k$

of the normal modes of the lattice QCD data to the eigenvalues $\omega'^{\chi}_k$ of the theoretical expression in Table 5.1, and the ratio of $\omega'_k$ to the numerical result for the chGUE. We observe good agreement between the lattice QCD data and the chRMT predictions in the intermediate regime, the ratios are close to one. At the hard edge we find again finite size effects but for small $k$ we observe strong deviations. There is a critical value of $k$ below which lattice QCD and chRMT do not agree.

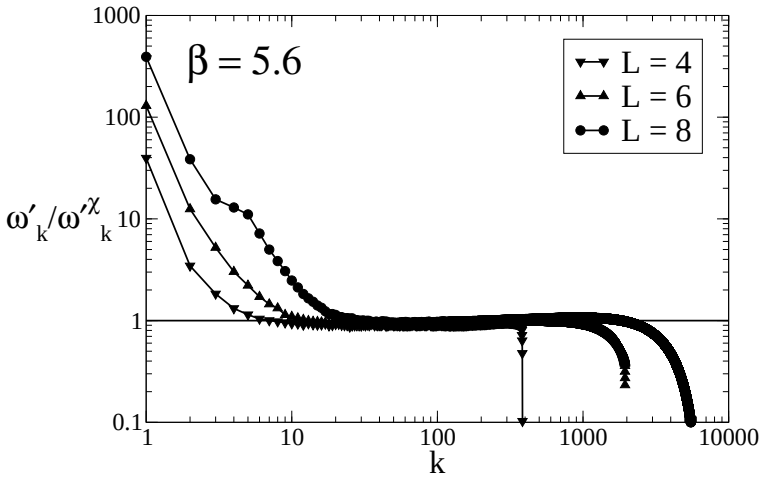


**Figure 5.12:** The three curves represent the ratios of the eigenvalues $\omega'_k$ of the normal modes of the lattice QCD data to $\omega'^{\chi}_k$, the analytical prediction for the chGUE. For the lattice QCD data we used $V = 4^4/6^4/8^4$ and $\beta = 5.6$. The leftmost curve corresponds to the lowest volume. We find that the critical value of $k$, below which lattice QCD and chRMT do not coincide, depends on the volume. Note that all eigenvalues in this figure are unfolded.

On the plot in Fig. 5.12 we plotted the ratio $\omega'_k$ of the lattice QCD data to $\omega'^{\chi}_k$ of the analytical chRMT prediction for three different lattice sizes at $\beta = 5.6$. Notice the good agreement in the intermediate range of $k$, the ratios are very close to one. The hard part of the spectrum shows the common deviations. At the interesting soft part we see that as the volume increases the critical $k$ (the value of $k$ where $\omega'_k$ starts to deviate) moves to higher $k$. In the magnification of this plot in Fig 5.13 we marked the critical values $k_c$. We can read off the critical values and find approximately $k_c = 6/13/24$ for the volumes $4^4$, $6^4$, and $8^4$, respectively. These values correspond to the $k$'s where the ratio $\omega'_k/\omega'^{\chi}_k$ approximately hits the straight line drawn in Fig. 5.12.

The observation that there are deviations of lattice QCD data from the chRMT prediction is, of course, of great interest. Anyway, this is not a big surprise because we should not expect that chRMT describe full QCD in all details. Chiral random matrix theory rather should be valid in a certain regime of QCD. Let us discuss this topic in more detail.

RMT is supposed to describe the physics of a system below a certain energy scale. In condensed matter physics this energy scale is known as Thouless energy, see [69].

In a disordered system it is given by

$$E_c = \frac{\hbar\Delta}{L^2}, \tag{5.63}$$

where $\Delta$ denotes the diffusion constant and $L$ is the linear extent of the system. Below $E_c$ the system is in the ergodic regime and RMT is applicable, above the Thouless energy the system is in the diffusive regime up to another scale beyond which we speak of the ballistic regime. Let us try to find an expression for the Thouless energy in the case of chRMT.

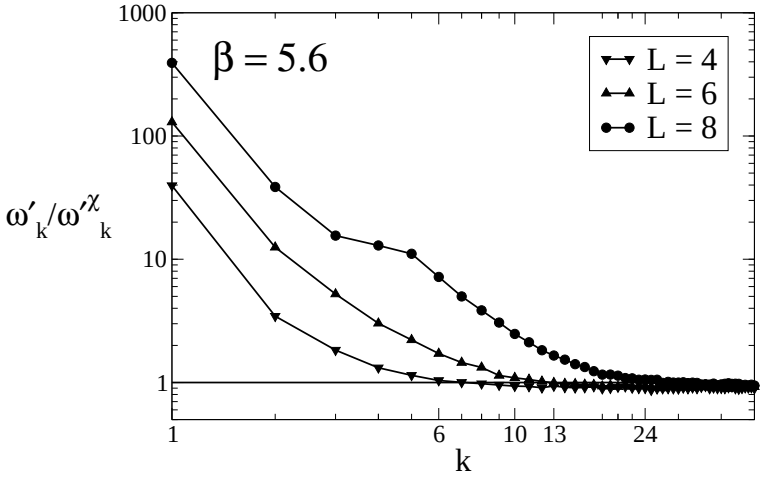


**Figure 5.13:** Magnification of the plot on the left hand side of Fig. 5.12. The values of $k$ where the lattice QCD data and the chRMT prediction do not coincide any more are $k_c = 6/13/24$ for the corresponding volumes $V = 4^4/6^4/8^4$.

Before we will derive an explicit expression for $E_c$ let us attend to the question of the validity of chRMT. All investigations done so far indicate that chRMT should be valid in the following regime

$$\frac{1}{\Lambda} \ll L \ll \frac{1}{m_\pi}, \tag{5.64}$$

where $\Lambda$ is a typical hadronic scale such as the rho mass (about 1 GeV). $L$ denotes the lattice extent. So the lattice volume is $V = L^4$ where we set the lattice spacing $a = 1$ as usual. $m_\pi \approx 140$ MeV is the pion mass. Let us comment on the meaning of the inequalities in the following. The first inequality is connected to the chiral structure of the QCD. It tells us that the Goldstone modes dominate the QCD partition function and, therefore, we can use an effective chiral Lagrangian to describe QCD in this regime [69]. Using this Lagrangian the second inequality ensures that the zero-momentum modes dominate the partition function. This can be seen as follow. The Compton wavelength of the pion is given by $1/m_\pi$. So if this length is much larger than the length $L$ of the box the pion field does not vary much. Then, the derivatives of the field are small which means that the kinetic terms in the chiral Lagrangian can be neglected. This is a crucial point since it is absolutely necessary for RMT

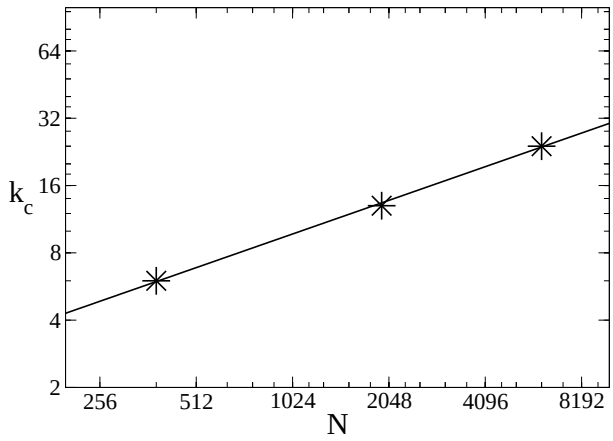


**Figure 5.14:** We plotted $k_c$ vs. $N$. The values are taken from Fig. 5.13. The corresponding volumes are $4^4/6^4/8^4$ and $\beta = 5.6$. The straight line correspond to a fit of the data points to $\widetilde{k}_c(N)$ with a determined value of $A \approx 0.3$.

to apply since RMT cannot reproduce the details of the dynamics of the system it should describe. To conclude, if our system fulfills the inequalities given in Eq. (5.64) we expect chRMT to apply.

To give an explicit expression for the Thouless energy we make use of the Gell–Mann Oakes Renner relation [77] given by

$$m\Sigma = f_\pi^2 m_\pi^2, \tag{5.65}$$

where $f_\pi$ is the pion decay constant in the normalization such that $f_\pi = 93$ MeV in the real world. We can now make use of the second inequality in Eq. (5.64) and find

$$m < \frac{f_\pi^2}{\Sigma L^2}. \tag{5.66}$$

If we then identify the Thouless energy with the critical valence quark mass above which RMT is not valid we find the explicit expression

$$E_c \sim \frac{f_\pi^2}{\Sigma L^2}. \tag{5.67}$$

To obtain a dimensionless expression for the Thouless energy we divide by $D$ and get

$$\frac{E_c}{D} \sim \frac{1}{\pi} f_\pi^2 L^2 \tag{5.68}$$

where $D = \frac{1}{\rho(0)} = \frac{\pi}{V\Sigma}$. Finally, we notice that the matrix dimension $N$ in our chiral random matrix model is proportional to $V = L^4$. This means for the dimensionless Thouless energy

$$\frac{E_c}{D} \sim \sqrt{N}. \tag{5.69}$$

Let us return to the starting point of this little intermezzo, the observed deviations of the lattice QCD data from the predictions of chRMT. It is clear now how we have to interpret the observed discrepancies. The critical values $k_c$ below which the deviation occurs should correspond to the Thouless energy $E_c$. (Note that the eigenvalues of the matrices $D_{ij}$ and $C_{ij}$ of Eqs. (5.22), (5.6) are reciprocal.) So we expect that $k_c$ shows the correct scaling in $N$.

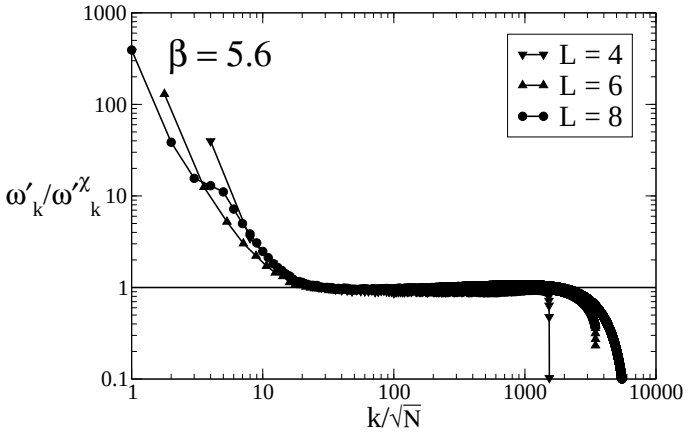


**Figure 5.15:** We plotted the same data as in Fig. 5.12 but rescaled the x-axis by $1/\sqrt{N}$. We see that the curves coincide which means that $k_c$ scales like $\sqrt{N}$.

In Fig. 5.14 we plotted the critical values of $k$ versus the matrix dimension $N$ on a logarithmic scale. We clearly see that the data points lie on a straight line which means that the data follow some power law. We make the following ansatz for a one parameter fitting function

$$\widetilde{k}_c(N) = A\sqrt{N}. \tag{5.70}$$

In Fig. 5.14 the straight line corresponds to the fitting function with a determined value of $A \approx 0.3$. We see that the critical $k$'s behave like $\sim \sqrt{N}$ very precisely which confirms our conjecture that the critical values of $k$ set the scale for the Thouless energy. Further evidence is provided by Fig. 5.15 where plotted Fig. 5.12 again, but this time we rescaled the x-axis by $1/\sqrt{N}$. This means that if the critical value $k_c$ scales like $\sqrt{N}$ the ratios ${\omega'}_k/{\omega'}_k^{\chi}$ should coincide (at least) near the $k_c$. This is exactly what we can see in Fig. 5.15.

The observation that $k_c$ is connected to the Thouless energy is very interesting because in principle it should be possible to extract an absolute value for the Thouless energy. In Refs. [76, 78] the authors determined the Thouless energy quantitatively by looking at the scaling properties of certain quantities. A similar approach should be possible in our case.

We have seen that the analysis of the normal modes in lattice QCD should provide us with a new method to extract the Thouless energy of our system. Of course, it is of great interest to compare the values of the Thouless energy obtained from a normal mode analysis to the Thouless energies the authors of Refs. [76, 78] found, and see whether the results of the different approaches coincide. This will be the task of future work.

# Chapter 6

# Conclusions

In this thesis we were interested in the connection between confinement and chiral symmetry breaking, we searched for calorons on the lattice, and finally we investigated normal modes in the framework of chRMT. In all these studies we made use of the lattice QCD approach. With the help of lattice QCD we could explore the non-perturbative regime of QCD. In partice we worked with staggered and chirally improved fermions with Wilson gauge action or with Lüscher-Weisz gauge action. We discussed the problem of chiral symmetry on the lattice and we have seen that both fermions, which we have used for our calculations, have better chiral properties than ordinary Wilson fermions. This allowed us to study chiral symmetry on the lattice.

In Chapter 3 we reinvestigated the problem, whether the critical point of the chiral phase transition depends on the different sectors of the Polyakov loop. It was claimed by Christ and Chandrasekharan that this is indeed the case which would have had important consequences on the relation between the chiral and confinement phase transition. However, they analyzed the problem with staggered fermions and the order parameter they used was the chiral condensate. In our studies we have used both, chirally improved fermions, which have much better chiral properties than staggered fermions, and staggered fermions. The order parameter we used was not the chiral condensate but the spectral gap. Within our approach we found in contrast to the results of Christ and Chandrasekharan that the critical temperature for the chiral phase transition coincides for the real and complex sector of the Polykov loop. It turned out that this is true for chirally improved as well as for staggered fermions. We also found no dependence of our results on the temporal extent of the lattice. For staggered fermions we analyzed two lattices with $L_t = 6$ ($L_s = 20$) and $L_t = 4$ ($L_s = 16$).

Because we wanted to understand how these different results can come about, we investigated the influence of the mixing of the zero modes of the Dirac operator, which occurs for staggered fermions. Because we know that the zero modes do not contribute to the chiral condensate we have removed them from the calculations in the case of chirally improved fermions, but this is not possible for staggered fermions. For staggered fermions, which do not have exact zero modes, we tried to identify the "zero modes" by their chirality and removed all modes which have chirality larger than some value from our calculations. We could indeed show, that by removing these would-be

zero modes our results for the critical temperature improves, which means that the critical temperatures for both sectors of the Polykov loop are approaching the critical temperature of the confinement phase transition. We conclude that the reason for the different findings compared to the results of Christ and Chandrasekharan is related to the bad chiral properties of the staggered fermions which lead to larger artifacts for the chiral condensate.

In Chapter 4 we searched for calorons on the lattice in order to prove or disprove the correctness of the instanton picture, which we have for spontaneous chiral symmetry breaking. Because of the problems which arise on the lattice when we investigate the topological content of gauge fields, we analyzed the gauge fields indirectly with the help of the localization properties of the fermions. For these studies we have used staggered fermions with Wilson and Lüscher-Weisz gauge action. We looked at ensembles near the critical temperature of the chiral phase transition and we found indeed modes which all show the correct localization properties. In particular, we found low-lying modes with high chirality. This signals that those modes are of topologiacal origin. We observed that these modes are localized in space and delocalized in time, and that the local chirality follows the density of the eigenmode. Further, those states are more localized if they appear in the real sector of the Polyakov loop than in the complex. Altogether, such modes show all the localization properties of a zero mode of a caloron which strongly suggest the existence of calorons on the lattice. Furthermore, we found highly localized modes with low chirality, where a region of positive chirality is next to a region of negtive chirality, which indicates that those modes correspond to instanton-anti–instanton molecules. This is further evidence for the correctness of the instanton picture of spontaneous chiral symmetry breaking.

Finally, we investigated the normal modes in chRMT and lattice QCD. Normal modes naturally provide a basis for studying the fluctuations of the eigenmodes of the Dirac operator around their most likely positions. We compared the analytical results of chRMT to the nummerical results obtained from calculations with staggered fermions and Wilson gauge action. In a certain regime we found great agreement for the lattice data and the chRMT prediction, which is further evidence for the claim that chRMT describes certain aspects of QCD. However, below a certain energy, the Thouless energy, it is known that RMT is not supposed to be applicable. This is exactly what we found. Below a critical value of $k$ we observe, that the lattice data begins to deviate from the chRMT prediction. This observation should, in principle, enable us to determine the Thouless energy with the help of the normal mode analysis, which we will investigate in the future.

# Bibliography


[1] H. J. Rothe, *Lattice Gauge Theories*, 2nd Edition, World Scientific Publishing, 1997.

[2] I. Montvay, G. Münster, *Quantum Fields on a Lattice*, Cambridge University Press, 1994.

[3] C. Gattringer and I. Hip, Nucl. Phys. B 541 (1999) 305, Nucl. Phys. B 536 (1998) 363.

[4] H. B. Nielson, M. Ninomiya, Nucl. Phys. 185, 20 (1981).

[5] D. C. Sorensen, SIAM J. Matrix Anal. Appl. 13 (1992) 357.

[6] http://www.caam.rice.edu/software/ARPACK/.

[7] R. B. Lehoucq, D. C. Sorensen and C. Yang, ARPACK User's Guide, SIAM, New York, 1998.

[8] P. H. Ginsparg and K. G. Wilson, Phys. Rev. D 25 (1982) 2649.

[9] R. Narayanan and H. Neuberger, Phys. Lett. B 302 (1993) 62, Nucl. Phys. B 443 (1995) 305.

[10] C. Gattringer, Phys. Rev. D 63 (2001) 114501.

[11] C. Gattringer, I. Hip and C. B. Lang, Nucl. Phys. B **597** (2001) 451 [arXiv:hep-lat/0007042].

[12] C. Gattringer, M. Göckeler, P. E. L. Rakow, S. Schaefer and A. Schäfer, Nucl. Phys. B **618** (2001) 205 [arXiv:hep-lat/0105023].

[13] M. Lüscher and P. Weisz, Commun. Math. Phys. 97 (1985) 59, Erratum: 98 (1985) 433.

[14] G. Curci, P. Menotti and G. Paffuti, Phys. Lett. B 130 (1983) 205, Erratum: B 135 (1984) 516.

[15] M. Alford, W. Dimm, G. P. Lepage, G. Hockney and P. B. Mackenzie, Phys. Lett. B 361 (1995) 87.

[16] G. P. Lepage and P. B. Mackenzie, Phys. Rev. D 48 (1993) 2250.

[17] J. Snippe, Nucl. Phys. B 498 (1997) 347.

[18] K. F. Liu, *seminar given at Jefferson Lab*, June 2003.

[19] A. M. Polyakov, Phys. Lett. **72B**, 477 (1978); B. Svetitsky and L. G. Yaffe, Nucl. Phys. **B 210 [FS6]**, 423 (1982).

[20] M. A. Stephanov, Phys. Lett. **B375**, 249 (1996).

[21] J. Goldstone, Nuovo Cimento 19, 154 (1961).

[22] T. Banks, A. Casher, Nucl. Phys. B 169, 103 (1980).

[23] H. Leutwyler and A. Smilga, Phys. Rev. D **46**, 5607 (1992).

[24] T. G. Kovács, *Instantons and Chiral Symmetry on the Lattice*, hep-lat/9912021 (1999).

[25] C. Itzykson, J. -B. Zuber, *Quantum Field Theory*, New York 1980

[26] A. A. Belavin, A. M. Polyakov, A. S. Shvarts and Y. S. Tyupkin, Phys. Lett. B **59** (1975) 85.

[27] T. Schäfer, E. V. Shuryak, *Instantons in QCD*, Rev. Mod. Phys. 70, 322 (1998).

[28] G. 't Hooft, Phys. Rev. D **14** (1976) 3432 [Erratum-ibid. D **18** (1978) 2199].

[29] R. D. Carlitz, D. B. Creamer, Ann. Phys. (N. Y.) 118, 429 (1979).

[30] E.-M. Ilgenfritz and E. V. Shuryak, Phys. Lett. **B325**, 263 (1994).

[31] R. Rapp, T. Schäfer, E. V. Shuryak, and M. Velkovsky, Ann. Phys. **280**, 35 (2000).

[32] L. Giusti, G. C. Rossi and M. Testa, Phys. Lett. B **587** (2004) 157 [arXiv:hep-lat/0402027].

[33] C. Gattringer, R. Hoffmann and S. Schaefer, Phys. Lett. B **535** (2002) 358 [arXiv:hep-lat/0203013].

[34] F. Karsch, Lattice QCD at high temperature and density, hep-lat/0106019.

[35] S. Chandrasekharan and N. H. Christ, Nucl. Phys. Proc. Suppl. 47 (1996) 527.

[36] P. N. Meisinger and M. C. Ogilvie, Phys. Lett. B 379 (1996) 163.

[37] S. Chandrasekharan and S. Huang, Phys. Rev. D 53 (1996) 5100.

[38] M. A. Stephanov, Phys. Lett. B 375 (1996) 249.

[39] G. Boyd, J. Engels, F. Karsch, E. Laermann, C. Legeland, M. Lütgemeier and B. Petersson, Nucl. Phys. B469 (1996) 419.

[40] C. Gattringer, P. E. L. Rakow, A. Schäfer and W. Söldner, Phys. Rev. D **66** (2002) 054502 [arXiv:hep-lat/0202009].

[41] C. Borgs and R. Kotecký, Phys. Rev. Lett. 68 (1992) 1734.

[42] C. Borgs and W. Jahnke, Phys. Rev. Lett. 68 (1992) 1738.

[43] C. Gattringer, R. Hoffmann and S. Schaefer, Phys. Rev. D **65**, 094503 (2002) [arXiv:hep-lat/0112024].

[44] J. J. M. Verbaarschot and T. Wettig, Ann. Rev. Nucl. Part. Sci. 50 (2000) 343 [arXiv:hep-ph/0003017].

[45] L. Venkataraman, G. Kilcup, *Applications of the Eigenmodes of the Staggered Dirac Operator*, hep-lat/9710086 (1997)

[46] M. Atiyah and I. M. Singer, Ann. Math. 93 (1971) 139.

[47] P. Hasenfratz, Nucl. Phys. Proc. Suppl. **63**, 53 (1998) [arXiv:hep-lat/9709110].

[48] P. Hasenfratz, Nucl. Phys. B **525**, 401 (1998) [arXiv:hep-lat/9802007].

[49] P. Hasenfratz, V. Laliena and F. Niedermayer, Phys. Lett. B **427**, 125 (1998) [arXiv:hep-lat/9801021].

[50] B. Heinzel *et al.*, *Finding Wollitons on the lattice*, Phys. Rev. D, hep-hap/990815 (1999).

[51] W. Söldner, *Lokalisierungseigenschaften der niedrigsten Quarkzustände im Rahmen der Gitter-QCD*, Diploma thesis, Regensburg, 2000.

[52] M. Göckeler, H. Hehl, P. E. L. Rakow, A. Schäfer, W. Söldner and T. Wettig, Nucl. Phys. Proc. Suppl. **94**, 402 (2001) [arXiv:hep-lat/0010049].

[53] D. J. Gross, R. D. Pisarski, and L. G. Yaffe, Rev. Mod. Phys. **53**, 43 (1981).

[54] G. 't Hooft, unpublished; R. Jackiw, C. Nohl, and C. Rebbi, Phys. Rev. D **15**, 1642 (1977).

[55] B. J. Harrington and H. K. Shepard, Phys. Rev. D **17**, 2122 (1978); Phys. Rev. D **18**, 2990 (1978).

[56] B. Grossman, Phys. Lett. **61A**, 86 (1977); H. Osborn, Nucl. Phys. **B 140**, 45 (1978).

[57] N. Bilić, Phys. Lett. **B97**, 107 (1980).

[58] M. Göckeler, P. E. L. Rakow, A. Schäfer, W. Söldner and T. Wettig, Phys. Rev. Lett. **87**, 042001 (2001) [arXiv:hep-lat/0103031].

[59] T. C. Kraan and P. van Baal, Nucl. Phys. **B 533**, 627 (1998); Phys. Lett. **B428**, 268 (1998); K. Y. Lee and C. Lu, Phys. Rev. D **58**, 025011 (1998).

[60] C. Gattringer, M. Göckeler, P. E. L. Rakow, A. Schäfer, W. Söldner and T. Wettig, Nucl. Phys. Proc. Suppl. **106**, 492 (2002) [arXiv:hep-lat/0110182].

[61] M. L. Laursen and G. Schierholz, Z. Phys. **C38**, 501 (1988); E. -M. Ilgenfritz *et al.*, hep-lat/0011051.

[62] S. Hands, Nucl. Phys. **B329**, 205 (1990).

[63] T. Guhr, A. Muller-Groeling and H. A. Weidenmuller, *Prepared for International School of Physics, 'Enrico Fermi': Unfolding the Layers of the Matter of the Nuclei, Varenna, Italy, 22 Jul - 1 Aug 1997*

[64] A. D. Jackson, C. B. Lang, M. Oswald and K. Splittorff, Nucl. Phys. B **616** (2001) 233 [arXiv:hep-th/0108141].

[65] C. N. Yang and T. D. Lee, Phys. Ref. **87** (1952) 404.

[66] M. L. Metha, *Random Matrices*, 2nd Edition, Academic Press (1991).

[67] A. Andersen, A. D. Jackson and H. J. Pedersen, Nucl. Phys. A **650** (1999) 213 [arXiv:nucl-th/9812037].

[68] A. D. Jackson, C. Mejia-Monasterio, T. Rupp, M. Saltzer and T. Wilke, Nucl. Phys. A **687** (2001) 405. [arXiv:cond-mat/0009332].

[69] T. Wettig, *Random-Matrix Theory in Quantum Chromodynamics and on the Lattice*, Habilitationsschrift, Heidelberg, 1998.

[70] M. E. Berbenni-Bitsch, S. Meyer and T. Wettig, Phys. Rev. D **58**, 071502 (1998) [arXiv:hep-lat/9804030].

[71] E. Brezin, S. Hikami and A. Zee, Nucl. Phys. B **464** (1996) 411 [arXiv:cond-mat/9511104].

[72] L. Del Debbio and C. Pica, JHEP **0402** (2004) 003 [arXiv:hep-lat/0309145].

[73] E. Brezin and A. Zee, Nucl. Phys. B **402** (1993) 613.

[74] G. Hackenbroich, H. A. Weidenmüller, Phys. Rev. Lett. 74, 4118 (1995).

[75] S. Nishigaki, Phys. Lett. B 387, 139 (1996).

[76] M. Göckeler, H. Hehl, P. E. L. Rakow, A. Schäfer and T. Wettig, Phys. Rev. D **59** (1999) 094503 [arXiv:hep-lat/9811018].

[77] M. Gell-Mann, R. J. Oakes and B. Renner, Phys. Rev. **175**, 2195 (1968).

[78] M. E. Berbenni-Bitsch *et al.*, Phys. Lett. B **438** (1998) 14 [arXiv:hep-ph/9804439].

# Dank

Ich möchte mich noch sehr bedanken ...

- bei Prof. Dr. A. Schäfer sowohl für die interessante Aufgabenstellung wie auch für die sehr gute Betreuung.
- bei Dr. habil. Chr. Gattringer, Dr. habil. M. Göckeler, Dr. P.E.L. Rakow, Dr. habil. Chr. Weiss und Prof. Dr. T. Wettig für die hervoragende Zusammenarbeit sowie für die Beantwortung vieler Fragen.
- bei allen Mitgliedern der Arbeitsgruppe für die fachliche und moralische Unterstützung, insbesondere bei meinen Zimmergenossen Barbara Jäger, Marco Stratmann, Axel Kirchner und Tim Opermann, sowie bei unserer Sekretärin Monika Maschek.
- bei meinen Eltern, die dieses Studium nicht nur finanziell ermöglicht haben.
- beim Leibniz Rechenzentrum in München für die Nutzung der Hardware, sowie für den hervoragenden Support und die ausgezeichneten Schulungen.
- beim Brookhaven National Lab, New York, für den angenehmen Aufenthalt und die Gastfreundschaft, die mir zu teil wurde.